THE END OF REIONIZATION: SEARCHES FOR FAINT GALAXIES AND QUASARS IN THE DEEP FIELDS OF THE HUBBLE SPACE TELESCOPE

by

Jian Su

A dissertation submitted to The Johns Hopkins University in conformity with the requirements for the degree of Doctor of Philosophy.

Baltimore, Maryland

December, 2011

Abstract

In this thesis work, we have examined high-redshift galaxies and quasars using the available deep imaging fields, e.g., the Hubble Ultra Deep Field (HUDF) and the Great Observatories Origins Deep Survey (GOODS), by observing with the instruments ACS/WFC and WFC3/IR onboard the Hubble Space Telescope (HST). Our goal is to understand the contributions of high-redshift galaxies and quasars to the ionization of hydrogen, their evolution with cosmic time, and their distribution across the observed fields.

We start with a derivation of the rest-frame ultraviolet (UV) luminosity function (LF) at redshift $z \sim 6$ using a new application of the maximum likelihood method and exploring the five deepest HST/ACS fields. We work on the latest improved data products, which makes our results more robust than those of previous studies. We are the first in this field to use un-binned object counts and thereby make optimal use of the information contained in the dataset. We undertake analysis to a magnitude limit where the completeness is larger than 50% to avoid possibly large errors in the faint-end slope that are difficult to quantify. We also take into account the scattering in and out of the dropout sample due to photometric errors by defining for each object a probability that an object belongs to the dropout sample (called the f-factor technique). Our $z \sim 6$ LF is thus more reliable than that from any previous group.

Using the same technique, we find the best-fit Schechter parameters of the LF at $z \sim 5$, 6, 7 and 8. We also study the evolution of the galaxies within the redshift window $4 < z < 9$ in a unified scheme. The picture that emerges in terms of stan-

dard Schechter function parameters is: a constant ϕ_*, a slowly steepening α, and a relatively rapidly dimmed M_* towards higher redshifts.

Our research survey continues to search for high-redshift quasars. We are among the first groups that have studied the high-redshift LF for both galaxies and quasars. We have identified ten $z \sim 6$ candidates in the four deep fields, much less than expected from those wide surveys at the bright end. Together with our discovery that there are more faint galaxies at $z \sim 6$, we reach the conclusion that galaxies, not quasars, are the main sources for continuing the re-ionization of the 900-million-year universe. Based on our results for the quasar LF, we also predict the quasar number density at $z \sim 7$ and $z \sim 10$ as a guide for future searches.

During our study of quasars, we found one at $z \sim 5$ that has also been detected in the 4 Ms Chandra Deep Field South (CDFS). The X-ray observations show a significant detection, displaying a hardness ratio of HR=0.23 ± 0.24, which, for a source at $z \sim 5$, is highly suggestive of Compton-thick absorption. This is the most distant obscured quasar discovered so far.

In this thesis work, we have processed thousands of optical and infrared images from the HST with various PyRAF procedures, e.g., MultiDrizzle, generated source catalogs with SExtractor based on detection image, tested and modified the dropout selection criteria for high-redshift objects, inspected images visually and excluded interlopers or artifacts, developed sophisticated statistical models, and run a series of IDL/C-language programs to find numerical results.

My thesis advisors are Dr. Massimo Stiavelli and Prof. Colin Norman.

Acknowledgements

It is really my pleasure to thank the many people who make this thesis possible.

I am so lucky to have the best advisors I could imagine. First, I express my sincerest gratitude to my advisor, Dr. Massimo Stiavelli, without whom this thesis would never have come into being. Massimo has offered me immense support and guidance throughout the duration of this project, especially at the most difficult times. He has always provided words of encouragement when I hit a barrier, making sure I did not get entangled by the details or become distracted from the big picture. His perseverance and zeal will continue to inspire me in the years to come. I would also like to thank my co-advisor, Prof. Colin Norman, for keeping track of my academic progress and wading through the mountains of paperwork I had him sign every semester. I was proud when he once introduced me as his co-author in a party at his home.

I thank Prof. Ethan Vishniac for advising me on MHD research and Profs. Michael Boardman, Chih-Yung Chien, Julian Krolik, Tobias Marriage, Tyrel McQueen, Catherine Norman, Colin Norman, Massimo Stiavelli, Morris Swartz, and Wei Zheng for serving in my academic committees.

I owe thanks to my collaborators who enthusiastically reveal the beauty of astronomy to me, especially Roberto Gilli, Colin Norman, Pascal Oesch, Massimo Stiavelli, and Michele Trenti.

The Department provides lots of courses, which I have had the chance to take, by those great educators: Chuck Bennett, Collin Broholm, Chih-Yung Chien, Timothy Heckman, Julian Krolik, Gerhardt Meurer, David Neufeld, Colin Norman, Morris Swartz, Oleg Tchernyshyov, Zlatko Tesanovic, Ethan Vishniac, Rosemary Wyse,

Alexander Szalay. I took a cosmology course by Bennett and Szalay with Adam Riess as a sit-in. Thanks to those outside the department who help me with my teaching: Gina Brissenden, John Feldmeier, Edward Prather, Joseph Di Rienzi.

I appreciate Tabitha Brewster, Barbara Dreyfus, Connie Fliegel, Carmelita King, Sathappan Ramesh, Bill Ruff, Brian Schriver, Jeffrey Tunison, Shane Wolfe and everyone else in the department and institute office, who have always make it convenient for us.

I am grateful to my wonderful peers for useful discussions: Lynn Carlson, Tingyong Chen, Xuemei Cheng, Daiana Di Nino, Timothy Dolch, Yanyan Gao, Hongyu Guo, Tao Hong, Kuang-Han Huang, Yawei Hui, Jianjun Jia, Soyoung Kim, Jingsheng Li, Zhuohan Liang, Roxana Lupu, Max Mutchler, Roderik Overzier, Dmytro Shapovalov, Jiming Shi, Xinwen Shu, Mike Specian, Sundar Srinivasen, Christopher Wells, Qiang Xu, Ching-Wa Yip, Yuan Yuan, Lingzhen Zeng, Leyi Zhu, Zheng Zheng, Xiaozhou Zhou and others. My complete friends list can not fit in this page so I have to acknowledge them elsewhere.

Words cannot express enough thanks to my family, i.e., parents, wife, and kids, to whom I dedicate my PhD thesis.

Contents

Abstract **ii**

Acknowledgements **iv**

List of Tables **ix**

List of Figures **x**

1 INTRODUCTION **1**
1.1 Motivation . . . 1
1.1.1 Cosmology . . . 1
1.1.2 Open Questions . . . 3
1.2 Observations . . . 4
1.2.1 Early Galaxies and Quasars . . . 4
1.2.2 Hubble Space Telescope and Deep Surveys . . . 6
1.2.3 Lyman Break Technique . . . 8
1.3 Luminosity Function . . . 8
1.3.1 Methods . . . 9
1.4 Thesis Overview . . . 10

2 GALAXIES AT REDSHIFT SIX **15**
2.1 Introduction . . . 16
2.2 Data . . . 18
2.3 Luminosity Function of LBGs at $z \sim 6$ . . . 18
2.3.1 Selection Criteria . . . 20
2.3.2 f-factor . . . 21
2.3.3 V-Matrix . . . 22
2.3.4 Evolution of ϕ_* . . . 24
2.3.5 Evolution of M_* . . . 24
2.4 Comparison to Other Results . . . 25
2.4.1 Most Probable $z \sim 6$ LF . . . 25

2.4.2 $z \sim 5$ LBGs LF revisited . . . 25
2.4.3 $z = 3 \sim 6$ Luminosity Density . . . 26
2.5 Conclusions . . . 26

3 HIGH-REDSHIFT GALAXIES IN THE DEEP FIELDS 39
3.1 Introduction . . . 40
3.2 Data . . . 42
3.3 Selection . . . 43
3.4 Luminosity Function . . . 45
3.4.1 LF at $z \sim 7$ . . . 45
3.4.2 LF at $z \sim 8$ . . . 46
3.5 A Unified Frame During One Billion Years . . . 46
3.5.1 Luminosity Evolution . . . 47
3.5.2 Slope Evolution . . . 48
3.5.3 Density Evolution . . . 48
3.6 Conclusions . . . 48

4 HIGH-REDSHIFT QUASARS IN THE DEEP FIELDS 56
4.1 Introduction . . . 56
4.2 $z \sim 6$ Candidates . . . 58
4.2.1 Selection . . . 58
4.2.2 Power-Law Fits . . . 59
4.2.3 Compatibility with SDSS . . . 60
4.3 Estimation for other Redshifts . . . 62
4.3.1 Quasars at $z \sim 7$ . . . 62
4.3.2 Quasars at $z \sim 10$ . . . 63
4.4 Spectroscopical Confirmations . . . 64
4.4.1 J033216.55-274103.2 . . . 64
4.4.2 J033219.05-274429.8 . . . 64
4.4.3 J033229.29-275619.5 . . . 64
4.4.4 J033238.80-274953.7 . . . 65
4.4.5 Our spectroscopic follow-ups . . . 65
4.5 Discussion . . . 66

5 A COMPTON-THICK QUASAR AT $z \sim 5$ 74
5.1 Introduction . . . 75
5.2 Source selection and Observations . . . 76
5.3 X-ray data analysis . . . 77
5.4 Discussion and Conclusions . . . 80
5.4.1 SED fitting . . . 80
5.4.2 Black hole and stellar mass growth . . . 82

5.4.3 Expectations for high-z Compton-thick AGN 83

6 SUMMARY & FUTURE PROSPECTS 87
6.1 Discoveries 87
6.2 Future Works 88

A More About Photometric Scatter and Flux Boosting 91

B Physical Concepts 93
B.1 Cosmology 93
B.2 Ionization 94
B.3 Black Hole 94
B.4 Star Formation Rate 95

Bibliography 96

Vita 108

List of Tables

1.1 Rough Numbers of Dropouts in the HUDF 14

2.1 Dropouts in Our Sample 28
2.2 Completeness of the Fields 28
2.3 Binned numbers of i_{775}-dropouts in the HUDF 36
2.4 Studies of the $z \sim 6$ Luminosity Function 37
2.5 Evolution of the Luminosity Density 38

3.1 Twenty three $z \sim 7$ LBGs in the HUDF 53
3.2 Studies of the $z \sim 7$ Luminosity Function 54
3.3 Twelve $z \sim 8$ LBGs in the HUDF 54
3.4 Studies of the $z \sim 8$ Luminosity Function 55

4.1 Most Updated Quasars z$\geq$5.7 69
4.1 Most Updated Quasars z$\geq$5.7 70
4.1 Most Updated Quasars z$\geq$5.7 71
4.2 Most Updated Quasars at z>3 in Our Deep Fields 72
4.3 Four $z \sim 6$ QSO Candidates in the GOODS-South Field 73
4.4 Expected $z \sim 6$ QSO Numbers in Our Deep Fields 73

A.1 The Steepening of α by the flux boosting for $\sigma(m) \propto 10^{0.3(m-m_*)}$ . . 92

List of Figures

1.1 Comparison of magnitudes in the HUDF and the GOODS. 12
1.2 Comparison of stellarity in the HUDF and the GOODS. 13

2.1 Predicted redshift distribution for i_{775}-dropouts as derived assuming synthetic SEDs and a non-evolving LF in the redshift window $5.7 < z < 7$. The total interloper fraction is estimated to be 24% and is primarily contributed by lower redshift galaxies selected as LBGs due to the aliasing between the Lyman break and the 4000Å break. The model is conservative and at the relatively bright end ($z_{850}<$ 27.5) comparison with Malhotra et al. (2005) shows a factor of two fewer interlopers than predicted by the model. 29
2.2 Color-color diagram of the HUDF $i_{775} - z_{850} > 1.3$ candidates. z_{850} image is rescaled to match Y_{105} to get the z_{850}-Y_{105} color. The dash lines give a possible i_{775}-dropout selection criterion, namely $i_{775} - z_{850} > 1.3$ and z_{850}-$Y_{105} < 1 + 0.09(i_{775} - z_{850}\text{-}1.3)$. 30
2.3 Color-magnitude diagram of the HUDF candidate pool. Candidates are indicated as filled circles whose radius is proportional to the f-factor, and asterisks are those objects with f-factor less than 0.2. The diamonds are i_{775}-dropouts selected in one realization for use in later ML process, and the line segments connect the cataloged and realized positions in the diagram. 31
2.4 Likelihood contour for the best fit Schechter parameters of the $z \sim 6$ LF. The contours, inner to outer, stand for 1-parameter 1-σ, 2-parameter 1-σ, and 1-parameter 2-σ likelihood contours averaged over realizations for use in the ML process. 32

2.5 Most probable parameter space at $z \sim 6$ based on ten studies. The inner contour includes 68% probability and the outer 95%, assuming all the studies are independent and correct. Two nearby squares are from Bouwens et al. (2006, 2007), a third square is from McLure et al. (2009) who combine their data with Bouwens et al. (2007), and the diamond is from this work. As illustrated in Fig. 2.4, M_* and α are strongly correlated, so we do not plot their error bars, which can be found in Table 2.4. 33
2.6 Luminosity function from $z \sim 3$ to $z \sim 6$ 34
2.7 Luminosity density from $z \sim 3$ to $z \sim 6$ integrated to 0.3 (diamonds), 0.2 (squares), 0.04 (circles) of $L_*(z = 3)$. $z \sim 3$ data calculated from Reddy & Steidel (2009), $z \sim 5$ data calculated from paper II, and $z \sim 6$ data calculated from this work. See Table 2.5 for the numbers. 35

3.1 Selection function S(m,z). The blue line is from the GOODS, the green one from HUDF NICP12, and the black one from the HUDF. It's clear that the selection function is very close to unity and drops rapidly near the detection limit of the survey. The two horizontal lines show that when shifting the selection function of different fields according to their deepness, the function is universal. 50
3.2 Color-color diagram of z_{850}-dropouts in the HUDF field. Candidates are indicated as filled circles whose radius is proportional to the f-factor, and asterisks are those objects with f-factor less than 0.2. See Equation (3.1)-(3.3) for the selection criteria and Table 3.1 for their photometry. 51
3.3 Color-color diagram of Y_{105}-dropouts in the HUDF field. Candidates are indicated as filled circles whose radius is proportional to the f-factor, and asterisks are those objects with f-factor less than 0.2. See Equation (3.6)-(3.8) for the selection criteria and Table 3.3 for their photometry. 52

4.1 QLF at $z \sim 6$. The slope-fit (green line) is from Jiang et al. (2008) and the slope-flat (blue line) is 1σ flatter. The red line is fitted for all SDSS points and our candidates, assuming they are all real which are actually the upper limit. 68

5.1 *Top* : The observed 4 Ms *Chandra* X-ray spectrum of XID403 and best-fit model (data/model ratio in the bottom panel). A best fit column density of $N_H = 1.4^{+0.9}_{-0.5} \times 10^{24}$ cm^{-2} is obtained when assuming $\Gamma = 1.8$. The spectrum has been rebinned for display purposes. *Bottom* : Response corrected spectrum and best fit model. The inset shows a smoothed 0.9-4 keV image of XID403 (size is 30"×30"). The cross marks the position of the optical V-dropout. 85

5.2 Spectral energy distribution of XID403 (observed frame) and possible decomposition into a galaxy component (red dashed line) and an AGN component (blue dotted line). The green solid line is the sum of the two. The template of Arp 220 shifted to $z = 4.76$ is adopted for the galaxy emission. The sum of a torus and a scattered component is adopted for the AGN emission (see text). 86

For HUALEY

by SU Jian:

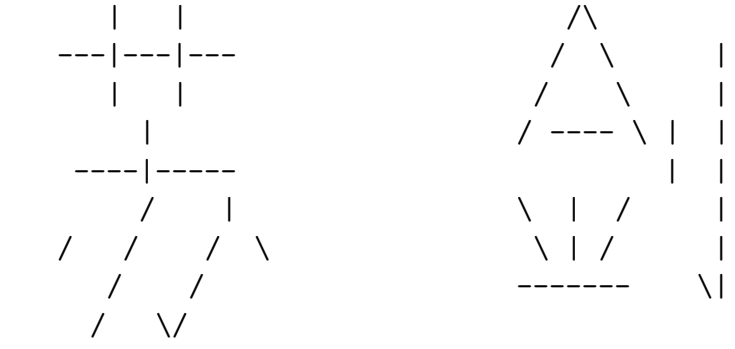

Chapter 1

INTRODUCTION

Our research interests in this thesis focus on the very young universe, especially observations in the deep fields of the Hubble Space Telescope (HST). We study early galaxies and quasars for their properties and roles in cosmology.

1.1 Motivation

1.1.1 Cosmology

We first describe the cosmological framework we adopt. It is referred to as the standard model of the big bang cosmology, i.e., the cold dark matter model with dark energy (Lambda-cold dark matter, ΛCDM). More general introductions can be found in Peebles (1993), Liddle (2003), or Weinberg (2008) and we leave technical details used in this thesis to the Appendix B.

The curvature of space-time is flat[1], in agreement with the assumption that the universe on large scales is homogeneous and isotropic (the cosmological principle) and also the observation that the average density of mass-energy is close to the critical one, i.e., we use the Wilkinson Microwave Anisotropy Probe (WMAP, Komatsu et al. 2011)

[1] 1) a theoretical argument known as the flatness problem shows that anything except flat would evolve too fast and it would require fine tuning for us to be in an almost flat universe, 2) inflation predicts a flat universe, 3) cosmic microwave background radiation shows that it's flat.

parameters. The geometry and evolution of the universe are determined by physical laws, i.e., general relativity, and by the fractional contribution of various types of components: radiation, baryonic matter, dark matter, and dark energy. The standard model of cosmology starts with an extremely hot state named the hot big bang. The cosmos then expands fast and cools down, decoupling different components. The decoupling of matter and radiation is accompanied by recombination of hydrogen. Following the so-called dark ages, characterized by the absence of discrete sources of radiation, is the cosmic dawn when collapse of gravitational density perturbations of baryonic matter around dark matter halos leads to the birth of the first stars. These stars are massive and short-lived, and then explode as supernovae, sometimes leaving behind the first black holes (BHs). More and more infant galaxies form, merge, and quickly grow supermassive BHs in their nuclei and become luminous quasars. The ultraviolet (UV) radiation from these sources ionize the intergalactic hydrogen gas into protons and electrons, initiating the epoch of reionization.

Exploring the first stars, galaxies, and quasars is vitally important for astronomy. As summarized by Stiavelli (2009), firstly, the reionization of hydrogen is a global phase transition affecting the range of viable masses of galaxies; secondly, it makes it possible to probe the density fluctuations emerging from recombination at scales smaller than are accessible by current cosmic microwave background (CMB) experiments; and lastly, we may learn about processes relevant to the formation of the nuclei of present-day giant galaxies and perhaps also find clues to the connection between the growth of BHs and evolution of their host galaxies. The formation and evolution of galaxies and quasars, from the first stars at very high redshifts to the diversified galaxies in the present universe, are among the most important questions in astronomy that are moderately close to a full understanding (Giavalisco 2002).

Reionization is less an event than a process, extended in both time and space. (e.g., Wyithe & Loeb 2004; Stiavelli 2009), from $z \sim 6$ (e.g., Fan et al. 2006b) to possibly higher than $z \sim 20$. The initial pre-overlap stage consists of individual ionizing sources turning on and ionizing their surroundings. The overlap phase begins when neighboring HII regions begin to overlap. At the end of this stage, the low-

density intergalactic medium (IGM) has been highly ionized, and this landmark is most often referred to as the moment of reionization. Then the post-overlap phase continues indefinitely because collapsed objects retain neutral gas even in the current universe. Many models yield a reionization redshift around $7 - 12$ (e.g., Loeb & Barkana 2001; Barkana & Loeb 2001; Ciardi & Ferrara 2005). At the end of overlap, the IGM is heated by the ionizing radiation and the intergalactic Jeans mass increases dramatically, changing the minimum mass of forming galaxies (e.g., Miralda-Escudé & Rees 1998). ΛCDM cosmology predicts the first non-linear dark matter condensations, 2-3 σ peaks of the primordial density field on mass scales of 10^{5-6} $M_\odot$, collapse at redshifts $z = 15 - 20$ (Haiman 2009).

The above theoretical investigations have been well confirmed by observations. The recent measurement of the optical depth to electron scattering by WMAP (Komatsu et al. 2011) suggests that there are sources of radiation that significantly ionize the IGM at redshift $z \sim 10.6 \pm 1.2$ under the assumption that the universe is reionized instantaneously from the neutral state to the fully ionized state. The detection of CMB anisotropies also continues to confirm that the large-scale structure in the universe originates from small-amplitude density fluctuations at early times (e.g., Peebles 1993).

We adopt ΛCDM cosmology: $\Omega_M = 0.3$, $\Omega_\Lambda = 0.7$, and $H_0 = 70$ km s^{-1} Mpc^{-1}. Magnitudes are in the AB system.

1.1.2 Open Questions

Even though the big picture of reionization has been put together, many details remain unknown. Which sources ionize the universe during the epoch of reionization: galaxies or quasars? And exactly when does reionization occur? What is the process of formation and evolution of galaxies and quasars at high redshifts? What are the interactions between these sources and their environment? What is the surface density of galaxies and quasars? These are questions we address in this thesis.

Given that theoretical guidance is very uncertain because it requires a large num-

ber of assumptions and free parameters, direct empirical information is essential in guiding the investigation. As shown in the next Section, deep imaging surveys by the HST provide us a unique opportunity to study the early galaxies and quasars in detail, e.g., their luminosity function (LF), with the help of the Lyman-break technique.

1.2 Observations

1.2.1 Early Galaxies and Quasars

The main objects we focus on in this thesis are high-redshift quasars and galaxies.

Quasars are thought to be extremely powerful and distant active galactic nuclei (AGNs). The observations of quasars began in the late 1950s with radio telescopes and the term *quasar* was coined (Chiu, 1964) soon after 3C 273, the optically-brightest of its kind in the sky, was found to be at a cosmic distance.[2] Emitting radiation from X-ray to far-infrared, some quasars are also strong sources of radio or gamma-ray emission. Their spectra are characterized by a high redshift and by a combination of very broad lines with narrow forbidden lines. The widths of the broad lines resulting from Doppler shifts are due to the high speed of the gas emitting those spectral lines. The narrow-line clouds lie further out, moving more slowly. A high redshift implies large distances associated with the expansion of the universe, and consequently, huge luminosities. The energy for quasars comes from accretion disks around central SMBHs, which, by gravitational force, can convert 10% of the mass into energy as compared to 0.7% for nuclear fusion process that dominates inside stars of solar mass. Quasar's host galaxies become ordinary galaxies when they run out of surrounding gas and dust, after a few (tens of) Myrs of accretion.

Gunn & Peterson (1965) first proposed using Lyα resonance absorption in the spectrum of distant quasars as a direct probe of the neutral hydrogen density in the IGM at high redshifts. At $1.5 < z < 2.5$, the UV ionizing background is dominated by quasars whereas at $z > 3$, the density of luminous quasars decreases faster than

[2]Shields (1999) presents a detailed discovery history of quasars.

that of star-forming galaxies so that their contribution is less prominent. Studies have shown (e.g., Fan et al. 2001, Jiang et al. 2009, and Willott et al. 2010) that quasars could not have maintained IGM ionization at $z \sim 6$, as the quasar number density drops dramatically towards high redshift and the shape of the LF at $z \sim 6$ is not much steeper than that at $z < 3$. On the other hand, the strength of quasar emission lines remains roughly constant through cosmic history (SDSS, Fan et al. 2006a, Abazajian et al. 2009). The $z \sim 6$ quasars have very similar properties to their lower-redshift analogues in the rest-frame UV, visible and X-ray bands (e.g., Fan et al. 2006b), suggesting they are already evolved objects. Therefore, quasars have a strong evolution in the values of their luminosity but do not exhibit significant changes in other properties, and it is not well understood what is the cause of the luminosity evolution. All known $z \sim 6$ quasars are listed in Table 4.1. The host galaxies surrounding quasars have been identified in some cases, and they may be star-forming too (Schramm et al. 2008).

Most galaxies known at $z > 3$ are those that are still forming new stars (star-forming galaxies), especially with Lyα emission, due to the well-known detection bias. Glazebrook et al. (2004) and Cimatti et al. (2004) have found "old", evolved, massive galaxies when the universe was only 3 billion years old. These studies are forcing astronomers to consider whether massive galaxies grew much earlier than predicted by the hierarchical model, or whether the stars in these galaxies formed in a different way from our expectations. Hierarchical galaxy formation is the model whereby massive galaxies form from an assembly of smaller units. This model succeeds in describing the clustering of galaxies, but the evolutionary history of massive galaxies is not accurately predicted.

Large ground-based telescopes such as the Keck 10-meter telescopes, the 8-m Very Large Telescopes (VLTs) of the European Southern Observatory, the 8.3-m Subaru telescope and the 8-m Gemini North and Gemini South telescopes make redshift determinations possible for such early galaxies, which are too faint to be spectroscopically identified by earlier generations of telescopes. They also confirm several z$\geq$7 candidates (e.g., Vanzella et al. 2011 and Lehnert et al. 2010) selected by the

Lyman-break technique (Chapter 1.2.3), as well as about one hundred $z \sim 6$ galaxies (Chapter 2).

1.2.2 Hubble Space Telescope and Deep Surveys

The best instrument so far to detect faint high-redshift sources is the Hubble Space Telescope (HST). HST is a space telescope that was carried into orbit by space shuttle Discovery in 1990. Named after astronomer Edwin Hubble, it is built by the United States space agency NASA, with contributions from the European Space Agency, and is operated by the Space Telescope Science Institute in Baltimore.

The Advanced Camera for Surveys (ACS) camera, installed on March 7, 2002, is designed to provide the HST with a deep, wide-field survey capability from the near-UV to near-infrared (IR) at 1100 nm. One of the three channels of the ACS is the Wide Field Channel (WFC), which has $\sim$202$\times$202 arcsecond field of view from 3700 - 11,000 Å. The detector employs a mosaic of two 2048$\times$4096 Scientific Imaging Technologies (SITe) CCDs, with $\sim$0.049 arcsec/pixel. The initial design and scientific capabilities of the ACS were defined by a team based at Johns Hopkins University (Ford et al. 2003).

One deep survey of the HST/ACS is the Great Observatories Origins Deep Survey (GOODS, Giavalisco et al. 2004), which combines deep observations also from the Spitzer Space Telescope in the IR, and the Chandra Space Observatory in the X-ray. Two fields of 10$\times$16 arcmin field of view center on the Hubble Deep Field North (12h 36m 55s, +62° 14m 15s) and the Chandra Deep Field South (3h 32m 30s, -27° 48m 20s) respectively.

With the desire to see fainter and further galaxies, astronomers observe even deeper fields beyond the GOODS. The Hubble Ultra Deep Field (HUDF, Beckwith et al. 2006), a million-second-long exposure, is the deepest image of the visible universe ever taken. The field consists of a single ultra-deep field observed by four filters of the ACS/WFC: F435W (56 orbits), F606W (56 orbits), F775W (150 orbits), and F850LP (150 orbits). The pointing is (3h 32m 39s, -27° 47m 29.1s) with $\sim$11 arcmin^2 field of

view, a subregion of the GOODS-South field.

There are 1980 objects detected both by the GOODS and the HUDF. At bright magnitudes, $z_{850} < 26$, the two surveys match pretty well (Fig. 1.1), with the GOODS magnitude slightly fainter, possibly because of the choice of zero magnitudes. When the GOODS reaches close to its detection limit, it fails to count all the photons from faint sources so that they look much fainter than their actual brightness as detected by the HUDF. In the meanwhile, other parameters measured by the GOODS also become invalid at the faint end, e.g. the stellarity (Fig. 1.2). In the magnitude $24.5 < z_{850} < 25$, there are only seven out of 126 objects having different stellarity ($\delta_{S/G} < 0.1$) measured by the GOODS and the HUDF, whereas in the magnitude range $26 < z_{850} < 26.5$ there are 74 out of 299 of them. This justifies additional observations going deeper than the GOODS, i.e., the HUDF, and warns us to be careful at the faint limit of the surveys (e.g., Table 2.2).

Between the GOODS and the HUDF, the Hubble Ultra Deep Field Follow-up (UDF05, Oesch et al. 2007) has two principal fields: NICP12 (3h 33m 03.60s, -27° 41m 01.8s) and NICP34 (3h 33m 07.7s, -27° 51m 47.0.1s), which are the two Near Infrared Camera and Multi-Object Spectrometer (NICMOS) parallel fields that are acquired while the HUDF is imaged with ACS (Thompson et al. 2005).

The most relevant HST NIR instrument for high-z studies is the Wide Field Camera 3 (WFC3). It was installed on May 14, 2009, designed to provide HST with a high-sensitivity, high-resolution, wide-field survey capability covering a broad wavelength range, from the near-UV at 200 nm to the near-IR at 1700 nm. One of the two channels of the WFC3 is the Infrared channel (IR), which has $\sim$136×123 arcsecond field of view from 800 - 1700 nm. The detector employs a 1024×1024 Teledyne low-noise, high-QE HgCdTe detector array, with $\sim$0.13 arcsec/pixel. The HUDF09 program (Oesch et al. 2010; Bouwens et al. 2010a) has devoted 192 orbits to observations of the three fields of HUDF and UDF05, using the newly available WFC3/IR filters: F105W, F125W and F160W.

All these deep fields observed by the HST/ACS and the HST/WFC3 constitute an unparalleled treasure for studying faint sources lying at comic distance.

1.2.3 Lyman Break Technique

To best select high-redshift objects observed by the HST, we need to apply the Lyman break technique.

Gunn & Peterson (1965) show that even a tiny neutral hydrogen fraction in the IGM would produce a large optical depth at given wavelength. Absorption by the Lyα forest clouds implies that above $z \sim 2$, only sources in a small redshift range are visible to a typical point in the IGM.

Distant sources can be photometrically discovered by the Lyman-Break technique (e.g., Steidel et al. 1999). Hydrogen gas clouds lying along the line of sight absorb UV radiation, so that the detected flux drops significantly at corresponding wavelengths, e.g., near-IR for the first generation objects. If we observe that an object has a very red color with two adjacent broadbands, i.e., being much brighter on the longer wavelength band, then it is called a dropout and is probably a high-redshift source. More comprehensive selection criteria should also be satisfied, usually asking for additional blue color measurements in the non-ionizing continuum. High-redshift star-forming galaxies can be selected by this technique in a very efficient and effective way (e.g., Malhotra et al. 2005 and Vanzella et al. 2009).

Current estimates of the star formation rate (SFR) at $z \sim 6$ mostly come from photometrically-selected F775W-band dropouts in the deep fields observed by the HST (Chapter 1.2.2). Large samples of dropouts have been collected and are waiting for spectral confirmations. Without spectroscopy, it is still possible to measure the LF and the SFR precisely as we will see in Chapter 2, if the contaminations and completeness are well estimated, together with solid statistics. Table 1.1 lists rough numbers of them in the HUDF, with other $\sim$5000 sources at lower redshifts in the same field.

1.3 Luminosity Function

To answer all these questions posed in Section 1.1.2, we need to count the sources, in magnitude and in redshift.

From as early as the 1930s, astronomers have tried to quantify the statistical nature of the evolution of galaxies by studying their luminosity distribution - known as the luminosity function (LF). One of the key features of this thesis is to derive the most updated LF of distant galaxies and quasars.

The LF provides us with a robust handle to compare the difference between different sets of galaxies and allows us to assess the statistical nature of galaxy formation and evolution. The LF describes the relative number of galaxies of different luminosity (brightness) by counting them in a co-moving volume which measures the number density of galaxies per unit of luminosity L,

$$dN = \phi(L)dLdV \tag{1.1}$$

It is typically written in the Schechter form,

$$\phi(L)dL = \phi_*(\frac{L}{L*})^\alpha \exp(-\frac{L}{L*})\frac{dL}{L*}, \tag{1.2}$$

where ϕ_* is a normalization factor that defines the overall density, L_* is the characteristic luminosity at the knee of the function, and α defines the faint-end slope of the LF and is usually negative, implying more faint galaxies than bright ones.

It is common to convert the equation from absolute luminosity to absolute magnitude $M \sim 2.5 \log L$, with the help of $\phi(L)dL = \phi(M)dM$,

$$\phi(M) = (0.4 \ln 10)\phi_* 10^{0.4(1+\alpha)(M_*-M)} \exp(-10^{0.4(M_*-M)}). \tag{1.3}$$

1.3.1 Methods

Many methods have been developed to estimate the LF, as reviewed in Johnston et al. (2011). We introduce here two non-parametric approaches and their drawbacks, and leave the detailed explanation of our parametric approach in Chapter 2.3.

The "effective volume" (V_{eff}) technique (Steidel et al. 1999) is the generalization of V_{max} estimator (Schmidt 1968).

$$\phi_i = \frac{N_i}{V_{eff,i}}, \tag{1.4}$$

where N_i is the number of galaxies in the given magnitude bin and $V_{eff,i}$ is the effective co-moving volume considering selection bias.

In the stepwise maximum likelihood method (SWML, Efstathiou, Ellis, & Peterson 1988), the LF is parameterized as a series of step functions,

$$\phi(M) = \Sigma\phi_i \; W(M_i - M), \tag{1.5}$$

where $W(x)$ represents two window functions, $W(x) = 1$ when $-\Delta M/2 \leq x \leq \Delta M/2$, and 0 otherwise. The likelihood $\mathcal{L}$ is given by

$$\ln \mathcal{L} = \Sigma W(M_j - M_k) \ln \phi_k - \Sigma\Sigma\phi_j \; H(M_{max,k} - M_j)\Delta M, \tag{1.6}$$

where $H(x)$ represents three window functions, $H(x) = 1$ when $x > \Delta M/2$, 0 when $x < -\Delta M/2$, and $x/\Delta M + 1/2$ otherwise.

These two methods depend essentially on binning the data, which is exactly the reason we do not use them. Binning may lose information, and lead to biased results dependent on bin size. At the same time, having very few luminous candidates in current high-redshift surveys, there is huge uncertainty about the numbers in the bright bins since the candidates could jump into adjacent bins due to photometric errors. Simulations by Trenti & Stiavelli (2008) show that binning is likely to affect the confidence regions for the best-fit parameters. Therefore, we would like to employ one parametric approach in our later calculations, namely, the maximum likelihood estimator (STY79, Sandage, Tammann, & Yahil 1979).

1.4 Thesis Overview

The thesis is organized as follows:

In Chapter 2, we derive the galaxy LF at $z \sim 6$ by studying five deep fields observed by the ACS/WFC. With un-binned data, we modify STY79, introduce the f-factor technique, and find a steeper slope in the LF than previously thought.

In Chapter 3, we derive the galaxy LF at $z \sim 7$ and $z \sim 8$ combining images observed by the ACS and the WFC3, and examine the evolution of the LF from $4 < z < 9$.

In Chapter 4, we derive the quasar LF at $z \sim 6$ from the deep fields. Faint quasars are much less than expected. We also search for quasars at other high redshifts.

In Chapter 5, we present the discovery of an obscured $z \sim 5$ quasar by matching sources in the HST and the Chandra. It is the highest redshift Type 2 quasar discovered, and the only one at $z \sim 5$.

In Chapter 6, we end with a summary of the thesis work and indicate possible directions of future research.

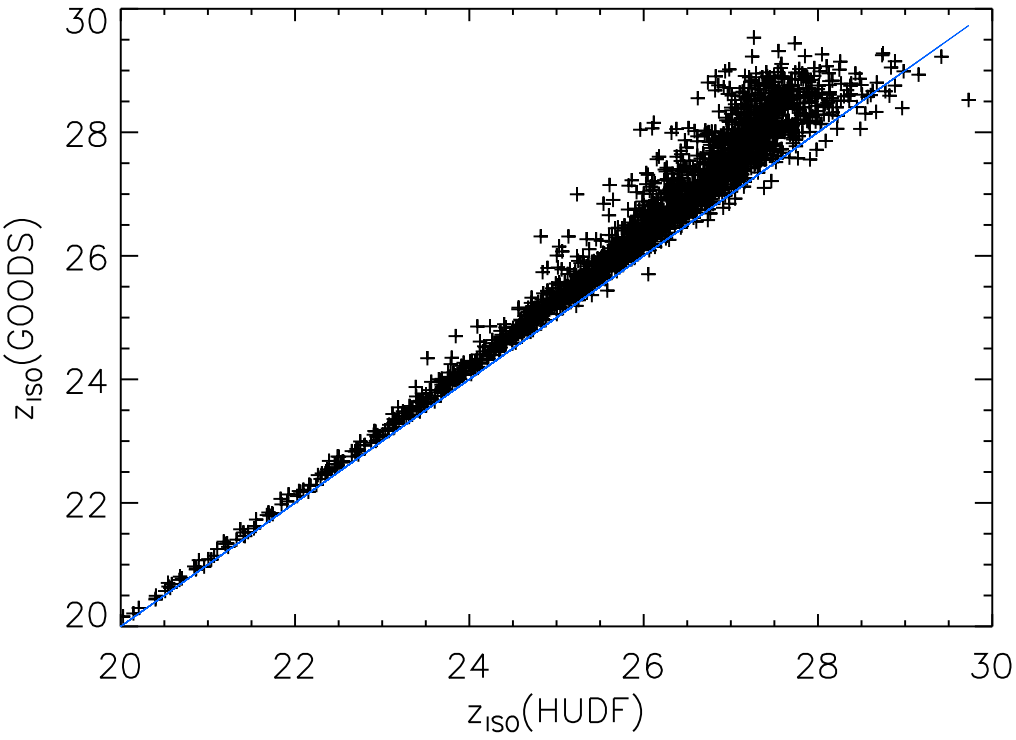

Figure 1.1 Comparison of magnitudes in the HUDF and the GOODS.

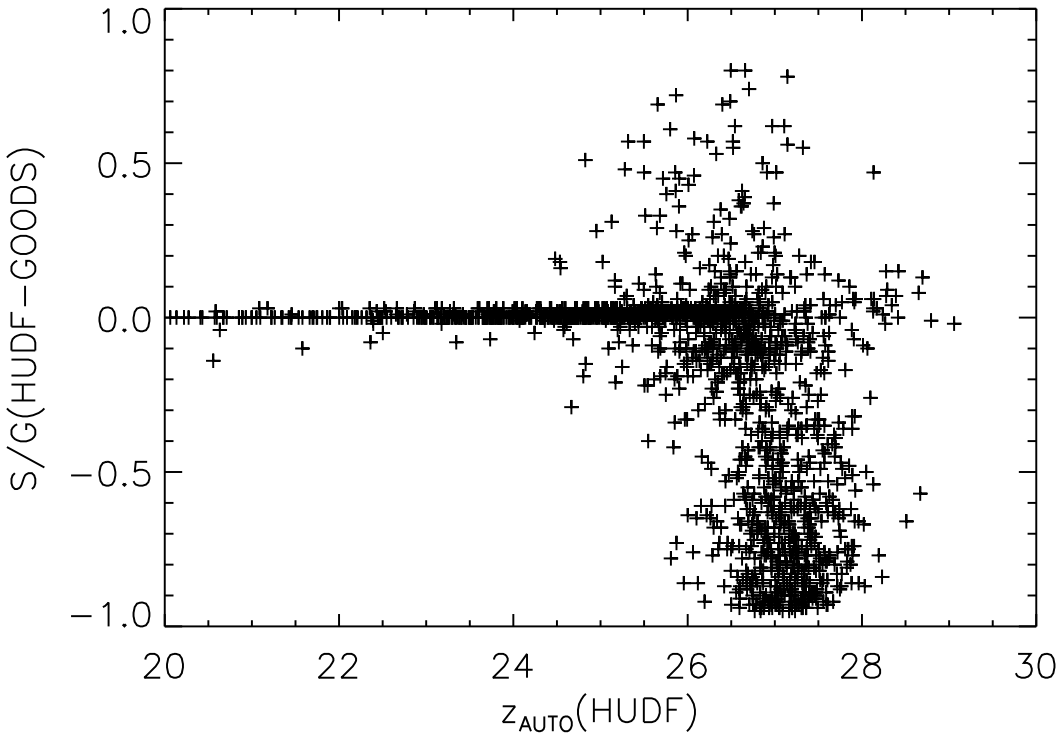

Figure 1.2 Comparison of stellarity in the HUDF and the GOODS.

Table 1.1. Rough Numbers of Dropouts in the HUDF

	redshift window[a]	candidates number
B_{435}-dropouts[b]	$3 < z < 5$	400
V_{606}-dropouts[c]	$4 < z < 6$	200
i_{775}-dropouts[d]	$5 < z < 7$	100
z_{850}-dropouts[e]	$6 < z < 8$	20
Y_{AB}-dropouts[e]	$7 < z < 9$	10
J_{125}-dropouts	$z > 8$	3

[a]The original dropout technique does not allow that an object can drop into different redshift window. The selection is exclusive. But the selected dropouts can actually be found spectrographically at other redshifts. We will introduce the f-factor in Chapter 2 to deal with this.

[b]Chapter 6.

[c]Chapter 5.

[d]Chapter 2 and 4.

[e]Chapter 3.

Chapter 2

GALAXIES AT REDSHIFT SIX

In this chapter, we present a derivation of the rest-frame 1400Å luminosity function (LF) at redshift six from a new application of the maximum likelihood method. We consider the five deepest *HST*/ACS fields, i.e., the HUDF, two UDF05 fields, and two GOODS fields. We work on the latest improved data products, which makes our results more robust than those of previous studies. We use un-binned data and thereby make optimal use of the information contained in the dataset. We focus on the analysis to a magnitude limit where the completeness is larger than 50% to avoid possibly large errors in the faint end slope that are difficult to quantify. We also take into account scattering in and out of the dropout sample due to photometric errors by defining for each object a probability that it belongs to the dropout sample. We find the best fit Schechter parameters to the $z \sim 6$ LF are: $\alpha = -1.87 \pm 0.14$, $M_* = -20.25 \pm 0.23$, and $\phi_* = 1.77^{+0.62}_{-0.49} \times 10^{-3}$ Mpc^{-3}. Such a steep slope suggests that galaxies, especially the faint ones, are the main sources of ionizing photons in the universe at redshift six. We also combine results from all published studies at $z \sim 6$ to determine confidence level at 95% for the LF parameters, namely, $-20.45 < M_* < -20.05$ and $-1.90 < \alpha < -1.55$. The luminosity density has been found not to evolve significantly between $z \sim 6$ and $z \sim 5$, but considerable evolution is detected from $z \sim 6$ to $z \sim 3$. A version of this Chapter has been included in Su & Stiavelli et al. (2011).

2.1 Introduction

Deep imaging surveys, such as the Great Observatories Origins Deep Survey (GOODS, Giavalisco et al. 2004) and the Hubble Ultra Deep Field (HUDF, Beckwith et al. 2006), have been extensively analyzed to study galaxy properties out to the reionization epoch. The rest-frame ultraviolet (UV) galaxy luminosity function (LF) is measured for samples of Lyman break galaxies (LBGs) and used to detect cosmic evolution. The consensus that has developed is that a considerable increase in the space-density of galaxies at the bright end of the LF occurs from redshift $z \sim 6$ (Bunker et al. 2004; Yan & Windhorst 2004; Beckwith et al. 2006; Bouwens et al. 2006)[1] to $z \sim 3$ (e.g., Steidel et al. 1999). However, there are still some discrepancies in the interpretation of this evolution, in terms of density, slope, luminosity, or a combination of these. Bunker et al. (2004) undertake a photometric analysis of the HUDF i_{775}-dropouts and propose that the density increases six-fold from $z \sim 6$ to $z \sim 3$, in agreement with Beckwith et al. (2006). Yan & Windhorst (2004) push the detection limit deeper to magnitude 30, finding a steeper faint slope at $z \sim 6$ compared to $z \sim 3$ by 0.2-0.3. Furthermore, Bouwens et al. (2006) estimate corrections to the measured quantities to account for various observational effects and conclude that the intrinsic luminosity is $\sim$0.8 mag fainter at $z \sim 6$. Their conclusions remain qualitatively unchanged after Reddy & Steidel (2009) recently revisit the LF parameters at $z \sim 3$. On the other hand, ground-based observations, e.g., McLure et al. (2009), find an even stronger luminosity evolution.

Different measurements of the luminosity density (LD) or star formation rate (SFR) also give somewhat different results (e.g., Bunker et al. 2004; Bouwens et al. 2006). It is important to establish whether these observed differences are due to intrinsic differences in the evolution of different galaxy populations or due to issues with the derivation of the LF.

Spectroscopic confirmations of $z \sim 6$ galaxies, e.g., Malhotra et al. (2005), Dow-Hygelund et al. (2007), Hathi et al. (2008) and Vanzella et al. (2009), have already

[1]The results of these groups are summarized in Table 2.4.

proven the effectiveness and robustness of the dropout technique in selecting LBGs. However, the faint LBGs, which are essential to determining the faint-end slope of the LF, have not been spectroscopically confirmed because they require impractically long exposure time on large telescopes.

Therefore, to improve upon the previous studies of the $z \sim 6$ LF and to establish its form, a number of difficult issues should be considered. (a) Optimal use of the data: a single field provides us with only a handful of candidates so that some magnitude intervals contain only very few objects. Thus, it is very important to keep all the information. In order to do so, we use un-binned data. (b) Completeness of the catalogs: the correction to the number of objects observed at faint magnitudes is significant due to the detection incompleteness. We adopt a more moderate magnitude limit than other groups in order to avoid possible uncertainties brought by large corrections. (c) Photometric errors and biases: a strict color cut used for i_{775}-dropout selection may lose real LBGs and is affected by contaminants. For each galaxy within or outside the selection window, we explicitly consider its probability of being an actual LBG by assuming a Gaussian distribution for the photometric error.

On the basis of the HUDF images (Beckwith et al. 2006, hereafter paper I), the UDF05 images (Oesch et al. 2007, hereafter paper II), and the HUDF09 images (Oesch et al. 2010; Bouwens et al. 2010a), we are now in a position to study properties of LBGs from $z \sim 0$ to beyond $z \sim 8$ utilizing *Hubble Space Telescope*'s (*HST*) unparalleled deep optical and infrared (IR) view. In this paper, we plan to further develop techniques to derive the LF at $z \sim 6$ using the procedures used for $z \sim 5$ galaxies in paper II. In particular, we apply the maximum likelihood (ML) method, which is independent of clustering in our sample, to derive the LF and examine whether star forming galaxies, especially the faint ones, are responsible for re-ionizing or keeping the universe ionized at $z \sim 6$.

2.2 Data

We work on five *HST*/ACS deep fields in four broad bands: F435W (B_{435}), F606W (V_{606}), F775W (i_{775}), and F850LP (z_{850}). We use the most recent and updated version of the data, namely: GOODS South (GOODS-S) & GOODS North (GOODS-N) v2.0 data by Giavalisco & the GOODS Team (2008), the HUDF data from paper I, HUDF NICP12 from paper II, and HUDF NICP34 processed in this work. PyRAF tasks Multidrizzle and Tweakshifts (Koekemoer et al. 2006) help precisely align the images, and SExtractor (Bertin & Arnouts 1996) is run in double-image mode with z_{850} as the detection band to generate the catalogs. Our survey covers ~ 350 arcmin^2 to a magnitude limit of $z_{850} \sim 29$, identifying ~ 1100 LBG candidates at $z \sim 6$, with an average number of 350 per realization, as shown in Table 2.1.

We have not made use of the WFC3/IR data that are becoming available on these fields for two main reasons: (a) The IR data are not available over the full fields, especially only a small portion of the GOODS has been covered. This would force us to reduce the sample size greatly. (b) We think an important component of this work is a comparison with other published results which are based on the simple one color selection rather than a full two-color selection. We do make a quick check of the IR information in the HUDF in Section 2.3.1 and will leave a full investigation for future work.

We also do not use ground based data for two main reasons: (a) The two GOODS fields are already large enough to provide good constraints on galaxies brighter than the knee of the Schechter function. (b) We prefer to work with a homogenous data set in terms of filters and detector QE curves.

2.3 Luminosity Function of LBGs at $z \sim 6$

The completeness function $C(m)$ (m is the apparent/detected magnitude) and the selection function $S(m, z)$ (z is the redshift) are measured by performing recovery simulations in the same way as in paper II, i.e., by inserting artificial galaxies into

our science images and rerunning SExtractor with the same setup as for the original catalog generation. We use a $\beta-$distribution -2.2 ± 0.4 (Stanway et al. 2005) and a size distribution following a scaling of $(1+z)^{-1}$ as in Ferguson et al. (2004). For each redshift bin $\delta z = 0.1$, we thus compute the color a galaxy would have with the randomly chosen $\beta-$value and insert it in the images. The input magnitudes are following a flat distribution from $24-29$, but the selection function is given at observed magnitudes, simply by computing the fraction of galaxies that we insert with the measured output magnitude which is selected by the i_{775}-dropout criteria. $C(m)dm$ is defined as the probability that a galaxy of magnitude m in the images is selected in the catalog, which depends strongly on SExtractor parameters such as DEBLEND. Thus, it is important that the recovery simulations are done using the same SExtractor parameters used to derive the catalog. $S(m,z)dmdz$ represents the probability that a LBG at a given redshift z and at a given observed magnitude, m , satisfies the selection criteria. Naturally, the product of these two functions $C(m)S(m,z)dmdz$ is the probability that a galaxy at redshift, z , is detected with magnitude, m , AND selected as a LBG.

The UV LF can be expressed in Schechter form as,

$$\phi(M) = (0.4 \ln 10)\phi_* 10^{0.4(1+\alpha)(M_*-M)} \exp[-10^{0.4(M_*-M)}] \tag{2.1}$$

with the absolute magnitude $M = m - DM(z) - K_{cor}(z)$, where $DM(z)$ is the distance modulus and $K_{cor}(z)$ is the K-correction from observed z_{850} to rest-frame 1400 Å.

Binned data were initially utilized by many groups to derive the shape of the LF. The observed number of LBGs within the apparent magnitude bin $m_l < m < m_u$ is predicted as

$$N_i = \int dz \frac{dV_C}{dz}(z) \int_{m_l}^{m_u} dm C(m) S(m,z) \phi(M(m,z); \phi_*, M_*, \alpha) \tag{2.2}$$

where dV_C/dz is the comoving volume element of the survey. Binning may lose information, and lead to biased results dependent on the bin size. At the same time, having very few luminous candidates in current high-z surveys, there is uncertainty about the numbers in the bright bins since the candidates could jump into adjacent

bins due to photometric errors. Simulations by Trenti & Stiavelli (2008) show that binning is likely to affect the confidence regions for the best-fitting parameters.

To overcome these drawbacks, in this section we present an improved approach based on the ML method (Fisher 1922; Sandage et al. 1979, STY) to make optimal use of every possible LBG in the fields. As also pointed out by Trenti & Stiavelli (2008), the STY ML estimator relies essentially on un-binned data. We determine the shape of the LF by exploring every single detected dropout. First, we find the probability for each galaxy that it could be selected as a LBG, considering the photometric uncertainty of the catalogs (Section 2.3.2). Second, we choose galaxies randomly by the above probability and run our ML process (Section 2.3.3). Third, we repeat the above step enough times to achieve convergence.

2.3.1 Selection Criteria

We adopt the i_{775}-dropout selection criteria from paper I, i.e.,

$$i_{775} - z_{850} > 1.3, \tag{2.3}$$

$$S/N(z_{850}) > 5, \tag{2.4}$$

$$S/N(V_{606}) < 2 \quad \text{or} \quad V_{606} - z_{850} > 2.8. \tag{2.5}$$

The dominant criterion, i.e., the SExtractor MAG_ISO color $i_{775} - z_{850} > 1.3$, will be further discussed in Section 2.3.2. The signal-to-noise ratio $S/N(z_{850}) > 5$ is demanded for each candidate to largely avoid interlopers (later this subsection) or slope steepening (Appendix A), and to be consistent in comparing with $z \sim 3$ results from Steidel et al. (1999) and with $z \sim 5$ results in paper II. The photometric errors also take into account the correlated errors present in the images as discussed in paper II. In addition, we require for CLASS_STAR < 0.75 if the MAG_AUTO magnitude $z_{850} < 28.0$ for the HUDF, < 27.5 for the UDF05 (NICP34 might be shallower than NICP12 because of the roll issue and a PSF not as tight), and < 26.5 for the GOODS in order to remove stellar contamination at the bright end (e.g., Bouwens et al. 2006, and paper II). Only galaxies with $C(m) > 0.5$ have been included to avoid large

uncertainty corrections (Table 2.2). The selection has been proven to be very efficient and effective. All the spectroscopically confirmed $i_{775} - z_{850} > 1.3$ $z \sim 6$ LBGs through the HUDF/GOODS follow-up surveys (e.g., Malhotra et al. 2005; Vanzella et al. 2009) satisfy our criteria, with only one exception, and no Galactic star could pass the CLASS_STAR test.

We have estimated the possible fraction of interlopers by applying our selection criteria of equations (3)-(5) to a library of ∼3000 synthetic SEDs built on Bruzual-Charlot models (Bruzual & Charlot 2003), adopting the LF derived by Steidel et al. (1999) at $z \sim 3$ and no evolution. The models include the effects of intergalactic absorption (Madau 1995), and span a wide range of metallicities (0.04-2.5 $Z_{\odot}$), dust reddening (no extinction, or eight values logarithmically spaced between $A_V = 0.05$ and 6.4), emission lines (no lines or lines computed from first principles from UV SED for Hydrogen and fit to Cloudy models for metal lines), and different star formation histories (burst, constant at fixed metallicity, constant at evolving metallicity without infall or with infall, two component models with an old component and a young one which may include emission lines). We consider 18 ages logarithmically spaced between 1 Myrs and 18 Gyrs. And no model older than the universe is included. We can see from the resulting redshift distribution (Fig. 2.1) that there is a lower redshift population $z \sim 1, 2$ of galaxies that may be selected as LBGs at $z \sim 6$ due to the aliasing between the Lyman break and the 4000Å break (See e.g., Dahlen et al. 2010, for more discussions). In Fig. 2.2, we have identified our $i_{775} - z_{850} > 1.3$ candidates detected by the WFC3 F105W (Y_{105}) band in the HUDF to verify that our sample does not have many interlopers.

2.3.2 f-factor

Photometric scatter introduces large uncertainties in numbers and magnitudes of the LBG candidates, and therefore, in determined properties of the LF. If a strict color cut such as $i_{775} - z_{850} > 1.3$ was applied, the impact of photometric errors would not be fully explored, and many real LBGs with a little bluer measured color may

be missed due to photometric errors. A relaxed cut, e.g., $i_{775} - z_{850} > 0.9$, on the other hand, suffers from larger contaminations. For example, Malhotra et al. (2005) found five objects at intermediate redshifts and four intrinsic $z \sim 6$ galaxies within $0.9 < i_{775} - z_{850} < 1.3$, which means the contamination rate in the relaxed color window may be as high as $5/(5+4) = 56\%$.

To account for this effect, we calculate the probability that each object is an LBG, which decides how often it could contribute to the later maximum likelihood (ML) process. If $p(m)dm$ is the probability that a galaxy is of magnitude m in the catalog, then the f-factor of $i_{775} - z_{850} > 1.3$ LBG candidates is defined as:

$$f = \int \mathrm{d}z_{850}\mathrm{d}i_{775}\ p(z_{850})p(i_{775}) \tag{2.6}$$

where the integration of i_{775} is taken over $i_{775} - z_{850} > 1.3$. The real magnitude m is assumed to be a Gaussian distribution around its cataloged magnitude m_c (See Appendix A for details). In practice, one could find the values of f-factor with a Monte Carlo method by simply generating Gaussian distributed magnitudes repeatedly to see how often the $i_{775} - z_{850} > 1.3$ color would be satisfied. A 2-σ magnitude limit is adopted if there is no detection in the i_{775}-band.

It is easy to see that $f > 0.5$ when the cataloged $i_{775} - z_{850} > 1.3$ while $f < 0.5$ when the cataloged $i_{775} - z_{850} < 1.3$, and $f = 0.01$ corresponds to the cataloged $i_{775} - z_{850} \sim 0.9$ when the z_{850} and i_{775} errors are both 0.2. All $f \geq 0.01$ galaxies are used in the subsequent ML analysis, i.e., 1% chance of being included in one realization. Table 2.1 shows that essentially about 25% - 50% candidates in each field will participate in one realization, which brings our sample into agreement with other groups within the magnitude window in study, such as Bouwens et al. (2007). (See Fig. 2.3 and Table 2.3.)

2.3.3 V-Matrix

Due to the unique long tail of the ACS z_{850}-filter, the K-correction can be as large as 2.2 mag at $z = 5.7$ and goes down to 0.3 mag at $z = 7.0$. Thus, with distance modulus varying by 0.5 mag there could be a 2.4-mag scatter in UV rest

frame absolute magnitudes in realizations at $5.7 < z < 7$ for any given observed z_{850}-magnitude. In other words, the relation between M and m is very uncertain. Therefore, although it is applicable at where M is relatively insensitive to redshift or the redshift span is relatively small, the effective volume V_{eff} technique does not fit in our case. This forces us to seek a new formalism.

We define the apparent LF as

$$\Phi(m) = \frac{C(m)}{V_{eff}} \int dz S(m,z) \frac{dV_C}{dz}(z) \phi(M; m, z) \tag{2.7}$$

and it does not need to be of Schechter form. The V-matrix is therefore,

$$V(m,z) \equiv C(m) S(m,z) \frac{dV_C}{dz}(z) \tag{2.8}$$

and $V_{eff}(m) = \int dz V(m,z)$. We maximize the likelihood function $\ln \mathcal{L} = \sum_i \ln p(m_i)$ where

$$\begin{aligned} p(m_i) &= \Phi(m_i) / \int dm \Phi(m) \qquad (2.9) \\ &= \int dz V(m_i, z) \phi(M_i) / \int\int dm dz V(m,z) \phi(M) \end{aligned}$$

The integrations are always taken over the region of interest, for example for the HUDF, $5.7 < z < 7.0$ and $24.0 < m < 28.5$. (The bright limit is introduced for calculations only when there is no candidate detected beyond this magnitude, and an even brighter limit will not affect the results since the LF is greatly suppressed at this end.) $C(m)$ has been included in the calculation of $V(m,z)$ so that there is no additional completeness correction factor in $p(m_i)$. [2]

When combining different fields, e.g., the GOODS and the HUDF, no additional rescaling factor is needed in the ML method (Trenti & Stiavelli 2008). The inputs to the ML process are the V-matrix and the magnitudes m of selected candidates. In each realization, candidates are selected from the pool in a probability as to their f-factor. The outputs are M_* and α in as many as possible realizations, when the averages and errors have been convergent. The uncertainty of m considered in the

[2]We note that Marshall (1985) adopted a similar approach to ours and he did not have to take the integration of redshift as shown above since the redshifts of their objects were already known.

ML process only yields minor errors when several hundreds of galaxies are surveyed (Appendix A). ϕ_* is determined by χ^2 fit to the observed LBG densities with respect to the 1-σ 2-parameter contour of M_* and α.

The LF parameters we derive for $z \sim 6$ are: $\alpha = -1.87 \pm 0.14$, $M_* = -20.25 \pm 0.23$, and $\phi_* = 1.77^{+0.62}_{-0.49} \times 10^{-3}$ Mpc^{-3}, as illustrated in Fig. 2.4. We notice our faint end slope α is slightly steeper than that from some other studies. This could partly be caused by a steeper slope at $z \sim 7$ (e.g., Oesch et al. 2010; Trenti et al. 2010) since we include up to $z = 7$ LBGs in our estimate of the $z \sim 6$ LF.

2.3.4 Evolution of ϕ_*

Since we are investigating a relatively large redshift range $5.7 < z < 7.0$ and finding indication of LF evolution, it is a good sanity check for us to explicitly consider the effect of evolving LF parameters. Assuming M_* and α are uniform in this redshift range, we assign a linear evolution $\phi_*(z) = \phi_*(6.3)[1 - \frac{5}{7}(z - 6.3)]$ and repeat the analysis described in Section 2.3.1 - 2.3.3. We find that $\alpha = -1.92 \pm 0.13$, $M_* = -20.22 \pm 0.21$. The closeness to our derived parameters for no evolution, i.e., $\alpha = -1.87 \pm 0.14$ and $M_* = -20.25 \pm 0.23$, shows that our results are robust with respect to an evolution of the LF normalization within the redshift range of i_{775}-dropouts .

2.3.5 Evolution of M_*

Similar considerations to those in the previous subsection lead us to explore a variation of M_* within the i_{775}-dropout redshift window. We do so by assigning $\mathrm{M}_*(z) = \mathrm{M}_*(5.9) + 0.36(z - 5.9)]$ (Bouwens et al. 2007; Oesch et al. 2010) while keeping uniform values of α and ϕ_*. We find $\alpha = -1.91 \pm 0.08$, which is also within one sigma of our non-evolving derivation.

2.4 Comparison to Other Results

We have verified the internal consistency and robustness of our results and we are now ready to compare them to other studies.

2.4.1 Most Probable $z \sim 6$ LF

To deal with the weighted average of results from different groups, we follow Press (1997). The probability of getting observed variable(s) H_0 from data or measurements D is

$$P(H_0|D) \propto \prod_i (P_{Gi} + P_{Bi}) \tag{2.10}$$

Here $P_{Gi} \sim \frac{1}{\sigma_i} \exp[\frac{-(H_i - H_0)^2}{2\sigma_i^2}]$ and $P_{Bi} \sim \frac{1}{S} \exp[\frac{-(H_i - H_0)^2}{2S^2}]$ are the probability distributions of "good" and "bad" measurements, respectively, where i denotes different measurements, and S should be assigned to be large enough to ensure that measurements do not conflict with each other. When extending this method to two-dimensional analysis, we also consider the correlation between M_* and α (Fig. 2.4). Press (1997) puts almost no weight on those measurements without errors where $P_{Gi} = 0$ and P_{Bi} is widely spread. Instead, we assume here a moderate error of 0.3 for those six groups, i.e., Bouwens et al. (2004), Bunker et al. (2004), Dickinson et al. (2004), Yan & Windhorst (2004), Malhotra et al. (2005), and paper I. Combined with the other four measurements providing errors, i.e., Bouwens et al. (2006), Bouwens et al. (2007), McLure et al. (2009), and this work, we find there is about a 95% chance that $-20.45 < M_* < -20.05$ and $-1.90 < \alpha < -1.55$, assuming all the current studies are independent and correct. (See Table 2.4 and Fig. 2.5.)

2.4.2 $z \sim 5$ LBGs LF revisited

In order to further test the method used here, we derive the faint end slope of the $z \sim 5$ LBG LF using the same catalogs and the same selection criteria as those in paper II. To study the HUDF and NICP12 data that lack enough bright candidates to determine M_*, we fix $M_* = -20.7$ to find $\alpha = -1.72 \pm 0.04$, which is in agreement

with the previous results (their Table 3). Thus, our method, designed to deal with the varying K-correction in z_{850} and to account for additional uncertainties, is equivalent to our previous method in the simpler V_{606}-dropout case.

2.4.3 $z = 3 \sim 6$ Luminosity Density

The luminosity density (LD) at redshift z equals $\int L\phi(L)dL = L_*(z)\phi_*(z)\int_{x_0}^{\infty} x^{1+\alpha}e^{-x}dx$, where $x = L/L_*(z)$. We find there is considerable evolution between $z \sim 6$ and $z \sim 3$, but no statistically significant evolution between $z \sim 6$ and $z \sim 5$. More details are in Table 2.5 and Fig. 2.7 where $x_0 = aL_*(3)/L_*(z)$ and a=0.3,0.2,0.04. At lower redshifts there are fewer recombinations in the diffuse medium and therefore the required flux density to keep the universe ionized increases with increasing redshift. If the universe has finished reionizing at $z \sim 6$, then it will be kept ionized at $z \sim 5$ since the required LD at $z \sim 5$ is less than that at $z \sim 6$ and the observed ones are close to each other.

2.5 Conclusions

In this paper, we have reported the results of a study of a large sample of faint LBGs in the redshift interval $5.7 < z < 7.0$. Working on the five deepest *HST* fields with their most updated data, we account for the effect of photometric errors by introducing the factor f as the probability of each galaxy to be an LBG. We employ un-binned data to keep all the information and to avoid bias, and we develop a modified ML process to reduce the effect of the uncertain relation between M and m. Our best-fitting Schechter function parameters of the rest-frame 1400Å LF at redshift $z \sim 6$ are: $\alpha = -1.87 \pm 0.14$, $M_* = -20.25 \pm 0.23$, and $\phi_* = 1.77^{+0.62}_{-0.49} \times 10^{-3}$ Mpc^{-3}, which suggest evolution of M_*, possible steepening of α, and no change of ϕ_* compared to their values at $z \sim 3$. Such a steep slope suggests that galaxies, especially the faint ones, are possibly the main sources of ionizing photons in the universe at redshift six (Stiavelli et al. 2004b). Combining ten previous studies at

$z \sim 6$ with the extended Press method, we find that the most probable LF favors $-20.45 < M_* < -20.05$ and $-1.90 < \alpha < -1.55$ at the 95% confidence level. The LD has been found not to evolve significantly between $z \sim 6$ and $z \sim 5$, but considerable change is detected from $z \sim 6$ to $z \sim 3$.

If α remains constant from $z \sim 6$ to $z \sim 3$ as stated by e.g., Bouwens et al. (2007) and Reddy & Steidel (2009), it will be difficult to tell the intrinsically evolving parameter, M_* or ϕ_*, from faint LBGs only, while too few bright LBGs are found due to the limited area of current deep surveys. Ground-based surveys such as the Subaru Deep Field (Shimasaku et al. 2005; McLure et al. 2009) are extremely efficient in detecting bright LBGs in a large field of view and might clarify whether M_* or ϕ_* alone is not responsible for the change of LF, while splitting the z_{850}-band into two separate bands may be useful to isolate the effect of a possible slope steepening (Shimasaku et al. 2005). We look forward to including IR data from WFC3 on board *HST* to improve the selection of $z \sim 6$ LBG candidates, and the bright end of the LF will be better determined when the data from CANDELS/ERS (e.g., Bouwens et al. 2010a) and the BoRG survey (Trenti et al. 2011) are becoming available.

Table 2.1. Dropouts in Our Sample

	HUDF	GOODS-S	GOODS-N	NICP12	NICP34
N_{tot}[a]	115	373	502	120	54
N_s[b]	58.1±2.3	103.1±6.5	116.2±7.0	33.9±3.0	23.5±5.7

[a]Total number of galaxies in our candidates pool.

[b]Average number of galaxies in one realization.

Table 2.2. Completeness of the Fields

z_{850}	HUDF	NICP12	NICP34	GOODS
24.25	0.95	0.95	0.96	0.96
24.75	0.94	0.94	0.95	0.96
25.25	0.93	0.94	0.94	0.95
25.75	0.92	0.93	0.93	0.94
26.25	0.91	0.92	0.92	0.86
26.75	0.89	0.91	0.87	0.61
27.25	0.87	0.86	0.70	0.30
27.75	0.79	0.72	0.43	0.10
28.25	0.60	0.47	0.19	...
28.75	0.37	0.23	0.07	...

[a]Central bin magnitude.

[b]Only data with completeness above half are considered to avoid large uncertainty corrections.

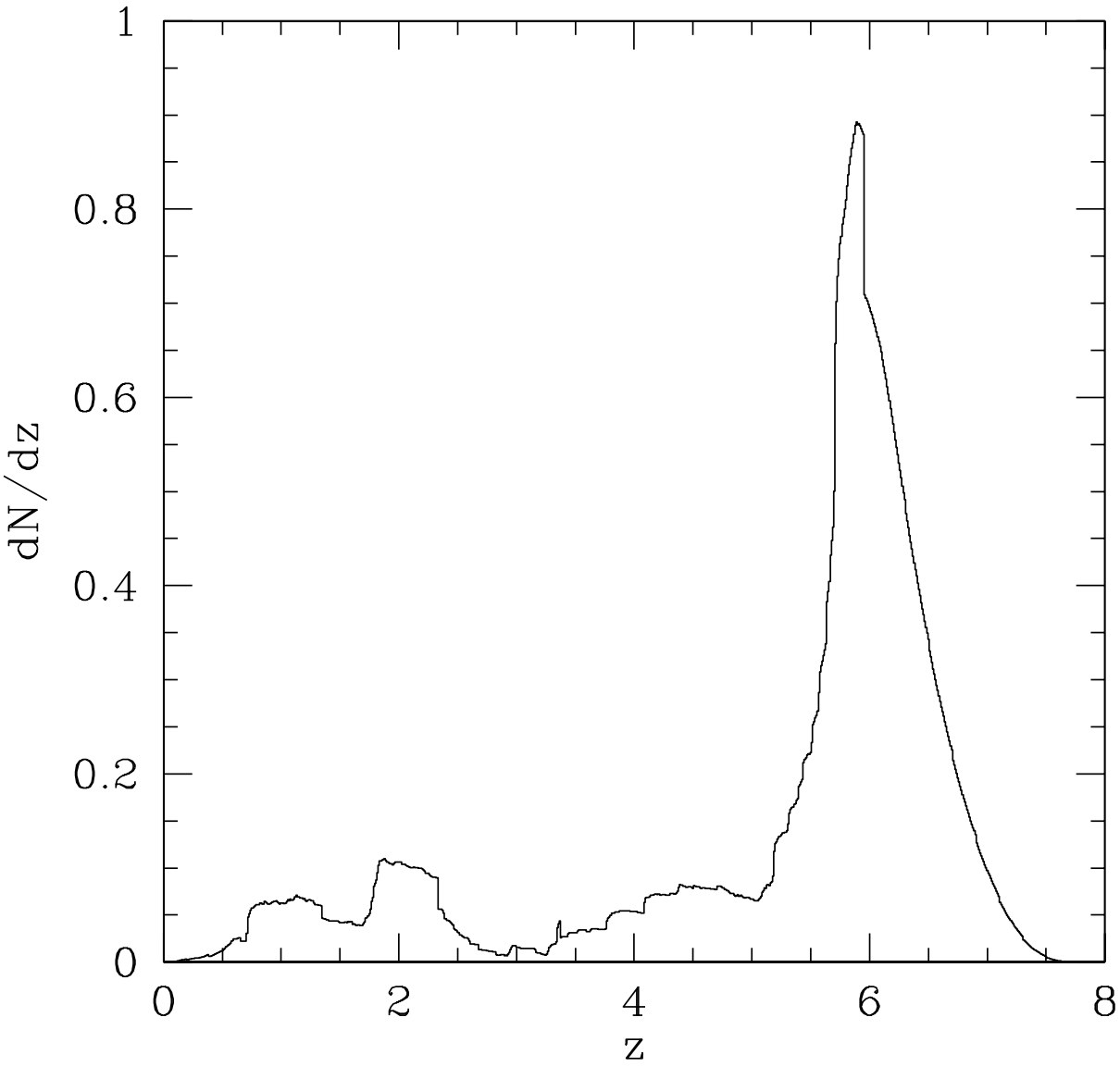

Figure 2.1 Predicted redshift distribution for i_{775}-dropouts as derived assuming synthetic SEDs and a non-evolving LF in the redshift window $5.7 < z < 7$. The total interloper fraction is estimated to be 24% and is primarily contributed by lower redshift galaxies selected as LBGs due to the aliasing between the Lyman break and the 4000Å break. The model is conservative and at the relatively bright end ($z_{850}< 27.5$) comparison with Malhotra et al. (2005) shows a factor of two fewer interlopers than predicted by the model.

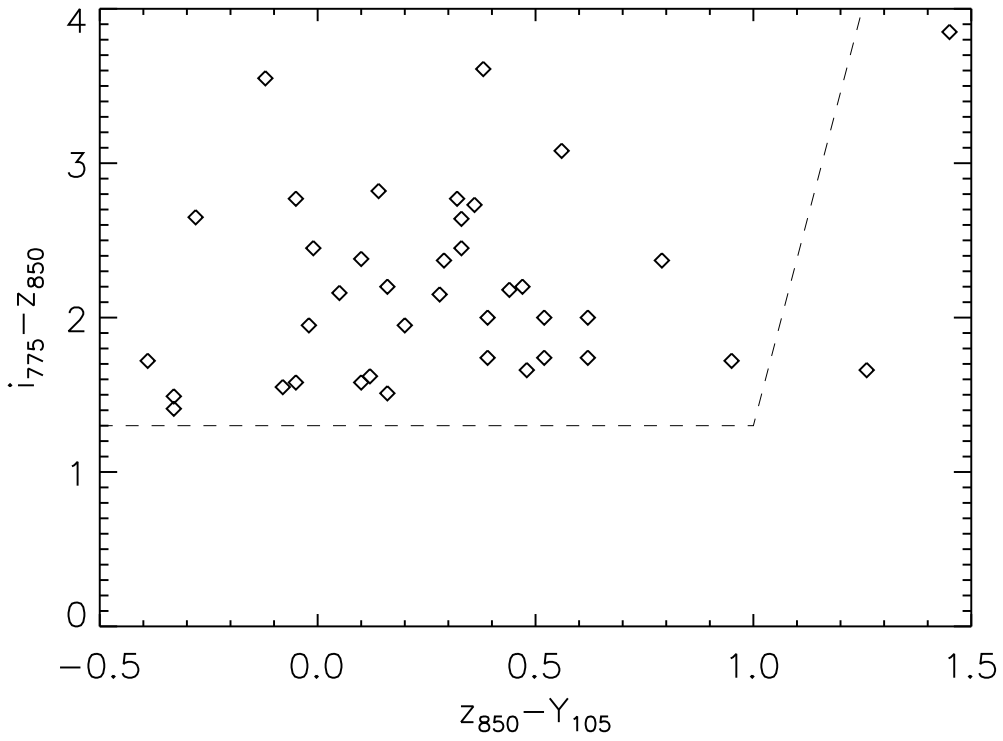

Figure 2.2 Color-color diagram of the HUDF $i_{775}-z_{850}>1.3$ candidates. z_{850} image is rescaled to match Y_{105} to get the z_{850}-Y_{105} color. The dash lines give a possible i_{775}-dropout selection criterion, namely $i_{775}-z_{850}>1.3$ and z_{850}-$Y_{105}<1+0.09(i_{775}-z_{850}$-1.3).

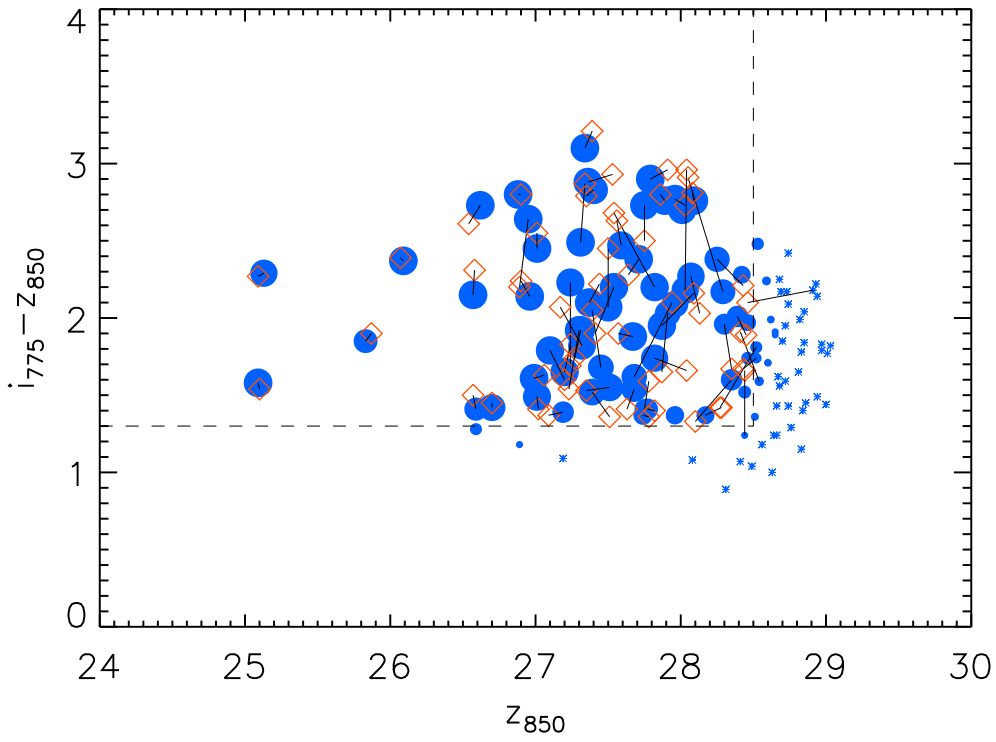

Figure 2.3 Color-magnitude diagram of the HUDF candidate pool. Candidates are indicated as filled circles whose radius is proportional to the f-factor, and asterisks are those objects with f-factor less than 0.2. The diamonds are i_{775}-dropouts selected in one realization for use in later ML process, and the line segments connect the cataloged and realized positions in the diagram.

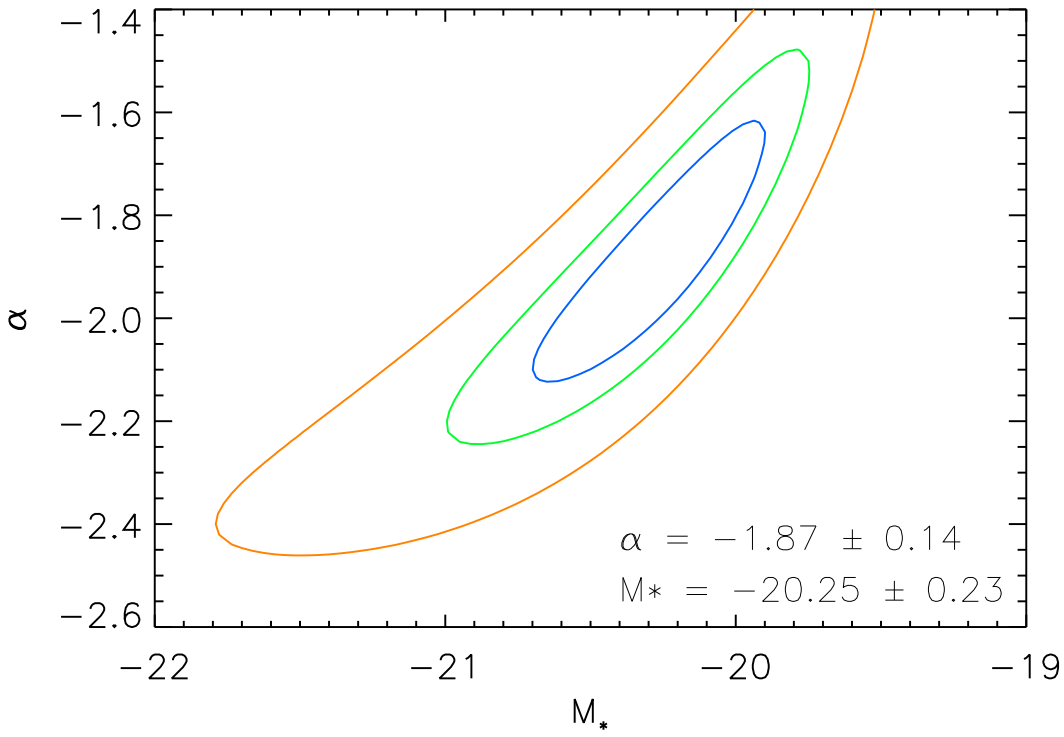

Figure 2.4 Likelihood contour for the best fit Schechter parameters of the $z \sim 6$ LF. The contours, inner to outer, stand for 1-parameter 1-σ, 2-parameter 1-σ, and 1-parameter 2-σ likelihood contours averaged over realizations for use in the ML process.

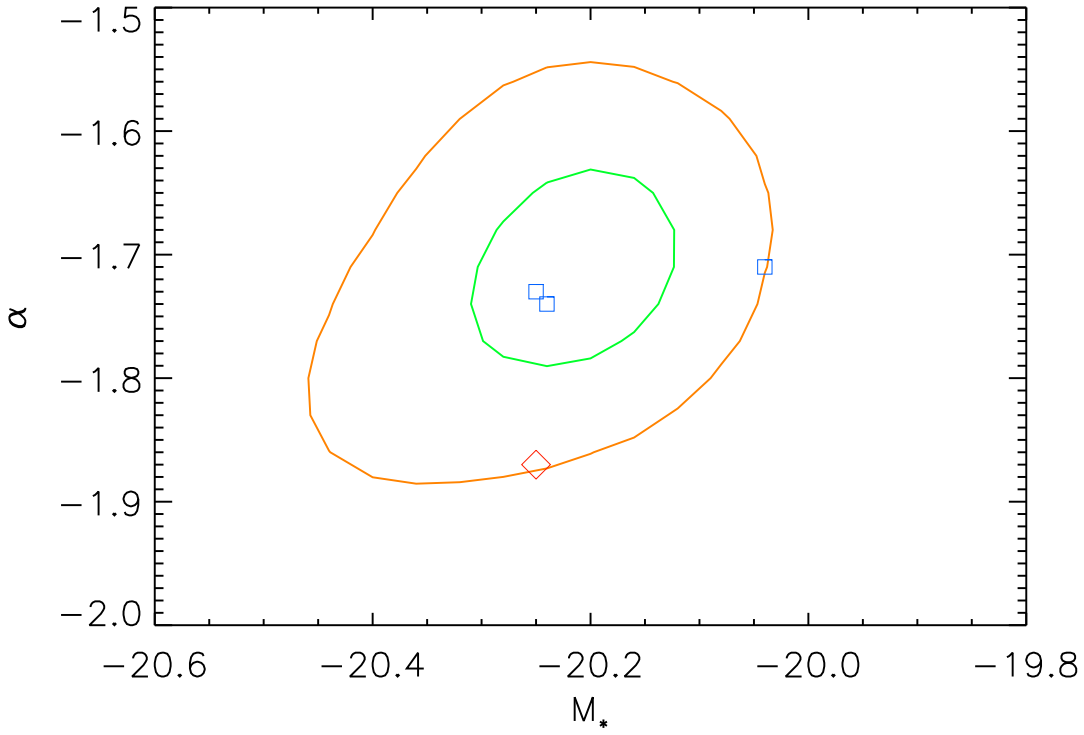

Figure 2.5 Most probable parameter space at $z \sim 6$ based on ten studies. The inner contour includes 68% probability and the outer 95%, assuming all the studies are independent and correct. Two nearby squares are from Bouwens et al. (2006, 2007), a third square is from McLure et al. (2009) who combine their data with Bouwens et al. (2007), and the diamond is from this work. As illustrated in Fig. 2.4, M_* and α are strongly correlated, so we do not plot their error bars, which can be found in Table 2.4.

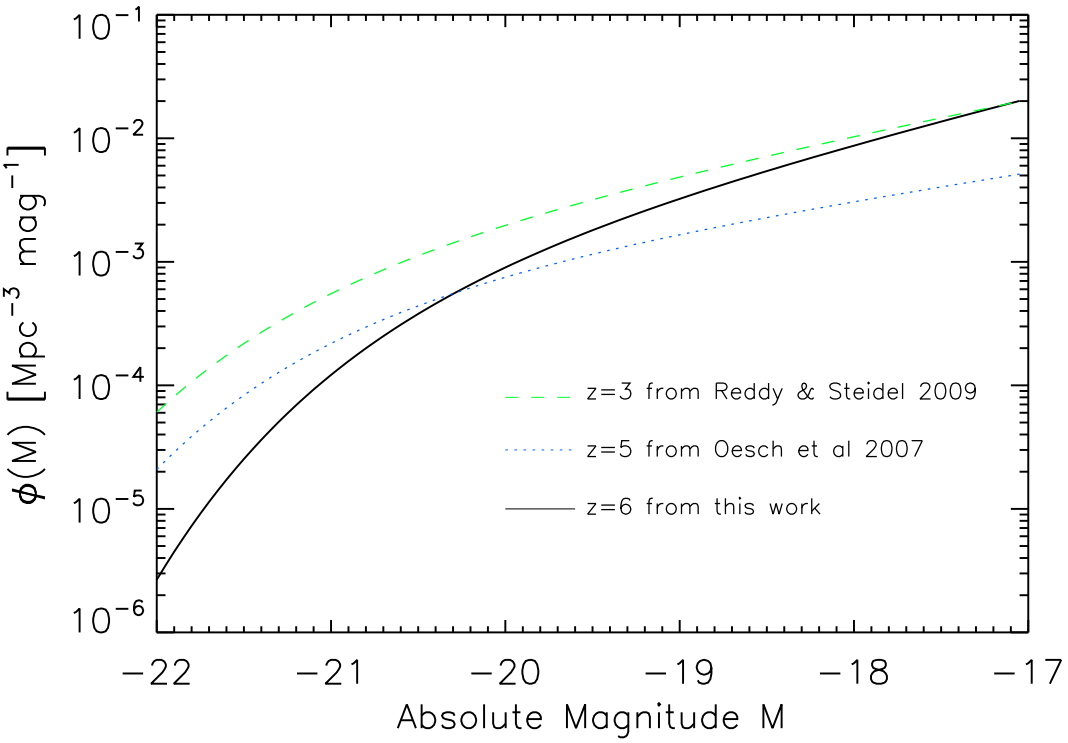

Figure 2.6 Luminosity function from $z \sim 3$ to $z \sim 6$.

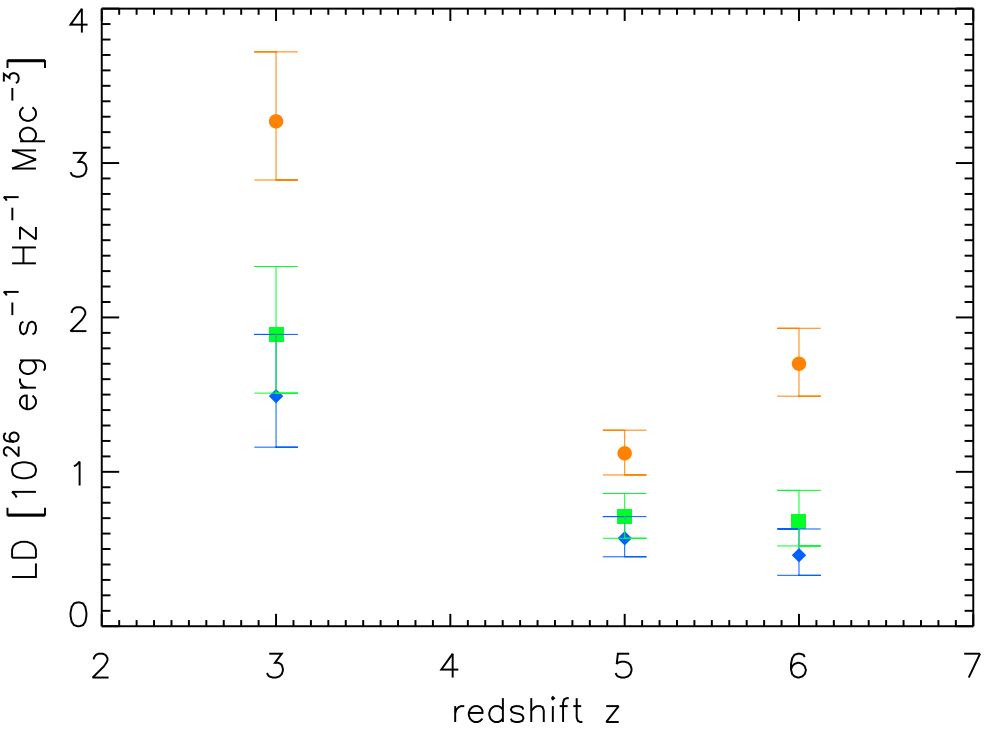

Figure 2.7 Luminosity density from $z \sim 3$ to $z \sim 6$ integrated to 0.3 (diamonds), 0.2 (squares), 0.04 (circles) of $L_*(z = 3)$. $z \sim 3$ data calculated from Reddy & Steidel (2009), $z \sim 5$ data calculated from paper II, and $z \sim 6$ data calculated from this work. See Table 2.5 for the numbers.

Table 2.3. Binned numbers of i_{775}-dropouts in the HUDF

$z_{850}{}^{(1)}$	$N_c{}^{(2)}$	$N_f{}^{(3)}$	$N_s{}^{(4)}$
24.75	0	0.00	0.01±0.12
25.25	2	1.95	1.94±0.25
25.75	1	0.83	0.84±0.39
26.25	1	1.00	1.26±0.50
26.75	8	8.42	8.11±1.47
27.25	16	15.52	16.54±1.98
27.75	21	19.22	18.07±2.34
28.25	14	11.13	11.30±2.19

[a]for illustration only, not for later calculations.

(1)Central bin magnitude.

(2)Number of $i_{775} - z_{850} > 1.3$ i_{775}-dropouts from the catalog without corrections.

(3)Number of i_{775}-dropouts weighted with their f-factor.

(4)Number of i_{775}-dropouts in simulations considering f-factor.

Table 2.4. Studies of the $z \sim 6$ Luminosity Function

References	Fields[a]	N[b]	α	M_*
Bouwens et al. (2004)	UDF PFs (28.1)	30	-1.15	-20.26
Bunker et al. (2004)	HUDF (28.5)	54	<=-1.60	-20.87
Dickinson et al. (2004)	GOODS (26.0)	5	-1.60 (fixed)	-19.87
Yan & Windhorst (2004)	HUDF (30.0)	108	(-1.90,-1.80)[c]	-21.03
Malhotra et al. (2005)	HUDF (27.5)	23[d]	-1.80 (fixed)	-20.83
paper I	HUDF (29.0)	54	-1.60 (fixed)	-20.5
Bouwens et al. (2006)	HUDF (29.2) ...[e]	506	-1.73±0.21	-20.25±0.20
Bouwens et al. (2007)	HUDF (29.3) ...[f]	627	-1.74±0.16	-20.24±0.19
McLure et al. (2009)	UDS (26.0)	157[g]	-1.71±0.11	-20.04±0.12
this work	HUDF (28.5) ...[h]	1164	-1.87±0.14	-20.25±0.23

[a]The fields and z_{850}-band detection limit studied by the reference.

[b]The number of candidates.

[c]$-1.9 < \alpha < -1.8$.

[d]all spectroscopically confirmed.

[e]HUDF (29.2)+HUDF-Ps (28.5)+GOODS (27.5).

[f]HUDF (29.3)+HUDF05 (28.9)+HUDF-Ps (28.6)+GOODS (27.6).

[g]plus binned data points from Bouwens et al. (2007).

[h]HUDF (28.5)+UDF05 (28.0)+GOODS (27.5)

Table 2.5. Evolution of the Luminosity Density

	Reddy & Steidel (2009) ($z \sim 3$)	paper II ($z \sim 5$)	this work ($z \sim 6$)
M_*	-20.97±0.14	-20.78±0.21	-20.25±0.23
α	-1.73±0.13	-1.54±0.10	-1.87±0.14
${\phi_*}^{\rm b}$	1.71±0.53	$0.9^{+0.3}_{-0.3}$	$1.77^{+0.62}_{-0.49}$
${L_*}^{\rm c}$	$1.06^{+0.15}_{-0.13}$	$0.89^{+0.19}_{-0.16}$	$0.55^{+0.13}_{-0.11}$
LD0.3[d]	$1.49^{+0.40}_{-0.33}$	$0.57^{+0.14}_{-0.12}$	$0.46^{+0.17}_{-0.13}$
LD0.2	$1.89^{+0.44}_{-0.38}$	$0.71^{+0.15}_{-0.14}$	$0.68^{+0.20}_{-0.16}$
LD0.04	$3.27^{+0.45}_{-0.38}$	$1.12^{+0.15}_{-0.14}$	$1.70^{+0.23}_{-0.21}$

[a]See Fig. 2.7 for the graph.

[b]in units of 10^{-3} Mpc^{-3}.

[c]in units of 10^{29} erg s^{-1} Hz^{-1}.

[d]in units of 10^{26} erg s^{-1} Hz^{-1} Mpc^{-3}. LD0.3 means that the LD is integrated from $0.3L_*(z=3)/L_*(z)$.

Chapter 3

HIGH-REDSHIFT GALAXIES IN THE DEEP FIELDS

In this chapter, we present a derivation of the rest-frame 1400Å luminosity function (LF) at redshift four to nine from a new application of the maximum likelihood method. We consider the deepest *HST*/ACS fields, i.e., the HUDF, two UDF05 fields, with two GOODS fields, and the deepest WFC3/IR fields, i.e., three HUDF09 fields, with the ERS fields. We work on the latest improved data products with more candidates, which makes our results more robust than those of previous studies. Similar to what has been done in Chapter 2 for the $z \sim 6$ LF, we use unbinned data and thereby make optimal use of the information contained in the dataset. We focus on the analysis to a magnitude limit where the completeness is larger than 50% to avoid possibly large errors in the faint end slope that are difficult to quantify. We also take into account scattering in and out of the dropout sample due to photometric errors by defining for each object a probability that it belongs to the dropout sample. We find the best fit Schechter parameters at $z \sim 7$ LF are: $\alpha = 1.73 \pm 0.15$, at $z \sim 8$ $\alpha = 1.79 \pm 0.14$, assuming $M*$ evolution $M_*(z) = -20.25 + 0.36\ (z - 6)$. Instead, at $z \sim 7$ $M_* = -19.96 \pm 0.16$, at $z \sim 8$ $M_* = -19.66 \pm 0.17$, assuming no α evolution. We also study the evolution of the LF parameters within the redshifts window $4 < z < 9$ in a unified scheme. The best description of the evolution of the LF from

1.5 Gyr to 500 Myr is given by: a constant ϕ_*, a slowly steepening α, and a relatively rapidly dimmed M_* towards higher redshifts.

3.1 Introduction

The new Wide Field Camera 3 (WFC3) onboard the Hubble Space Telescope (HST) provides us ultra-deep near-infrared (near-IR) imaging to faint magnitudes $26 < m_{AB} < 30$, which makes the study of z≥7 galaxies much more ready than before. A large number of papers (e.g., Bouwens et al. 2010a, 2010b, Bunker et al. 2010, Finkelstein et al. 2010, Grazian et al. 2010, Labbé et al. 2010, Lorenzoni et al. 2011, McLure et al. 2010, 2011, Oesch et al. 2010, 2011, Wilkins et al. 2010, 2011, and Yan et al. 2010) based on the WFC3/IR data sets have appeared for the last two years. Ground-based spectroscopy has confirmed several z>7 galaxies (Vanzella et al. 2011 and Lehnert et al. 2010) selected by the dropout technique (Castellano et al. 2010 and Bouwens et al. 2010a).

A consistent picture of evolution has been built up. UV continuum of galaxies appears progressively bluer with increasing redshift (Dunlop et al. 2011, Finkelstein et al. 2010 and Bouwens et al. 2010b) and their stellar masses are on average smaller than those of their low-z counterparts (Labbe et al. 2010) while the morphologies remain essentially unchanged (Oesch et al. 2010). Detailed comparisons between the high-redshift samples have been performed by several groups, e.g., Finkelstein et al. (2010) and McLure et al. (2010), and the overlap is reasonably good. Performing SED fitting to the optical and IR photometry of 300 objects in the HUDF field, McLure et al. (2010) identify 49 z>5.9 galaxies, recovering all but the faintest one of the 16 z_{850}-drops by Oesch et al. (2010) and all 5 of the Y_{105}-drops by Bouwens et al. (2010a). However, at faint magnitudes, photometric uncertainties bring more objects jumping into the selection window (Appendix A), so that more candidates are likely at lower redshifts. Therefore, faint sources should be examined carefully and a probabilistic selection is required and beneficial to avoid bias.

Robertson (2010) uses the Fisher matrix calculations to estimate the marginalized

(unmarginalized) contraints of $\delta M_* \sim 0.5$ (0.15) mag and $\delta\alpha \sim 0.4$ (0.1) from the completed HUDF09 and ERS data. Trenti et al. (2010) use their improved conditional LF method to find $M_* = -20.0$ and $\alpha = -1.84$ at $z \sim 7$ if their values at $z \sim 6$ are adopted from Bouwens et al. (2007). Their model also predicts a dimming of $\sim$0.3 in M_* and a steepening of $\sim$0.1 in α at redshifts $4< z <9$. Since the expected change of the parameters is comparable to the uncertainties constrained from the limited data, particular care is needed to establish the correct error bars.

Similar to Chapter 2, we have introduced a new statistical approach to study the rest-frame UV luminosity function (LF) of high-redshift galaxies.[1] We use un-binned data to keep all the information, adopt a more moderate magnitude limit than other groups to avoid possible uncertainties brought by large corrections, and consider the probability of each galaxy of being an actual LBG by assuming a Gaussian distribution for the photometric error. By doing so with the most updated data, we find a steeper faint-end slope $\alpha = -1.87\pm0.14$, a lower characteristic luminosity $M_* = -20.25\pm0.23$, and relatively constant density $\phi_* = 1.77^{+0.62}_{-0.49} \times 10^{-3}$ Mpc^{-3}, compared to those at lower redshifts.

Now we are going to study the evolution of the LF during one billion years, back to when the age of the universe is only 500 million years. How the LF evolves with the cosmic time will greatly help us understand the reionization process of the universe. High-redshift galaxy LF extending to low masses is also useful to weigh neutrinos (Jose et al. 2011) because the presence of massive neutrinos suppresses the growth of perturbations, thereby leading to a decreased abundance of collapsed dark matter halos.

This chapter is organized as follows. In Section 2, we discuss the observations, our data reduction process and our photometry measurement and catalogue production technique. In Section 3, our candidate selection procedure is described. In Section 4, we investigate the properties of these objects, including their LF at $z \sim 7$ and 8. In Section 5, we apply our method at $z \sim 6$ to the whole redshift window we are

[1]Mortlock et al. (2011) have a different approach to a probabilistic selection of high-redshift quasars.

interested in, 4<z<9. In Section 6, we present our conclusions.

3.2 Data

We have a large sample of galaxies in the deep fields observed by the *HST*: the GOODS fields (PI: Mauro Giavalisco, Mark Dickinson), the HUDF field (PI: Steven Beckwith, Rodger Thompson), the HUDF05 fields (PI: Massimo Stiavelli), the HUDF09 fields (PI: Garth D. Illingworth), the ERS field (PI: O'Connell), and the BoRG fields (PI: Michele Trenti). To maintain uniformity of the bands, we could not use the CANDELS (PI: Sandra Faber, Henry C. Ferguson; Grogin et al. 2011) data, also because it is difficult to separate $z \sim 7$ and $z \sim 8$ galaxies without the very near infrared Y-band observations, a band between F850LP and F125W. We have a full view of the SEDs via four optical bands: F435W (B_{435}), F606W (V_{606}), F775W (i_{775}), and F850LP (z_{850}), and three NIR bands: F105W (Y_{105})/F098M(Y_{098}), F125W (J_{125}), and F160W (H_{160}).

The full two-year images are drizzled (Koekemoer 2006) onto a final grid of 0".06/pix, with matched astrometry to the HUDF (Beckwith et al. 2006), the HUDF05 (Oesch et al. 2007), and the GOODS-South (GOODSv2.0, Giavalisco et al. 2004). SExtractor (v2.5.0, Bertin & Arnouts, 1996) is run in double-image mode with J_{125} as the detection band to generate the IR catalogs. The optical images are re-processed to match the point-spread function (PSF) in the IR images for the study of color.

3.3 Selection

We select $z \sim 7$ galaxies by the same selection criteria as Oesch et al. (2010), i.e.,

$$z_{850} - Y_{105} > 0.8 \tag{3.1}$$

$$z_{850} - Y_{105} > 0.9 + 0.75\ (Y_{105} - J_{125}) \tag{3.2}$$

$$z_{850} - Y_{105} > -1.1 + 4\ (Y_{105} - J_{125}) \tag{3.3}$$

$$S/N(J_{125}) > 5 \tag{3.4}$$

$$S/N(Y_{105}) > 5 \tag{3.5}$$

and less than 2-σ detection in other optical bands. Some different selection criteria employed by different groups may reach very different numbers of candidates, whereas their results of the LF are comparable within the errors (Grazian et al. 2010).

For the ERS fields, due to a different Y-band (Y_{098} instead of Y_{105}) used, the selection criteria are modified to

$$z_{850} - J_{125} > 0.9 \tag{3.6}$$

$$z_{850} - J_{125} > 0.8 + 1.1\ (J_{125} - H_{160}) \tag{3.7}$$

$$J_{125} - H_{160} < 0.5 \tag{3.8}$$

$$z_{850} - J_{125} > 0.4 + 1.1\ (Y_{098} - J_{125}) \tag{3.9}$$

$$Y_{098} - J_{125} < 1.25 \tag{3.10}$$

$$S/N(J_{125}) > 5 \tag{3.11}$$

$$S/N(Y_{098}) > 5 \tag{3.12}$$

and less than 2-σ detection in other optical bands.

To find $z \sim 8$ galaxies, we ask for similar selection criteria as Bouwens et al.

(2010a),

$$Y_{105} - J_{125} > 0.8 \tag{3.13}$$

$$J_{125} - H_{160} < 0.5 \tag{3.14}$$

$$J_{125} - H_{160} < 0.2 + 0.12\ (Y_{105} - J_{125}) \tag{3.15}$$

$$S/N(J_{125}) > 5 \tag{3.16}$$

$$S/N(H_{160}) > 5 \tag{3.17}$$

and less than 2-σ detection in any optical bands. For the ERS fields,

$$Y_{098} - J_{125} > 1.25 \tag{3.18}$$

$$J_{125} - H_{160} < 0.5 \tag{3.19}$$

$$S/N(J_{125}) > 5 \tag{3.20}$$

$$S/N(H_{160}) > 5 \tag{3.21}$$

and less than 2-σ detection in any optical bands.

By assuming Gaussian distribution in magnitudes, we calculate the f-factor for each galaxy, i.e., its probability to satisfy the above color criteria. All $f \geq 0.01$ galaxies are used in the subsequent ML analysis, i.e., 1% chance of being included in one realization. Visual inspection of the images is also important to exclude some artifacts.

Astronomers have designed many methods to minimize contaminations. First, Galactic brown dwarfs can be mostly excluded by their high stellarity (e.g., Chapter 4), especially for the brighter ones. Second, faint spurious sources can be removed by visual inspection of the images and estimated by studying inverted images. Third, transient objects such as supernovae may have unusually red color. Fourth, photometric scatter brings objects from outside the selection window but can be carefully handled by f-factor technique (Chapter 2) and considerable S/N (Appendix A). Fifth, galaxies with prominent Balmer 4000 Å break can be identified using additional color information. However, the contamination rate at $z \sim 7$ determined by simulations is sometimes uncertain. Pentericci et al. (2011) confirm 5 galaxies at $6.7 < z < 7.1$ out

of the 20 z-dropouts observed, which is systematically below the expectations drawn on the basis of lower-z observations (e.g., Vanzella et al. 2010).

3.4 Luminosity Function

Adopting the STY79 procedure (Sandage, Tammann, & Yahil 1979) as in Chapter 2, we maximize the likelihood function $\ln \mathcal{L} = \sum_i \ln p(m_i)$ where

$$p(m_i) = \int dz V(m_i, z)\phi(M_i) / \iint dm dz V(m, z)\phi(M) \tag{3.22}$$

$$V(m, z) \equiv C(m)S(m, z)\frac{dV_C}{dz}(z) \tag{3.23}$$

Here $C(m)$ is the completeness function, $S(m, z)$ is the selection function, and $\frac{dV_C}{dz}(z)$ is the comoving volume element of the survey.

We compare $S(m, z)$ of different fields at $z \sim 6$ in the Fig. 3.1. The function is very close to unity and drops rapidly near the detection limit of the surveys. When shifting $S(m, z)$ of different fields according to their depth, the function is close to universal. We also expect the same trend at $z \sim 7$ and 8 so that we have tried the results with a mocked $S(m, z)$ for the ERS fields.

3.4.1 LF at $z \sim 7$

As we can see from Table 3.1, there are 23 objects in the HUDF field having a probability larger that 1% to be a $z \sim 7$ galaxies. In addition, there are 33 possible $z \sim 7$ sources in the HUDF09-01 field, 26 in the HUDF09-02 field, and 17 in the ERS fields. We put their photometric information into the ML process to find the best fit to the Schechter parameters $\alpha = 1.73 \pm 0.15$, assuming $M*$ evolution $M_*(z) = -20.25 + 0.36\ (z - 6)$, as in Chapter 2 adopted from Bouwens et al. (2007); Oesch et al. (2010).

The UV spectral slope β adopted from Mclure et al. (2011)

$$\beta = 4.43\ (J_{125} - H_{160}) - 2.0 \tag{3.24}$$

have been found to be very blue $\beta \approx -2 \sim -3$ (Bouwens et al. 2010, Lebbé et al. 2010, and McLure et al. 2011). Our Table 3.1 also confirms this.

In Table 3.2, we list all the $z \sim 7$ LF studies so far on the fields with the WFC3/IR observations. Their colors can be found in Fig. 3.2. Similar results are found for the case of the $z \sim 6$ LF, and later the $z \sim 8$ LF. Different groups marginally agree with each other.

3.4.2 LF at $z \sim 8$

As we can see from Table 3.3, there are 12 objects in the HUDF field having the probability larger than 1% to be a $z \sim 8$ galaxies. In addition, there are 23 possible $z \sim 8$ sources in the HUDF09-01 field, 17 in the HUDF09-02 field, and 4 in the ERS fields. We put their photometric information into the ML process to find the best fit to the Schechter parameters $\alpha = 1.79 \pm 0.14$, assuming $M*$ evolution $M_*(z) = -20.25 + 0.36\ (z - 6)$. It should be pointed out that there are very few candidates in the ERS fields while many more in the HUDF09 fields. Since we have exactly the same processes as searching for $z \sim 7$ galaxies, the abnormality in number is possibly due to cosmic variance. Overdensity or under-density has been observed in several fields.

In Table 3.4, we list all the $z \sim 8$ LF studies so far on the fields with the WFC3/IR observations. Their colors can be found in Fig. 3.3.

3.5 A Unified Frame During One Billion Years

In Chapter 2, we have studied the LF at $z \sim 6$ in the HUDF field, NICP12 field, NICP34 field, and two GOODS fields to find $\alpha = -1.87 \pm 0.14$, $M_* = -20.25 \pm 0.23$, and $\phi_* = 1.77^{+0.62}_{-0.49} \times 10^{-3}$ Mpc^{-3}. We also apply the same technique to the z$\sim$5 LF to find $\alpha = -1.72 \pm 0.04$ with $M_* = -20.7$ fixed in the HUDF field and NICP12 field. In the previous sections of this chapter, we have learned the LF at $z \sim 7$ and 8 in the HUDF field with the exactly same procedure. Being confident about the statistical

significance of LF evolution results, we attempt to characterize it better by analyzing all data simultaneously. Therefore, for the next step, we would like to study the evolution of the LF at 4<z<9 in a unified frame. When applied consistently to data sets gathered using the same method it should be a good way to compare samples at different redshifts without a priori knowledge of the underlying source population to discover significant evolution of the source populations (Beckwith et al. 2006).

Instead of determining the LF at each redshift window, we extend our ML method to estimate the LF 4<z<9 in a single likelihood function $\ln \mathcal{L} = \sum_i \ln p(m_i)$,

$$p(m_i) = \int dz V(m_i, z)\phi(M_i)g_i(z) / \iint dm dz V(m, z)\phi(M)g_i(z), \tag{3.25}$$

where $p(m_i)$ will be run over every candidate at every redshift step, and $g_i(z)$ is a step function to tell the estimator in which redshift window the current candidate is. If equipped with more SED information from more observing bands, $g_i(z)$ can be generalized to be a probability function, as shown in the Fig. 2.1 of Chapter 2. Finkelstein et al. (2010) select candidates for their integrated $g_i(z)$ from $6 \leq x \leq 11$ being larger than 60%. They push the detection limit to magnitude ∼29.5, where the photometric error could be large enough to make the results unreliable (Appendix A).

3.5.1 Luminosity Evolution

In the pure luminosity evolution (PLE) scenario, it is assumed that massive galaxies are assembled and formed most of their stars and evolve without merging. Therefore,

$$L_*(z) = L_*(z_0)(\frac{1+z}{1+z_0})^\beta \tag{3.26}$$

$$M_*(z) = M_*(z_0) - 2.5\beta \log \frac{1+z}{1+z_0} \tag{3.27}$$

We also learn from Chapter 2 that $M_*(z) = -20.25 + 0.36\ (z-6)$ fits well at $z = 3-6$. The same evolution holds well at higher redshifts. We find that at $z \sim 7$ $M_* = -19.96 \pm 0.16$, at $z \sim 8$ $M_* = -19.66 \pm 0.17$, assuming $\alpha = -1.80$.

3.5.2 Slope Evolution

For the HUDF field only, α is unlikely to evolve monotonically with redshift since it peaks at $z \sim 6$, drops at $z \sim 7$, and lies in between at z$\sim$5 and 8. As we have pointed out before, cosmic variance plays an important role for pencil beam surveys (Trenti and Stiavelli 2008, Munoz, Trac and Loeb 2010) and we need more data to understand the situation. Grazian et al. (2010) find using simulations that α depends critically on the half light radii of the synthetic galaxies. The size of galaxies evolves roughly as $E^{-1}(z)$ (Appendix B) from redshift z$\sim$1 to z$\sim$5 (Ferguson et al. 2004), but we observe much less change in the slope (Chapter 2).

3.5.3 Density Evolution

In the pure density evolution (PDE) scenario, it is assumed that galaxies emerge and fade at the same rate for any luminosity. As we can see from the study in Chapter 2, the characteristic luminosity changes a lot from $z \sim 3$ to $z \sim 6$, and noticeably from $z \sim 5$ to $z \sim 6$. So it is very unlikely that PDE holds at high redshift. We also expect to see the density ϕ_* drop towards higher redshifts where the first stars are just beginning to form the first galaxies.

3.6 Conclusions

We find the best fit Schechter parameters at $z \sim 7$ LF are: $\alpha = 1.73 \pm 0.15$, at $z \sim 8$ $\alpha = 1.79 \pm 0.14$, assuming $M*$ evolution $M_*(z) = -20.25 + 0.36\ (z - 6)$. Assuming α evolution $\alpha*(z) = -1.80 - 0.05\ (z-6)$, we find $z \sim 7$ $M_* = -19.96 \pm 0.16$, at $z \sim 8$ $M_* = -19.66 \pm 0.17$. In other words, a constant ϕ_*, a slowly steepening α, and a relatively fast dimmed M_* towards higher redshifts can best describe the evolution of the LF from 600 Myr to one Gyr.

Pencil beam surveys in deep fields are suffering from large cosmic variance (Trenti and Stiavelli 2008) so that it is very important to include as many fields as possible. We are including more fields into the calculations, as they are becoming available,

e.g., the BoRG or CANDELS fields.

With the current depth of the near-infrared observations, it is not possible to produce better constraints on the UV slopes, dust content, and SFR (e.g., Vanzella et al. 2011). This issue could be solved with a future investment of HST time, such as the CANDELS project, together with ground based surveys, such as UltraVISTA. However, due to the limited spectral coverage available at wavelength greater than 1.8 μm (i.e., beyond HST/WFC3 H-band) statistical studies of $z \geq 9$ objects will likely be limited until the development of the James Webb Space Telescope.

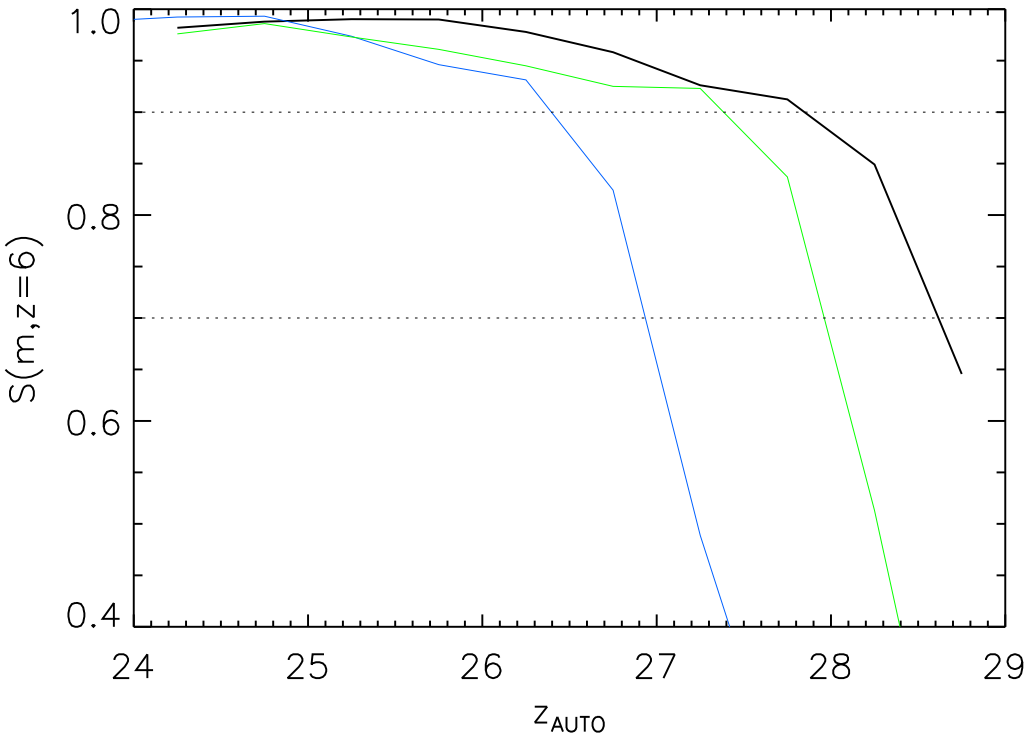

Figure 3.1 Selection function S(m,z). The blue line is from the GOODS, the green one from HUDF NICP12, and the black one from the HUDF. It's clear that the selection function is very close to unity and drops rapidly near the detection limit of the survey. The two horizontal lines show that when shifting the selection function of different fields according to their deepness, the function is universal.

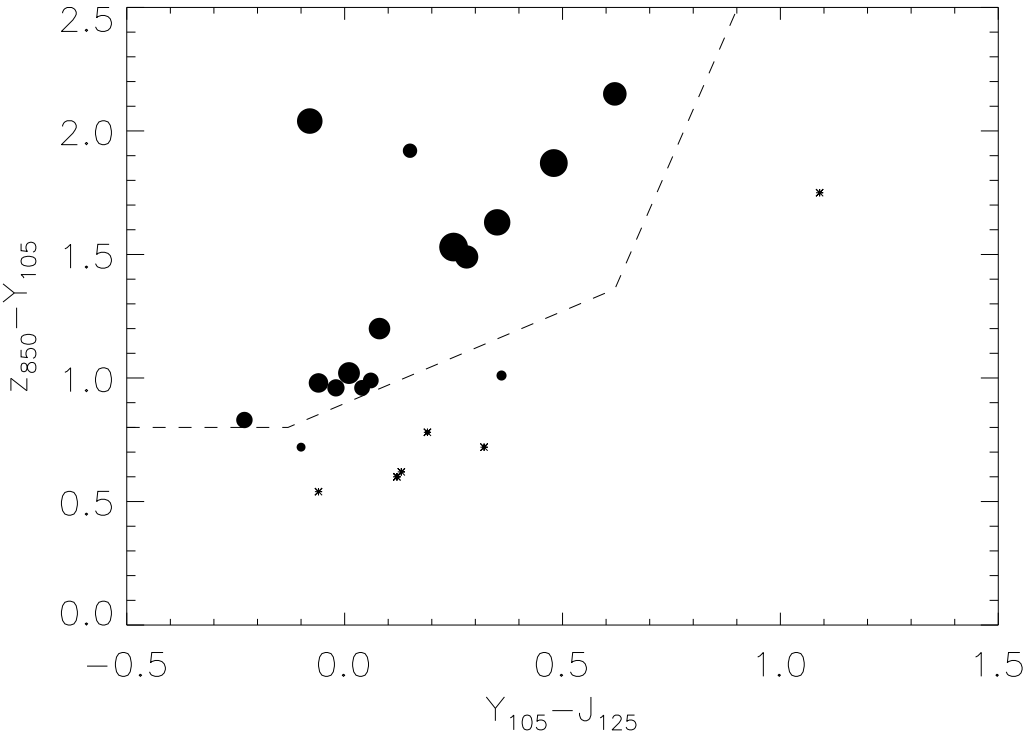

Figure 3.2 Color-color diagram of z_{850}-dropouts in the HUDF field. Candidates are indicated as filled circles whose radius is proportional to the f-factor, and asterisks are those objects with f-factor less than 0.2. See Equation (3.1)-(3.3) for the selection criteria and Table 3.1 for their photometry.

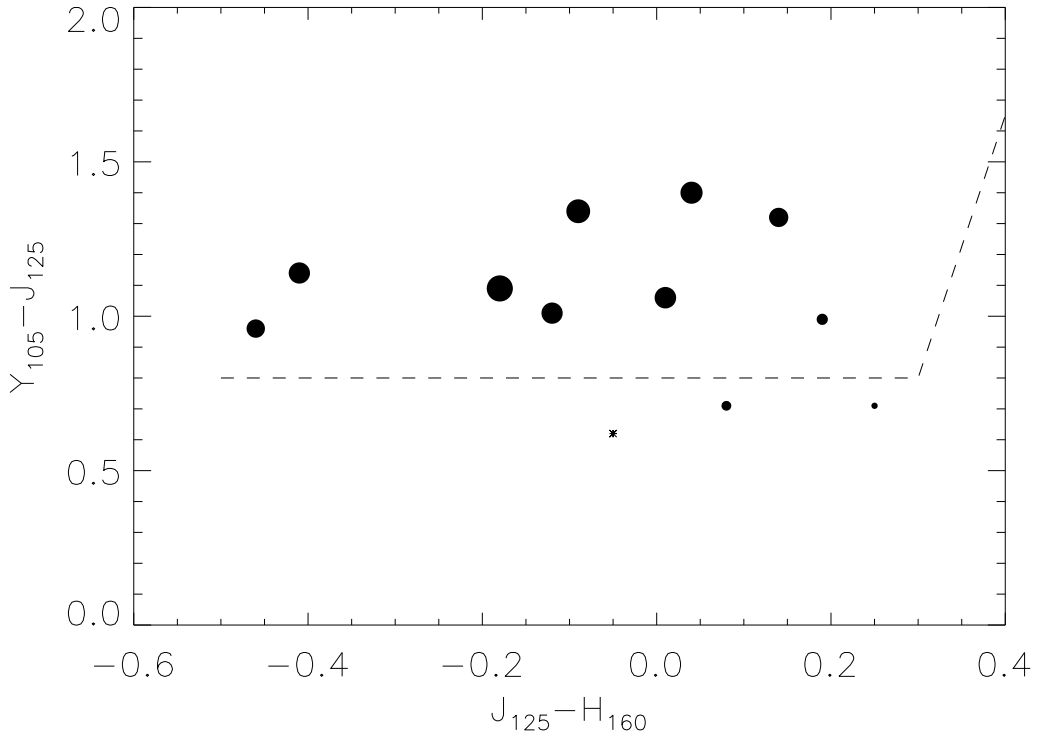

Figure 3.3 Color-color diagram of Y_{105}-dropouts in the HUDF field. Candidates are indicated as filled circles whose radius is proportional to the f-factor, and asterisks are those objects with f-factor less than 0.2. See Equation (3.6)-(3.8) for the selection criteria and Table 3.3 for their photometry.

Table 3.1. Twenty three $z \sim 7$ LBGs in the HUDF

RA	DEC	J_{125}	f-factor	$z_{850} - Y_{105}$	$Y_{105} - J_{125}$
53.17262	-27.76701	27.11	0.01	0.54	-0.06
53.16658	-27.77232	28.02	0.09	0.60	0.12
53.17579	-27.77439	27.69	0.55	0.96	0.04
53.18242	-27.77603	27.77	0.18	0.78	0.19
53.16579	-27.77604	27.99	0.11	0.60	0.12
53.16902	-27.77877	27.99	0.75	1.20	0.08
53.18625	-27.77896	27.10	0.10	1.75	1.09
53.18461	-27.77922	28.03	0.09	0.62	0.13
53.15601	-27.78090	28.15	0.68	0.98	-0.06
53.16890	-27.78131	28.03	0.11	0.72	0.32
53.17733	-27.78238	26.03	1.00	1.53	0.25
53.16491	-27.78234	27.91	0.55	0.99	0.06
53.14553	-27.78372	27.37	0.76	1.02	0.01
53.16544	-27.78433	27.58	0.35	1.01	0.36
53.17332	-27.78458	28.49	0.31	0.72	-0.10
53.16168	-27.78531	27.00	0.97	1.87	0.48
53.17103	-27.78765	27.94	0.81	1.49	0.28
53.15157	-27.78784	28.21	0.60	0.96	-0.02
53.16480	-27.78819	27.05	0.82	2.15	0.62
53.17735	-27.79206	27.10	0.92	1.63	0.35
53.15192	-27.79234	28.23	0.89	2.04	-0.08
53.15322	-27.79822	27.91	0.57	0.83	-0.23
53.15503	-27.80170	28.26	0.50	1.92	0.15

[a]See Fig. 3.2 for the graph.

Table 3.2. Studies of the $z \sim 7$ Luminosity Function

References	α	M_*	ϕ_* [10^{-3} Mpc^{-3} mag^{-1}]
Bouwens +2010b	-2.01±0.21	-20.14±0.26	$0.86^{+0.70}_{-0.39}$
Grazian +2010	-1.7±0.5	-20.1±0.4	0.7±0.5
McLure +2010	-1.72	-20.11	0.7
Oesch +2010	-1.77±0.20	-19.91±0.09	1.4(fixed)
Wilkins +2010	-1.7 fixed	-19.9	1.1

Table 3.3. Twelve $z \sim 8$ LBGs in the HUDF

RA	DEC	J_{125}	f-factor	$Y_{105} - J_{125}$	$J_{125} - H_{160}$
53.15889	-27.76499	28.37	0.67	1.32	0.14
53.15748	-27.76669	28.47	0.77	1.40	0.04
53.15680	-27.76708	28.22	0.83	1.34	-0.09
53.15496	-27.77454	28.52	0.64	0.96	-0.46
53.17972	-27.77457	27.77	0.34	0.71	0.08
53.17865	-27.77625	27.84	0.75	1.06	0.01
53.18625	-27.77896	27.10	0.91	1.09	-0.18
53.14174	-27.78067	28.48	0.74	1.14	-0.41
53.17830	-27.78212	28.88	0.22	0.71	0.25
53.14016	-27.78302	28.81	0.39	0.99	0.19
53.16480	-27.78819	27.05	0.08	0.62	-0.05
53.15323	-27.79099	28.02	0.74	1.01	-0.12

[a]See Fig. 3.3 for the graph.

Table 3.4. Studies of the $z \sim 8$ Luminosity Function

References	α	M_*	ϕ_* [10^{-3} Mpc^{-3} mag^{-1}]
Bouwens +2010a	-1.74 fixed	-19.5±0.3	1.1
Bouwens +2010b	-1.91±0.32	-20.10±0.52	$0.59^{+1.91}_{-0.32}$
Lorenzoni +2011	-1.70 fixed	-19.5	0.93
Yan +2010	-1.80	-17.80	0.76

Chapter 4

HIGH-REDSHIFT QUASARS IN THE DEEP FIELDS

In this chapter, we report on our search for high-redshift quasars in the GOODS and the HUDF fields to probe the faint end of quasar luminosity function (QLF). Ten candidates at $z \sim 6$ have been identified in the four deep fields. By combining our results with those from the SDSS and the CFHQS, we find that a single-power-law extending to $M_{1450} \approx -19$ has a slope $\beta = -2.8$. However, a double-power-low distribution is preferred. We also predict the quasar number density at $z \sim$7 and 10 for future searches.

4.1 Introduction

Quasars (QSOs) are powered by accretion onto supermassive black holes (BHs). The successful searches for redshift $z \sim 6$ quasars such as the Sloan Digital Sky Survey main fields (SDSS-main, Fan et al. 2001, 2003, 2004, 2006b) & deep stripes (SDSS-deep, Jiang et al. 2008, 2009), and the Canada France High-z Quasar Survey (CFHQS, Willott et al. 2007, 2009, 2010) have found almost 50 of them with spectroscopical confirmations. Other groups (Mahabal et al. 2005; Cool et al. 2006; Goto 2006; McGreer et al. 2006; Venemans et al. 2007; Momjian et al. 2008; Mortlock et al. 2009,

2011b; Zeimann et al. 2011) also discover z≥5.7 quasars and have reached the redshift record of z=7.1 (Mortlock et al. 2011b). See Table 4.1 for a complete list.

A better knowledge of the high-redshift quasar luminosity function (QLF) is essential to understand their formation and early evolution. It would allow us to better assess quasars' contribution to the reionization of hydrogen. Consensus has gathered that quasars are unable to keep the universe ionized at $z \sim 6$ (e.g., Willott et al. 2010) but they could still remain an important contributor. An accurate description of the QLF would also map the BH accretion history and determine how the feedback from quasars inverts the dark matter halo hierarchical sequence for the collapse of baryonic matter (e.g. Volonteri & Rees 2006, Granato et al. 2004).

During the past two decades, we have learned a lot about the QLF at low-redshift and its bright-end at high-redshift. We know from the 2dF QSO Redshift Survey (2QZ, Croom et al. 2004) that at $0.4 < z < 2.1$, the QLF is well fit by a double power law with pure luminosity evolution, in the sense that the characteristic luminosity of quasars decreases at lower redshift. The density of luminous quasars ($M_{1450} < -26$) is a strong function of redshift: it peaks at z ∼2-3 and declines exponentially with redshift towards earlier and later time (SDSS, Fan et al. 2006b). The co-moving density of luminous quasars at $z \sim 6$ is about 40 times smaller than that at z ∼3. Do fainter quasars evolve differently at high-redshift?

Unfortunately, the wide survey fields mentioned above do not go deep enough to determine the knee of the QLF. For example, SDSS-main goes down to apparent magnitude $z_{AB} = 20.5$, and SDSS-deep to $z_{AB} = 22.2$, while CFHQS $z_{AB} \sim 22.7$ with one single faint quasar at $z_{AB} = 24.4$. Jiang et al. (2009) divide all SDSS $z \sim 6$ quasars into five magnitude bins and find the bright end slope $\beta = -2.6 \pm 0.3$, flatter than that at z ∼2 but steeper than that at z ∼4 derived from SDSS data (Richards et al. 2006b; Hopkins et al. 2007). Willott et al. (2010) combine all the SDSS and CFHQS $z \sim 6$ quasars to determine $\beta = -2.81$. But the break magnitude M_* or faint end slope α have not been constrained well.

Ultra deep fields observed by the Hubble Space Telescope (HST) are actually available to discover those really faint QSOs. We would therefore like to extend the

study 3-mag deeper than the SDSS-deep in the Great Observatories Origins Deep Survey (GOODS, Giavalisco et al. 2004) and 3-mag deeper than the CFHQS in the Hubble Ultra Deep Field (HUDF, Beckwith et al. 2006) & its parallel UDF05 (PI: Stiavelli, Oesch et al. 2007), which will greatly shape the $z \sim 6$ QLF at the faint end.

4.2 $z \sim 6$ Candidates

4.2.1 Selection

We work on four *HST*/ACS (Ford et al. 2003) deep fields in four broadbands: F435W (B_{435}), F606W (V_{606}), F775 (i_{775}), and F850LP (z_{850}). We use the most recent and updated version of the data, namely: the GOODS (south: GOODS-S & north: GOODS-N) v2.0 data by Giavalisco & the GOODS Team (2008), the HUDF data from Beckwith et al. (2006), the HUDF NICP12 from Oesch et al. (2007).

We adopt the i_{775}-dropout selection criteria from Beckwith et al. (2006), i.e.,

$$i_{775} - z_{850} > 1.3, \tag{4.1}$$

$$S/N(V_{606}) < 2 \quad \text{or} \quad V_{606} - z_{850} > 2.8. \tag{4.2}$$

Besides, $S/N(z_{850}) > 5$ is demanded for each candidate to largely avoid interlopers and stellarity CLASS_STAR (S/G) > 0.85 to select point-like sources at the resolution of 0.03 arcsec/pixel. We also ask for $z_{AB} < 25.5$ for the GOODS data and $z_{AB} < 27.5$ for the HUDF data to minimize contaminations, and ensure that stellarity is well measured.. Since we are only interested in relatively bright sources in our fields, the stellarity S/G parameter determined by SExtractor (Bertin & Arnouts 1996) is valid (cf., Fig 1.2). We do not apply the f-factor technique introduced in Chapter 2 because the requirement of stellarity and brightness allows us to select highly-qualified candidates for possible spectroscopical observation.

We proceed to rule out those candidates that are close to the locus of stars in the $i_{775} - z_{850}$ vs $z_{850} - J$ plane. Here the J-magnitudes are generally from GOODS-MUSIC catalog (Grazian et al. 2006) but we also consider the public GOODS-ISAAC

catalog (Retzlaff et al. 2007) and the GOODS-SIMPLE catalog (Damen et al. 2011) when available. Essential stars with red $i_{775} - z_{850}$ colors have also red $z_{850} - J$ colors. For those objects with blue $z_{850} - J$ color or no measured J-band flux we measure their proper motion with errors of about 6−10 mas/yr. Retrieving (through StarView[1] from the Multimission Archive at STScI, or MAST[2]) and combining (through MultiDrizzle, Koekemoer et al. 2006) ACS images available for more than four-year baseline, we are able to exclude those moving with 2-σ significance or higher. Objects in the GOODS-S identified as stars in the GOODS VLT/FORS2 spectroscopy survey (Vanzella et al. 2008) or VLT/VIMOS spectroscopy survey (Popesso et al. 2008) have also been removed. The remaining objects constitute our $z_{850} \leq 25.5$ $z \sim 6$ QSOs sample which comprises of 4 candidates in each of GOODS South and North field (Table 4.3). A similar process has been carried out on the HUDF field with GRAPES (Pirzkal et al. 2004) spectroscopic data helping eliminate brown dwarf contaminants and leaving us no candidate with $z_{850} \leq 27.5$. Finally we study the HUDF NICP12 field where two candidates are included to the final list.

Cristiani et al. (2004) and Fontanot et al. (2007) find altogether twelve $2.7 < z < 5.2$ QSOs in the GOODS fields. Our survey in the GOODS is one magnitude fainter and one redshift deeper than theirs, which gives the number of QSOs expected of about 7.4 by using slope-flat, close to the candidate number 8 we have now.

4.2.2 Power-Law Fits

The QLF can be fit to a single power law as

$$\phi \;=\; \phi^* \times 10^{-0.4(\beta+1)(M_{1450}+26)} \tag{4.3}$$

and the best fits at $z \sim 6$ from the SDSS-deep (Jiang et al. 2008) are $\phi^* = (5.2 \pm 1.9) \times 10^{-9}[Mpc^{-3}mag^{-1}]$ and $\beta = -3.1 \pm 0.4$, which is consistent with the slope $\beta = -3.2 \pm 0.7$ derived from the SDSS-main (Fan et al. 2004).

[1]http://starview.stsci.edu/
[2]http://archive.stsci.edu/

To estimate how many QSOs are expected in our deep fields based on previous studies in the wide fields, we apply the results from SDSS-deep to the cumulative QLF $\psi \equiv \int \phi \, dM$, which gives what we call the "slope-fit",

$$(\log \psi)_{fit} \;\; = \;\; 13.27 + 0.84M \tag{4.4}$$

where M in the Eqn (4.4) is the detection limit of the survey. If the error is decided by the Cauchy-Schwartz inequality,

$$\delta \log \psi \;\; \geq \;\; \mathrm{ABS}(|\frac{\partial \log \psi}{\partial \phi^*}|\delta\phi^* - |\frac{\partial \log \psi}{\partial \beta}|\delta\beta), \tag{4.5}$$

we have the 1-σ flatter one as the "slope-flat",

$$(\log \psi)_{flat} \;\; = \;\; 9.58 + 0.69M \tag{4.6}$$

Extrapolating the QLF down to the brightness limit we are working with the GOODS and the HUDF, we predict the number of the QSOs in each field (Table 4.4). The uncertainties are given by cosmic variance distributions for pencil-beam surveys (Trenti & Stiavelli 2008). It is clear that the slope-flat cumulative QLF agree with our results better than the slope-fit. We leave detailed discussion to the next sub-section.

Drawing a single-power fit with the SDSS (main and deep) points, we find that

$$\beta = -2.8 \pm 0.1 \tag{4.7}$$

which is consistent with -3.2 ± 0.7 by the SDSS-main and -3.1 ± 0.4 by the SDSS-deep. Since the completeness at this bright magnitude is close to one (Chapter 2), this is the upper limit of the slope by assuming our candidates are all true QSOs. The real one should be flatter if any of our candidates are interlopers. Our derivation of the $z \sim 6$ QLF can be found in Fig. 4.1.

4.2.3 Compatibility with SDSS

To avoid possibly misleading a posteriori probabilities, we use three different methods with a priori probability to judge whether our results are compatible with the SDSS slopes extended to the faint end.

For the slope-fit, the probability of two being at 1-σ away and two being at 2-σ away out of four independent tests, as in our case, will be roughly less than $C_4^2 \times (32\%)^2 \times (5\%)^2 = 0.0015$, which is quite small compared to that of all within 1-σ, $(68\%)^4 = 0.2138$. For slope-flat, the probability of three within 1-σ and one out of 1-σ, as in our case, will be roughly $C_4^1 \times (68\%)^3 \times (32\%) = 0.4025$. It is clear that the slope-fit is strongly disfavored by our surveys and the slope-flat is quite promising.

The same conclusion could be drawn from χ^2 tests, $\chi^2 \equiv \Sigma \frac{(obs-exp)^2}{exp}$,

$$\chi^2_{fit} = \frac{(26-0)^2+(26-2)^2}{26} + \frac{(8-4)^2+(8-4)^2}{8} \approx 52 \quad (4.8)$$

$$\chi^2_{flat} = \frac{(4-0)^2+(4-2)^2}{4} + \frac{(3-4)^2+(3-4)^2}{3} \approx 6 \quad (4.9)$$

The third method is to check for compatibility between our survey and the SDSS. Since we have an upper limit for the possible numbers of faint QSOs, the probability for each survey that our estimate is incompatible with the SDSS data at the bright end will be

$$P = \sum_{n+1}^{\infty} p(k)$$

where $p(k)$ is the probability distribution at number k and n is the upper limit. The Poisson distribution $p(k) = \lambda^k e^{-\lambda}/k!$, where λ is the intrinsic number, usually has a sharper bump than the distribution with cosmic covariance (e.g. Fig. 1 of Trenti & Stiavelli 2008) but remains a good approximation when λ is not very large. For the slope-fit, P= $100\% \times 100\% \times 90\% = 90\%$, i.e., there is 90% chance our results are not compatible with the simple fit of SDSS data. While for the slope-flat, $P = 98.2\% \times 76.2\% \times 18.5\% = 13.8\%$, which is again favored.

Therefore, if the QLF at $z \sim 6$ is fitted by a single power-law, the slope-flat will be the answer based on our deep fields and SDSS wide fields. Later study by Willott et al. (2010) confirms this conclusion.

4.3 Estimation for other Redshifts

The new *HST* WFC3/IR camera allows ambitious near-infrared surveys, e.g., HUDF09 (PI: G. Illingworth, Oesch et al. 2010; Bouwens et al. 2010a) and CANDELS (PI: S. Faber & H. Ferguson, Grogin et al. 2011), to detect $z > 6$ quasars. We are among the first groups to consider seriously the $z > 5.5$ quasars in the deep fields.

4.3.1 Quasars at $z \sim 7$

Mortlock et al. (2011b) recently find a quasar at redshift of 7.085, with a BH of two billion solar mass. Such a massive quasar at just 770 million years after the Big Bang is significant to provide information on the state of the surrounding Universe. Its spectrum shows tantalizing differences from $z \sim 6$ quasars, suggesting a high neutral-hydrogen fraction (>0.1) in the IGM close to the quasar. But one object does not always tell the whole story, so it will be important to find more quasars at redshifts above 6.

Now, we employ three evolution models to estimate the minimum absolute magnitude M needed to detect 10 QSOs at z ∼7 in a 0.25 deg^2 survey. The slope-flat $(\log\psi)_{flat} = 9.58 + 0.69M$ at $z \sim 6$ is adopted.

1. Study of quasars up to z ∼5 from Richards et al. (2006b) suggests that the cumulative QLF, $\psi \approx 10^{-0.5z}$. The number of QSOs drops to 10% for every two increasing redshift >3. Therefore, we have

$$0.69(M - M_6) = 0.5(z - 6) + \log(V_6/V), \tag{4.10}$$

where V_6 is the comoving volume at $z \sim 6$ by a survey as deep as M_6 to detect 10 QSOs, V is the comoving volume of field of view 0.25 deg^2, and the variables without suffix are at redshift we are studying, i.e., $z = 7$. We find that $M_{1450} = -20.91$, which encourages that a future 0.25 deg^2 survey as deep as the GOODS survey would have great chance to find ten $z \sim 7$ QSOs. Thus, the QLF can be well determined.

2. Eddington accretion leads to $L \propto \exp(\frac{t-t_0}{\tau})$, where the Salpeter time $\tau = 4.5 \times 10^8 \times \frac{\epsilon}{1-\epsilon}$ yr and choosing the radiative efficiency $\epsilon = 0.1$ gives us $\tau = 50$

Myr. The luminosity and mass of a quasar will more than double in 50 Myr at the Eddington accretion limit if the supply of nearby gas and dust is sufficient. Therefore, we have

$$0.69(M - M_6) = (2.5 \log e)\frac{t_6 - t}{\tau} + \log(V_6/V) \tag{4.11}$$

to find $M_{1450} = -17.72$. This is roughly as deep as the HUDF field and it is unrealistic in the near future to carry on such a survey.

3. Linear accretion $L \propto t - t_0$, where t is the cosmic time since the big bang. t_0 could be conveniently chosen as that of z=30 so that

$$0.69(M - M_6) = 2.5 \log \frac{t_6 - t_{30}}{t - t_{30}} + \log(V_6/V) \tag{4.12}$$

In this case, $M_{1450} = -21.38$, which means it is possible for the SDSS to fulfill the task.

The results are quite different. Model 1 (extrapolation) comes from previous observations of lower redshifts so it would be expected to well match the real data. It would also be possible for something peculiar to happen when the time is close to the end of reionization, since the physical environment becomes different, more or less neutral instead of mostly ionized. Model 2 (Eddington) gives us an upper limit of accretion efficiency so that the resulted M will be fainter than the real one. Model 3 makes a reasonable assumption and can be improved when the start of reionization can be better estimated.

4.3.2 Quasars at $z \sim 10$

We are approaching redshift 10 using the newly installed HST/WFC3 (Bouwens et al. 2011a), so that it is useful to look into how many quasars there are at that early epoch of the universe. Assuming quasars SEDs are power-law, $f_\nu \propto \nu^\alpha$,

$$m_{AB}(\lambda_1) = m_{AB}(\lambda_2) + 2.5\alpha \log(\lambda_1/\lambda_2) \tag{4.13}$$

where $\alpha = -0.79$ from (Fan et al. 2001) (it could be flatter based on other groups' estimations, e.g., Barger et al. 2005). The quasar's Lyα lines will be redshifted to

about 1.3 μm at z=10 so $M^J_{1450} = -23.81$. Adopting the extrapolation (Richards et al. 2006b) as in Section 4.3.1, we estimate that about one quasar can be found at the detection limit of apparent magnitude $m = 24$ for every 110 deg^2 of survey.

4.4 Spectroscopical Confirmations

4.4.1 J033216.55-274103.2

Fiore et al. (2011) find it (their 216554) just below detection threshold [3] and propose that it lies at $z > 6$. We have selected (in Chapter 2) it an i_{775}-dropout in the GOODS-S field with $i_{ISO} = 27.64 \pm 0.21$, $z_{ISO} = 26.53 \pm 0.09$ and therefore its f-factor=0.20, which means there is 20% chance it is a real high-z object. SExtractor can not decide its stellarity and assigns as S/G=0.

4.4.2 J033219.05-274429.8

Fiore et al. (2011) find it (their E1611) just below detection threshold [4] and propose that it lies at z=6.9 (68% in 6.0-7.4). We have not selected it as an i_{775}-dropout with $i_{ISO} = 27.88 \pm 0.17$, $z_{ISO} = 27.39 \pm 0.13$. It is also detected in the V-band, 28.47 ± 0.18, which further excludes its high-z nature. Its S/G=0.3, but the parameter may fail at such faint magnitudes (Fig. 1.2).

4.4.3 J033229.29-275619.5

Similar to the description in Section 4.2.1, we have searched to find $z \sim 5$ quasar candidates as point-like V_{606}-band dropouts in the GOODS-S. Unlike the null result at $z \sim 6$, we find one object, i.e. J033229.29-275619.5, has also been detected by the 4 Ms *Chandra* Deep Field South X-ray imaging. Recognized as a quasar at z=4.76 based on FORS-2 spectroscopy (Vanzella et al. 2006), it now turns out to be

[3] 2 spurious detection in 5000 candidates in the X-ray image.
[4] 4 spurious detection in 5000 candidates in the X-ray image.

Compton-thick, and probably the highest-redshift type-II quasar ever found (Chapter 5).

4.4.4 J033238.80-274953.7

It satisfies our i_{775}-dropout criteria to be a $z \sim 6$ candidate. Mannucci et al. (2007) even find it to be a possible $z \sim$7 galaxy with the information from HST/NICMOS. However, many groups have speculated it is a Galactic star (Stanway et al. 2003; Bunker et al. 2004) and now finally confirm it (Vanzella et al. 2009). We measure it in four-year HST imaging to find its proper motion of 3.5 mas/yr. This justifies our removing other high-proper-motion objects from the $z \sim 6$ quasar candidates list.

4.4.5 Our spectroscopic follow-ups

We applied for VLT observing time (Circle 81) for the spectra of three out of four of our $z \sim 6$ QSO candidates in the GOODS-S, which are lying within a single FORS2 field. Low spectral resolution is acceptable since QSOs are characterized by broad lines. We find that GRIS_150I+27 is the optimal choice and will provide us with spectra with 6.9 A / pixel of spectral resolution, a wavelength range from 6000A to 11000A and a useful field of view (for complete spectral coverage) of ∼5.5' × 6.8'. Our goal is to obtain spectra with S/N of at least 4 per resolution element. We will use the MXU mode and we plan to fill two slits with bright objects for mask alignment and other slits with two candidate QSOs at $z = 5$ identified with the same method applied to V-dropouts and other $z \geq 5$ galaxy candidates not previously observed in GOODS.

We were granted four half-night observation time on Keck Telescope in Hawaii in 2009. But the spectra are inconclusive in assessing whether the candidates in the GOODS-South are true quasars or not. The same story happened again in Spring 2011. As listed in Table 4.3, our objects are all brighter than 24.5 so that they are very promising to be detected by spectroscopy.

4.5 Discussion

Luminosity-dependent evolution of the space density of soft X-ray selected bright AGNs (Hasinger et al. 2005) and optically selected faint QSOs (e.g., Wolf et al. 2003 and Richards et al. 2006) both peak around z ∼2. And the data are well fitted by double-power law (e.g., Fontanot et al. 2007) or the exponential $L^{1/4}$ law (Pei 1995) to z ∼5. But the lack of faint QSOs detected at $z \sim 6$ leaves us great uncertainty on the QLF. Shankar and Mathur (2007) argue using some incomplete surveys that there is flatting at $M_{1450} > -24.67$. Fewer or no detection of QSOs in any of our fields would significantly bend the QLF down at the faint end to adopt a double-power-law form.

SDSS-main QSOs have central BHs with masses about a few 10^9 $M_\odot$ (Kurk et al. 2007), and our candidates are expected to harbor BHs with masses of order 10^7 $M_\odot$ or less. Trenti & Stiavelli (2008) derived a QLF assuming that it is the product of accretion from seed BHs formed by first stars.The accretion rate is limited by the total amount of gas available within the host dark halo, leading naturally to a BH-galaxy mass correlation and to a QLF in agreement at high luminosities with the SDSS one but predicting steeper slopes at fainter magnitudes. Volonteri & Rees (2006) studied the growth of supermassive BHs considering also a number of dynamical effects including in particular BH mergers. They also predict QLF that could be as steep or slightly steeper than the one observed at the bright end. Begelman, Volonteri & Rees (2006) have considered an entirely different scenario where massive seed BH could form directly out of gaseous collapse at high redshift and then possibly grew super-Eddington up to 10^{4-6}M$_\odot$. This model is favored by the z=7.1 quasar recently discovered by Mortlock et al. (2011b). Such seed BHs could grow at a more leisurely rate and it is harder to make a firm prediction on the $z \sim 6$ QLF that one would obtain. Beaming of jets also brings complexity to the study. If beaming is considered when estimating the quasar luminosity, there will be fewer bright quasars. In the meantime, there will be more quasars undetected if they are not beaming toward us. These two effects may not change the total contribution of quasars to the reionization,

but affect the shape of QLF. Thus, measuring the QLF slope at fainter magnitudes than achievable by the SDSS and the CFHQS would give us direct insight on the possible formation mechanisms of the $z > 3$ QSOs.

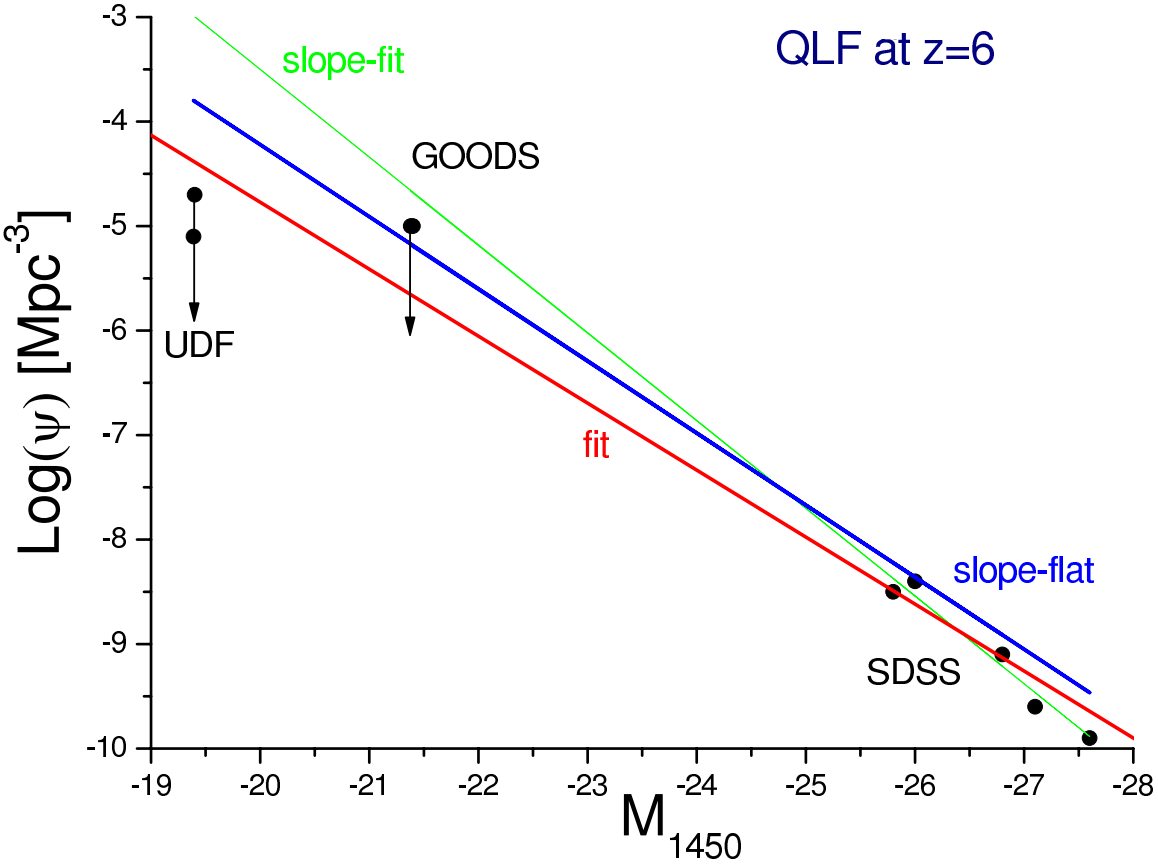

Figure 4.1 QLF at $z \sim 6$. The slope-fit (green line) is from Jiang et al. (2008) and the slope-flat (blue line) is 1σ flatter. The red line is fitted for all SDSS points and our candidates, assuming they are all real which are actually the upper limit.

Table 4.1. Most Updated Quasars z≥5.7

QSOs	redshift	reference
J104433.04-012502.2	5.80	(1) Fan et al. (2000)
J083643.85+005453.3	5.82	(2) Fan et al. (2001)
J130608.26+035626.3	5.99	(2)
J103027.10+052455.0	6.28	(2)
J114816.64+525150.3	6.42	(3) Fan et al. (2003)
J104845.05+463718.3	6.23	(3)
J163033.90+401209.6	6.05	(3)
J141111.29+121737.4	5.93	(4) Fan et al. (2004)
J160254.18+422822.9	6.07	(4)
J162331.81+311200.5	6.22	(4)
J000552.34-000655.8	5.85	(4)
J000239.39+255034.8	5.80	(4)
J114816.2+525339	5.70	(5) Mahabal et al. (2005)
J081827.40+172251.8	6.00	(6) Fan et al. (2006)
J084035.09+562419.9	5.85	(6)
J092721.82+200123.7	5.79	(6)
J113717.73+354956.9	6.01	(6)
J125051.93+313021.9	6.13	(6)
J133550.81+353315.8	5.93	(6)
J143611.74+500706.9	5.83	(6)
J084119.52+290504.4	5.96	(7) Goto et al. (2006)
J142516.3+325409	5.85	(8) Cool et al. (2006)
J1427385+331241	6.12	(9) McGreer et al. (2006)

Table 4.1 (cont'd)

QSOs	redshift	reference
J003311-012524	6.13	(10) Willott et al. (2007)
J150941-174926	6.12	(10)
J164121+375520	6.04	(10)
J232908-030158	6.43	(10)
J030331.40-001912.9	6.07	(11) Jiang et al. (2008)
J035349.72+010404.4	6.05	(11)
J205406.49-000514.8	6.06	(11)
J231546.57-002358.1	6.12	(11)
J020332.39+001229.3	5.85	(11) & (12) Venemans et al. (2007)
J1427+3312	6.12	(13) Momjian et al. (2008)
J005502+014618	6.02	(14) Willott et al. (2009)
J010250-021809	5.95	(14)
J021627-045534	6.01	(14)
J022743-060530	6.20	(14)
J231802-024634	6.05	(14)
J232914-040324	5.90	(14)
J012958.51-003539.7	5.78	(15) Jiang et al. (2009)
J023930.24-004505.4	5.82	(15)
J205321.77+004706.8	5.92	(15)
J214755.41+010755.3	5.81	(15)
J230735.35+003149.4	5.87	(15)
J235651.58+002333.3	6.00	(15)
J131911.29+095051.4	6.13	(16) Mortlock et al. (2009)

Table 4.1 (cont'd)

QSOs	redshift	reference
J005006+344522	6.25	(17) Willott et al. (2010)
J013603+022605	6.21	(17)
J142952+544717	6.21	(17)
J022122-080251	6.16	(17)
J222901+145709	6.15	(17)
J210054-171522	6.09	(17)
J031649-134032	5.99	(17)
J105928-090620	5.92	(17)
J224237+033421	5.88	(17)
J222843.54+011032.2	5.95	(18) Zeimann et al. (2011)
J1120+0641	7.1	(19) Mortlock et al. (2011)

Table 4.2. Most Updated Quasars at z>3 in Our Deep Fields

QSOs	redshift	reference
J033204.94-274431.7	3.46	Cristiani et al. (2000)
J033218.83-275135.4	3.66	Szokoly et al. (2004)
J033229.29-275619.5	4.76	Gilli et al. (2011)
J033229.85-275105.9	3.70	Norman et al. (2002)
J033239.66-274850.6	3.06	Szokoly et al. (2004)
J033242.84-274702.5	3.19	Szokoly et al. (2004)
J123629.44+621513.2	3.65	Cowie et al. (2004)
J123643.09+621108.8	3.23	Cowie et al. (2004)
J123647.96+620941.6	5.19	Barger et al. (2002)
J123703.98+621157.8	3.41	Barger et al. (2003)
J123723.71+622113.3	3.52	Cowie et al. (2004)

Table 4.3. Four $z \sim 6$ QSO Candidates in the GOODS-South Field

ID	z_{850}	J[a]	$i_{775} - z_{850}$	z_{850}-J
J033204.69-274959.1	24.09	25.11	1.47	-1.02
J033205.72-274959.8	24.36	24.97	1.33	-0.61
J033222.47-275047.4	24.42	23.12	1.74	1.30
J033229.59-275228.7	23.18	22.07[b]	1.52	1.11

[a]From the GOODS-MUSIC catalog (Grazian et al, 2006).

[b]24.76 in the GOODS-SIMPLE catalog (Damen et al. 2011).

Table 4.4. Expected $z \sim 6$ QSO Numbers in Our Deep Fields

numbers	GOODS[a]	HUDF[b]
N_{fit}[c]	8 ± 4	26 ± 10
N_{flat}[d]	3 ± 2	4 ± 3

[a]as deep as magnitude 25.5.

[b]as deep as magnitude 27.5.

[c]expected by the slope-fit.

[d]expected by the slope-flat.

Chapter 5

A COMPTON-THICK QUASAR AT $z \sim 5$

We report the discovery of a Compton-thick Active Galactic Nucleus (AGN) at $z = 4.76$ in the 4 Ms *Chandra* Deep Field South. This object was selected as a V-band dropout in HST/ACS images and previously recognized as an AGN from optical spectroscopy. The 4 Ms *Chandra* observations show a significant ($\sim 4.2\sigma$) X-ray detection at the V-band dropout position. The X-ray source displays a hardness ratio of HR=0.23 ± 0.24, which, for a source at $z \sim 5$, is highly suggestive of Compton-thick absorption. The source X-ray spectrum is seen above the background level in the energy range of $\sim 0.9 - 4$ keV, i.e., in the rest-frame energy range of $\sim 5 - 23$ keV. When fixing the photon index to $\Gamma = 1.8$, the measured column density is $N_H = 1.4^{+0.9}_{-0.5} \times 10^{24}$ cm^{-2}, which is Compton-thick. To our knowledge, this is the most distant heavily obscured AGN, confirmed by X-ray spectral analysis, discovered so far. The intrinsic (de-absorbed), rest-frame luminosity in the 2-10 keV band is $\sim 2.5 \times 10^{44}$ erg s^{-1}, which places this object among type-2 quasars. The Spectral Energy Distribution shows that massive star formation is associated with obscured black hole accretion. This system may have then been caught during a major co-eval episode of black hole and stellar mass assembly at early times. The measure of the number density of heavily obscured AGN at high redshifts will be crucial to

reconstruct the BH/galaxy evolution history from the beginning. A version of this Chapter has been included in Gilli, Su, Norman, Stiavelli et al. (2011).

5.1 Introduction

While optically bright quasars are the most spectacular expression of accretion onto supermassive black holes (SMBHs) at galaxy centers, it is widely believed that SMBHs grow most of their mass during obscured phases, in which the detection of the nuclear power becomes challenging (e.g., Fabian 1999). Large amounts of gas and dust are found to hide the majority of Active Galactic Nuclei (AGN) in the nearby and distant Universe, as demonstrated by deep and wide X-ray surveys over different sky fields (see e.g., Brandt & Hasinger 2005 for a review). From ∼30 to ∼50% of all AGN are believed to be obscured by extreme gas column densities above $N_H = \sigma_T^{-1} \sim 10^{24}\mathrm{cm}^{-2}$. These objects are dubbed "Compton-thick" and represent the most elusive members of the AGN population. The evidence for an abundant population of local Compton-thick objects is compelling: up to $\sim$ 50% of nearby Seyfert 2s contain a Compton-thick nucleus (Risaliti et al. 1999; Akylas & Georgantopoulos 2009); about 50 objects - mostly local - have been certified as "bona-fide" Compton-thick AGN by X-ray spectral analysis (Comastri 2004).

Synthesis models of the X-ray background (XRB) suggest that Compton-thick AGN must be abundant at least up to $z \sim 1$ to explain the peak of the XRB at 30 keV (see e.g., Gilli et al. 2007; Treister et al. 2009, and references therein). A population of distant, Compton-thick AGN, as abundant as that predicted by XRB synthesis models, is also required to match the SMBH mass function measured in nearby galaxies with that of "relic" SMBHs grown by accretion (e.g., Marconi et al. 2004). In recent years it has been proposed that Compton-thick AGN represent a key phase of the BH/galaxy coevolution, during which the BH is putting most of its feedback into the host galaxy (e.g., Daddi et al. 2007; Menci et al. 2008), and it has also been suggested that their number density steeply increases with redshift (Treister et al. 2009).

The observation of heavily obscured AGN at high-z, $z \geq 2-3$, remains challenging and it is very difficult to estimate their abundance since they produce only a small fraction of the XRB emission and are thus poorly constrained by synthesis models. Deep X-ray surveys have proven effective in revealing a few "bona fide" Compton-thick AGN at high-z. For instance, four such objects at $1.53 < z < 3.70$ have been discovered in the *Chandra/XMM* - Deep field South (CDFS; see Norman et al. 2002; Comastri et al. 2011; Feruglio et al. 2011). Other examples of candidate Compton-thick AGN at high-z have been reported (e.g., Tozzi et al. 2006; Polletta et al. 2008), even up to z=5.8 (Brandt et al. 2001), albeit with poorer X-ray photon statistics. Selection techniques based on the strength of the mid-IR emission with respect to the optical and X-ray emission have also been developed and applied to select large populations of candidate Compton-thick AGN up to $z = 2 - 3$ (Daddi et al. 2007; Alexander et al. 2008a; Fiore et al. 2009; Bauer et al. 2010). Once more, however, the lack of X-ray spectra prevents an unambiguous determination of the absorbing column density, making the measurements by these works largely uncertain.

In this Chapter, we report the discovery of a "bona-fide" Compton-thick AGN at z=4.76 in the 4 Ms CDFS.

5.2 Source selection and Observations

We searched for $V-$band dropout objects in the HST/ACS v2.0 data of GOODS-South (Giavalisco et al. 2004) associated with X-ray emission in the 4 Ms *Chandra* image. We used the V_{606}-dropout selection criteria from Oesch et al. (2007), which effectively pick sources at $4.7 < z < 5.7$[1]. Details on the production of the V-dropout catalog are given in Su et al. (2011). Additionally, we required a stellarity parameter (CLASS_STAR) greater than 0.9 in the z_{850} band to choose point-like sources. This led to 21 star-like V_{606}-dropouts with $z_{850} < 25.5$, among which there are four z$\sim$5 galaxies, eleven stars, three lower-redshift galaxies, and one z$\sim$5 AGN, which is the

[1] An object is defined as a V_{606}-dropout if $V_{606} - i_{775} > min[1.5 + 0.9(i_{775} - z_{850}), 2]$, $V_{606} - i_{775} > 1.2$, $i_{775} - z_{850} < 1.3$, $S/N(z_{850}) > 5$ and $S/N(B_{435}) < 3$.

only object detected in X-rays (XID403 in the 4 Ms CDFS catalog of Xue et al. 2011). The remaining two candidates have not been identified spectroscopically. The measured AB magnitudes of XID403 in ACS images are: $V_{606} = 26.84 \pm 0.10, i_{775} = 25.21 \pm 0.04, z_{850} = 25.05 \pm 0.04$. The 5σ detection limit in the B_{435}-band is 28.4 AB mag.

XID403 (J033229.29-275619.5) was recognized as an AGN at $z = 4.76$ based on FORS-2 spectroscopy (Vanzella et al. 2006). Its optical spectrum exhibits a narrow (FWHM$\leq$ 1000 km s^{-1}) Lyα emission line and a broader (FWHM$\sim$ 2000 km s^{-1}) NVλ1240 emission line, with an integrated flux similar to Lyα. A more recent spectrum with DEIMOS/Keck confirms both features (Coppin et al. 2009). The Spectral Energy Distribution of XID403 was published by Coppin et al. (2009). Based on a LABOCA detection at 870μm, they showed that this source is a bright submillimeter galaxy with SFR$\sim$1000 $M_\odot$ yr^{-1}. A large reservoir of molecular gas ($\sim 1.6 \times 10^{10}\, M_\odot$) was also identified through CO(2-1) observations (Coppin et al. 2010).

We considered the same optical to mid-IR datasets used by Coppin et al. (2009) and improved on the SED by adding the detection at 1.1 mm by AzTec/ASTE ($f_{1.1mm} = 3.3 \pm 0.5$mJy; Scott et al. 2010) and the Y, J and Ks magnitudes from the deep NIR imaging by HAWK-I/VLT ($Y_{AB} = 24.56 \pm 0.12$, $J_{AB} = 24.37 \pm 0.14$, $K_{AB} = 24.03 \pm 0.20$; Castellano et al. 2010). This object is also detected (at $\sim 3\sigma$) at 1.4 GHz with a peak flux of 22.3 μJy (N. Miller priv. comm). Unfortunately, it falls just outside the areas covered by the 16μm Spitzer/IRS mosaic (Teplitz et al. 2011) and GOODS-Herschel (PI D. Elbaz). XID403 is not detected in the 3 Ms XMM image of the CDFS.

5.3 X-ray data analysis

A total exposure of $\leq$ 4 Ms has been accumulated on the CDFS as a result of 54 individual observations with ACIS-I performed during three different time periods: $\sim$ 0.8 Ms in 2000, $\sim$ 1 Ms in 2007 and $\sim$ 2 Ms in 2010. X-ray data products, including event files for each observation and also for the merged datasets are publicly

available[2]. In this paper we use the data products by Xue et al. (2011) who derived X-ray source catalogs from a full reprocessing and astrometric recalibration of the event files. We used CIAO v4.1 and the Funtools package[3] to perform X-ray aperture photometry at the position of XID403. The separation between the optical and X-ray centroids is ~ 0.4", which is well within the 1σ X-ray source positional uncertainty ($\sim$0.47"). To maximize the S/N ratio, we measured the source counts in different bands within a small aperture of 3" radius, which encloses $\sim$50% of the PSF at 1.5 keV at the source location ($\sim$ 8 arcmin off-axis). We measured 37.0 ± 8.7 net counts in the 0.9-4 keV band, corresponding to a $\sim 4.2\sigma$ detection[4]. We verified that similar results are obtained when using different local background regions. The hardness ratio, defined as HR = (H-S)/(H+S), where S and H are the net counts observed in the 0.5-2 keV and 2-7 keV bands, respectively, is HR=0.23 ± 0.24 (not corrected for vignetting). This value, for an AGN at $z \sim 5$ with a standard intrinsic spectrum (i.e., $\Gamma = 1.8$) is highly suggestive of heavy obscuration. For comparison, an AGN at $z \sim 5$ with $N_H \leq 10^{23}\mathrm{cm}^{-2}$ is expected to have HR≤ -0.35 at the source position. We extracted the X-ray spectrum in the 0.5-7 keV band using the same 3" radius aperture and verified that below 0.9 keV and above 4 keV the source emission is indistinguishable from the background. The spectrum and response files were created using the `psextract` script in CIAO. Since `psextract` does not account for the PSF fraction when building up the effective area file, we multiplied the 0.5-2 keV and 2-10 keV fluxes as obtained from the spectral fit by a factor of 2 and 2.5, respectively, to recover the full aperture-corrected X-ray fluxes. We found consistent results either using spectral responses extracted from individual observations, or those obtained as an exposure-weighted mean over all individual responses. To double check the reliability of this procedure we also built spectral response files for one of the *Chandra* exposures (ObsID=8594) using the ACIS-Extract software (Broos et al. 2010) which allows proper construction of effective area files at any PSF fraction.

[2]http://cxc.harvard.edu/cda/Contrib/CDFS.html

[3]https://www.cfa.harvard.edu/~john/funtools

[4]XID403 has 82 ± 25 net counts in the 0.5-8 keV band (100% PSF) in Xue et al. (2011), in agreement with our estimate.

Again, consistent results are found when using the ACIS-Extract responses. We analyzed the X-ray spectrum with XSPEC v11.3.2 using the Cash statistic (Cash 1979) to estimate the best-fit parameters. Errors are quoted at 1σ confidence level. We first fitted the data using a powerlaw spectrum modified by galactic absorption, which returns $\Gamma = -0.64^{+1.15}_{-0.73}$. We then used the `plcabs` model (Yaqoob 1997), which follows the propagation of X-ray photons within a uniform, spherical obscuring medium, accounting for both photoelectric absorption and Compton scattering. This model can be used in the case of heavy absorption (up to 5×10^{24} cm^{-2}) and up to rest-frame energies of ~ 20 keV. When fixing the photon index to $\Gamma = 1.8$, we derived a Compton-thick column density of $N_H = 1.4^{+0.9}_{-0.5} \times 10^{24}$ cm^{-2} (see Fig. 1). If we conservatively assume $\Gamma = 1.0$, which is $\geq 4\sigma$ off the average intrinsic AGN value, we still obtain $N_H > 10^{24}$ cm^{-2}. The measured absorption should be interpreted as a lower limit, since a cold reflection model (`pexrav`), corresponding to $N_H \geq 10^{25}$ cm^{-2}, provides an equally good fit. [5] Fitting the data with the recent MYTorus model (Murphy & Yaqoob 2009), which accounts for a toroidal distribution of the obscuring matter, again returns $N_H > 10^{24}$ cm^{-2}. No prominent iron Kα line is observed at 1.1 keV (i.e., 6.4 keV rest-frame), but this is not in conflict with the Compton-thick scenario. Indeed, the *observed* EW scales with $(1+z)^{-1}$, so that EW$_{rest}$ ∼1-2 keV, as is typical of Compton-thick AGN, would translate into EW$_{obs}$ ∼170-340 eV. We verified that such a weak line can be easily accomodated in the fit and that only loose upper limits can be derived for the equivalent width (EW$_{rest} < 4.3$ keV at 90% c.l.). The aperture-corrected X-ray fluxes, as extrapolated from the X-ray fit, are $f_{0.5-2} = 4.2 \pm 1.5 \times 10^{-17}$ erg cm^{-2} s^{-1} and $f_{2-10} = 6.8 \pm 2.4 \times 10^{-16}$ erg cm^{-2} s^{-1}. The intrinsic (de-absorbed), rest-frame 2-10 keV luminosity is $\sim 2.5 \times 10^{44}$ erg s^{-1}, which places XID403 at the low end of the X-ray luminosity range for type-2 quasars. Admittedly, the uncertainties in the geometry of the obscuring (and reprocessing) material might substantially affect the derivation of the intrinsic luminosity. However, we note that, if the spectrum were produced by pure reflection and a typical reflection

[5] When grouping to a minimum of 1 count per bin, the value of the C-statistic over the degrees of freedom is 54.7/59 and 55.2/60 for the `plcabs` and `pexrav` model, respectively.

efficiency of $\sim 2\%$ is assumed (Gilli et al. 2007), the intrinsic luminosity would be even higher.

XID403 was detected in the 1 Ms CDFS catalog by Giacconi et al. (2002, XID=618), with $f_{0.5-2} = 1.6 \pm 0.5 \times 10^{-16}$ erg cm^{-2} s^{-1} and $f_{2-10} < 7.6 \times 10^{-16}$ erg cm^{-2} s^{-1}. The ~ 4 times larger soft X-ray flux is likely due to contamination from high background fluctuations over the larger (8" radius) extraction region adopted in that catalog. We checked the photometry of the 2000, 2007 and 2010 periods separately using a smaller 3" radius: no significant source variability is detected in any band. XID403 was below the detection thresholds of the 1 Ms CDFS catalog by Alexander et al. (2003) and 2Ms CDFS catalogs by Luo et al. (2008).

5.4 Discussion and Conclusions

5.4.1 SED fitting

We searched for additional indicators of heavy obscuration by considering data at other wavelengths. We first investigated the observed (i.e., not corrected for absorption), rest-frame 2-10 keV to $6\mu m$ luminosity diagnostic ratio (X/IR, e.g., Alexander et al. 2008a). We derived the X-ray luminosity from the spectral fit and used the $\sim 4\mu m$ rest-frame luminosity (derived from the Spitzer/MIPS datapoint at 24μm) as a proxy for the $6\mu m$ luminosity. The X/IR ratio of $\sim 5 \times 10^{-3}$ would place XID403 in the region populated by Compton-thick AGN (Alexander et al. 2008a). When considering the $F(24\mu m)/F(R)$ vs $R - K$ color diagram elaborated by Fiore et al. (2009), XID403 would fall in "cell E" , where a significant fraction ($\sim 25 - 30\%$) of galaxies is found to host a heavily obscured, candidate Compton-thick AGN.

We then built the Spectral Energy Distribution (SED) from the X-rays to the radio regime (see Fig.2). As already shown by Coppin et al. (2009), the radio to FIR emission of this source is dominated by dusty star formation, at a rate of $\sim$1000 $M_\odot$ yr^{-1}. We note that X-ray binaries associated to such a high SFR would produce $L^{obs}_{2-10} \sim 2 - 5 \times 10^{42}$ erg s^{-1} (Ranalli et al. 2003; Lehmer et al. 2010), similar to

the *observed* value. However, X-ray binaries have on average much softer spectra ($\Gamma \geq 1.5$, Remillard & McClintock 2006) than observed ($\Gamma = -0.64$). If absorption is invoked to explain such a spectral hardness, then intrinsic luminosities of $\approx 10^{44}$ erg s^{-1} are derived, which are incompatible with X-ray binary emission.

A reasonable match with the MIR to UV datapoints could be obtained with a reddened QSO template with $A_V \sim 0.7 - 0.8$ (adopting the extinction curve of Gaskell & Benker 2007). When converting the measured optical extinction into an equivalent hydrogen column density by applying the relation valid for the Milky Way ISM ($N_H \sim 1.8 \times 10^{21} A_V$), we find $N_H \sim 1.3 \times 10^{21}$ cm^{-2}, which is three dex smaller than what is estimated from the X-ray spectral fit. A mismatch between the X-ray and the optically estimated column density, in the range of $\sim 3 - 100$, is observed in local AGN, calling for a number of interpretations (e.g., low dust-to-gas ratio; Maiolino et al. 2001a). The mismatch observed in XID403 is ∼1000, which would make this object extreme.

In their SED analysis Coppin et al. (2009) suggest a different, stellar origin for the optical/UV rest frame emission. Following the parameterization used by Vignali et al. (2009) and Pozzi et al. (2010) for obscured AGN, we fitted the SED of XID403 with a stellar component, an AGN torus component, and a dusty starburst component. The dusty starburst is responsible for the bulk of the FIR to radio emission, while the AGN torus produces the entire emission at 24μm (4μm rest-frame). A galaxy template with $M_\star \sim 1.2 \times 10^{11} M_\odot$, $A_V \sim 1$ and a ∼1-Gyr-old constant star formation rate nicely fits the optical/UV$_{rest}$ data. However, a possible problem in interpreting the optical/UV$_{rest}$ emission as stellar light is that XID403 is pointlike in the deep HST/ACS images (CLASS_STAR=0.99 in i_{775} and z_{850}), which would imply a half-light radius of < 0.3 kpc. Although very compact morphologies have been observed in a fraction of distant sub-mm galaxies (Ricciardelli et al. 2010), the pointlike nature of XID403, coupled to the presence of broad NV emission, might suggest that the optical/UV$_{rest}$ light has a nuclear origin. In particular, we could be looking at a fraction ($\sim 10\%$) of nuclear radiation that leaks out without being absorbed or is scattered towards us and thus would be polarized. If true, the effective

extinction to the nucleus would be much higher than that estimated by fitting the whole MIR to UV emission with a reddened QSO template, being more in line with the large X-ray column density. This interpretation has been already proposed by Polletta et al. (2008) to explain the relatively blue optical/UV emission and broad line components of two sub-mm galaxies at $z \sim 3.5$ hosting heavily obscured AGN, similar to XID403. Also, although the stellarity parameter is uncertain for the faint K-band detection, the decrease of CLASS_STAR from 0.95 in Y to 0.74 in K may also suggest that the host galaxy contributes significantly only at $\lambda_{rest} > 4000$Å. In Fig.2 we show a possible SED decomposition for XID403 obtained by adding an AGN torus component and a scattering component (corresponding to $\sim 10\%$ of the AGN intrinsic UV emission[6]) to the SED of Arp220. In summary, the full SED analysis shows that XID403 is not a classic, type-2 QSO (i.e., a narrow-line, X-ray obscured AGN whose physical properties can be explained within the standard, geometry-based Unified Model; Norman et al. 2002), but points to a complex physical picture likely related to its active assembly phase.

5.4.2 Black hole and stellar mass growth

The IR emission from the AGN torus and the measured X-ray emission are used (see e.g., Vignali et al. 2009; Pozzi et al. 2010) to derive an AGN bolometric power of 7×10^{45} erg s^{-1}. Assuming that the BH is radiating at the Eddington limit, as might be expected during these active BH and galaxy build-up phases, would imply $M_{BH} = 5 \times 10^7\, M_{\odot}$. This in turn gives $M_{BH}/M_{\star} \sim 4 \times 10^{-4}$, which is a factor of 5 smaller than the local value. It would then seem that both BH and stellar mass are rapidly growing towards their final values, but the BH is lagging behind as seen in sub-mm galaxies at $z \sim 2$ (Alexander et al. 2008b) and expected by recent semi-analytic models of BH/galaxy formation (Lamastra et al. 2010). However, since the estimated BH mass is a lower limit (accretion might be sub-Eddington) and the stellar mass derived in the previous section might be an upper limit (the AGN likely contributes

[6]The intrinsic AGN UV emission is estimated by normalizing the QSO template of Elvis et al. (1994) to the Spitzer/MIPS datapoint.

to the optical/UV$_{rest}$ light), this ratio might well be equal to the local value.

5.4.3 Expectations for high-z Compton-thick AGN

While the space density of luminous, unobscured and moderately obscured QSOs declines exponentially at $z \geq 3$ (e.g., Brusa et al. 2009; Civano et al. 2011), the behaviour of heavily obscured objects has still to be properly determined. Semi-analytic models of BH/galaxy evolution linking the obscuration on nuclear scales to the gas availability in the host galaxy (e.g., Menci et al. 2008), would predict an increasing abundance of obscured AGN towards high redshifts, and some observational evidence of this trend has been reported (Treister et al. 2009 and references therein).

We considered the number of Compton-thick AGN as expected from the synthesis model by Gilli et al. (2007). XID403 is detected with a 2-10 keV flux ~ 2 times larger than the detection limit at its position. The mean limiting flux over the 160 arcmin^2 GOODS-S area is $f_{2-10} = 1.5 \times 10^{-16}$ erg cm^{-2} s^{-1}. Using the Gilli et al. (2007) model, one would expect from 0.06 to 0.6 Compton-thick AGN in the range of $4.7 < z < 5.7$ with $f_{2-10} > 3 \times 10^{-16}$ erg cm^{-2} s^{-1} in GOODS-S, depending on whether their space density undergoes the same high-z decline as observed for less obscured QSOs or stays nearly constant. Clearly, any firm conclusion is prevented by the low statistics. However, the mere presence of a Compton-thick AGN at $z > 4$ in such a small area (and this could be a lower limit since we did not investigate the whole X-ray source catalog) might suggest that the space density of Compton-thick AGN is not rapidly declining towards high redshifts. This shows that the detection of even a small number of heavily obscured AGN at $z > 4$ in ultra-deep X-ray surveys would have a strong leverage on our understanding of early BH evolution.

X-ray spectral analysis is the only unambiguous way to determine whether an AGN is shrouded by Compton-thick matter. Observations at energies above 10 keV are an obvious way to identify Compton-thick AGN, but the current high-energy instrumentation and that foreseen in the near future ($NuSTAR$, $Astro-H$) will not allow sampling objects beyond $z \sim 1 - 1.5$. Below 10 keV, sensitive observations

with limiting fluxes of $\approx 10^{-17}$ erg cm^{-2} s^{-1} over wide sky areas, such as those from the proposed missions IXO (White et al. 2010) and $WFXT$ (Murray et al. 2010), would be required. The only concrete way to detect and unambiguously recognize high-z Compton-thick AGN in the near future is through even deeper observations with $Chandra$.

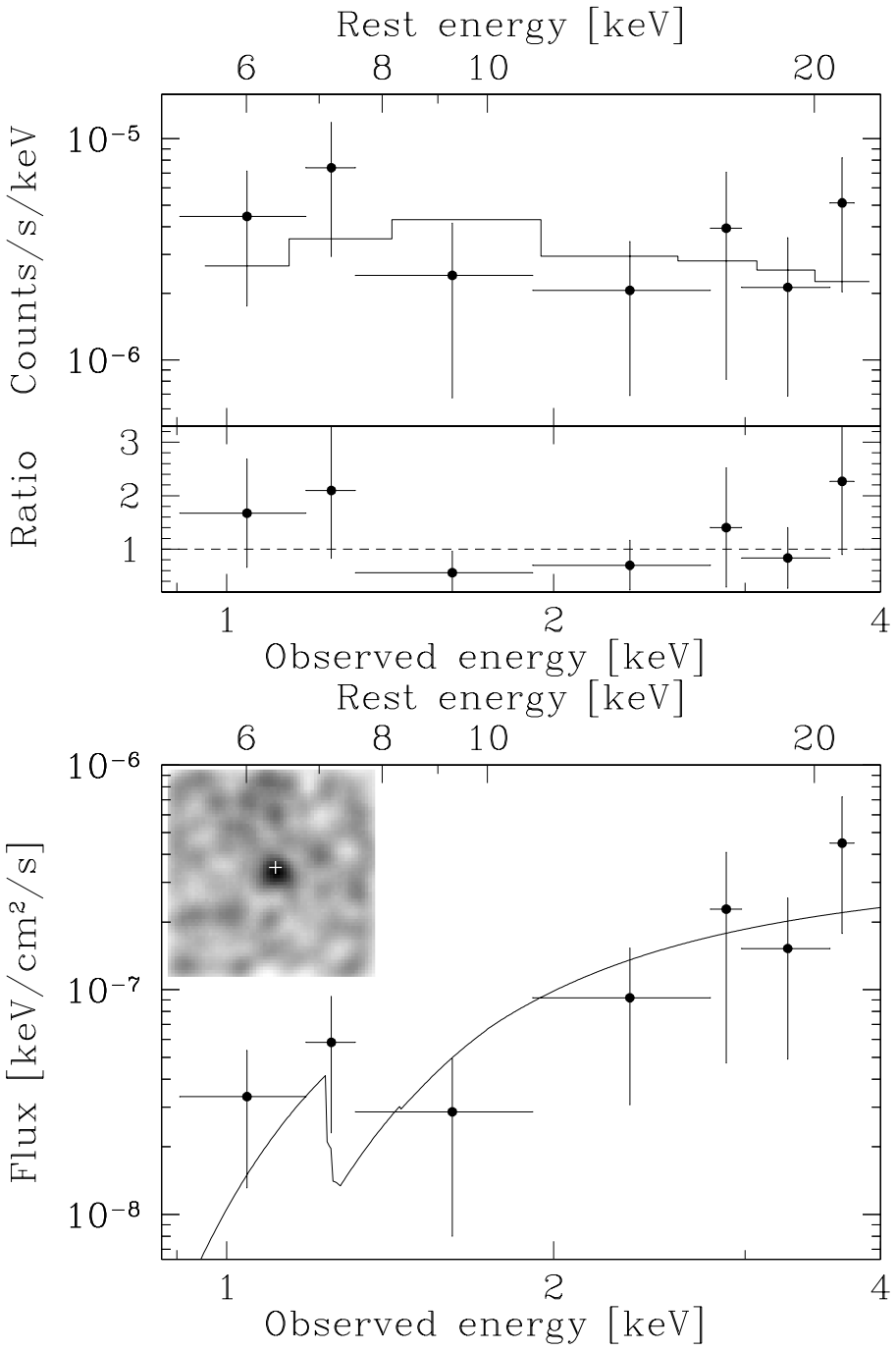

Figure 5.1 *Top* : The observed 4 Ms *Chandra* X-ray spectrum of XID403 and best-fit model (data/model ratio in the bottom panel). A best fit column density of $N_H = 1.4^{+0.9}_{-0.5} \times 10^{24}$ cm^{-2} is obtained when assuming $\Gamma = 1.8$. The spectrum has been rebinned for display purposes. *Bottom* : Response corrected spectrum and best fit model. The inset shows a smoothed 0.5–4 keV image of XID403 (size is 30"×30"). The cross marks the position of the optical V-dropout.

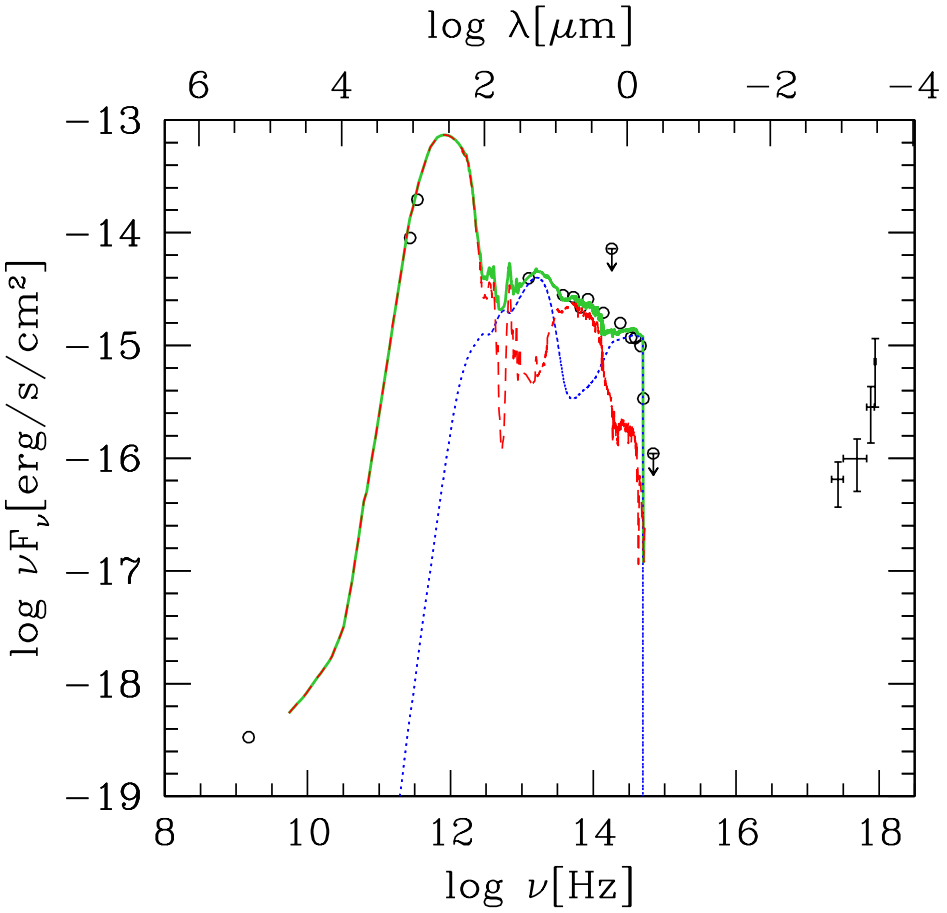

Figure 5.2 Spectral energy distribution of XID403 (observed frame) and possible decomposition into a galaxy component (red dashed line) and an AGN component (blue dotted line). The green solid line is the sum of the two. The template of Arp 220 shifted to $z = 4.76$ is adopted for the galaxy emission. The sum of a torus and a scattered component is adopted for the AGN emission (see text).

Chapter 6

SUMMARY & FUTURE PROSPECTS

6.1 Discoveries

Over the course of this thesis, we have extended significantly the sample size of high-redshift galaxies and quasars. By visiting all the deep fields made available by the HST, we have identified thousands of high-redshift galaxies, especially at $z > 6$ (cf, Table 1.1). This makes our sample statistically more significant than previous studies.

We have greatly improved the methodology in this field, by developing a set of innovations in dealing with images and data, compared to other groups (e.g., Bouwens et al. 2007). To make optimal use of information, we investigate un-binned data without grouping them. To avoid possible uncertainties brought on by large corrections when close to the detection limit of the surveys, we adopt a moderate magnitude cut to exclude the faintest sources. To take into account scattering in and out of the dropout sample due to photometric errors, we introduce the f-factor technique to take a probabilistic view at these candidates. To overcome the effect from the very uncertain relation between parameters, we modify the maximum likelihood process. To estimate the generally agreed LF parameters assuming all the current

studies are independent and correct, we introduce Bayesian and global statistical method (Chapter 2). All the above lead our results to be more robust and more reliable.

We have successfully reached a series of conclusive results to better understand of some of the major questions of cosmology posed in Chapter 1, e.g., what are the first objects to light up the universe after the dark ages? We recognize that there are more faint galaxies at high redshifts than previously expected (Chapter 2 and 3), meanwhile fewer faint quasars (Chapter 4), which suggests that galaxies are the main sources to keep ionizing the universe. This observation also confirms the model of hierarchical build-up of masses of galaxies. We study the luminosity function and the luminosity density over a time scale of one billion years, from the very end of the dark ages to the well-established epoch of reionization (Chapter 1). A constant normalization, a slowly steepening slope, and a relatively rapidly dimming characteristic luminosity towards higher redshifts can best describe the evolution of the luminosity function from 600 Myr to 1.6 Gyr (Chapter 3). Those discoveries will help guide future theoretical and observational studies.

Several closely related projects have progressed. For example, the previously thought-to-be distant galaxy, J033238.80-274953.7, is discovered to be actually a star in our Milky Way, suggested by its four-year proper motion (Chapter 3). The most distant obscured quasar, namely, J033229.29-275619.5, has also been found by carefully matching its images from several space telescopes, including the HST and the Chandra (Chapter 5).

We will continue on our journey to further understand the early universe.

6.2 Future Works

The Committee for a Decadal Survey of Astronomy and Astrophysics (2010) has suggested three priority science objects for the decade 2012-2021. One of them is exactly what we are doing, i.e., searching for the first stars, galaxies, and black holes. The discoveries in the area have already been two of the ten most important

achievements of the Hubble Space Telescope[1].

There is much work still in progress. One of our ongoing projects would be supplementing the study of the galaxy LF at redshift region $4 < z < 9$ by including data from more fields, e.g., the BoRG and the CANDELS. An initial study has shown an overdensity at $z \sim 8$ in one of the fields. We will explore whether the evidence of evolution of the LF parameters is statistically significant. A second ongoing project is to identify quasars by cross-correlating optical dropouts with deep X-ray and IR observations. The detections in the X-ray or IR images would enhance greatly the chance of being high-redshift sources for these dropouts in optical bands. We have initialized the search for B_{435}-dropouts in the E-CDFS field and compared them with available catalogs, e.g., Cardamone et al. (2010) and Rafferty et al. (2011). A principal component analysis shows the latter catalog performs better in matching photometric redshifts with spectroscopic redshifts within the redshift window we are interested in.

To find B_{435}-dropouts designed to $3 < z < 5$, we ask for

$$B_{435} - V_{606} > 1.1 + (V_{606} - z), \tag{6.1}$$

$$B_{435} - V_{606} > 1.1, \tag{6.2}$$

$$V_{606} - z_{850} < 1.6, \tag{6.3}$$

$$S/N(V_{606}) > 5, \tag{6.4}$$

$$S/N(i_{775}) > 3, \tag{6.5}$$

following Papovich et al. (2004) as many other groups (e.g., Beckwith et al. 2006, Bouwens et al. 2007, Stark et al. 2009, Dahlen et al. 2010). The selection criteria are slightly relaxed to maximize the completeness of the detection, instead of minimizing the contaminations as in Giavalisco et al. (2004). In this way, we have identified about 1100 sources[2] brighter than magnitude 27.5 which include almost all the confirmed

[1] http://www.nasa.gov.

[2] We ask for detections in both V-band and i-band and signal as its 2-σ limit for the B-band during non-detection. Instead, Dahlen et al. (2010) ask for z-band detection and 1-σ limit for the B-band during non-detection so that they find 2129 B-dropouts including very faint $z_{850} \sim 28.5$ ones.

$3 < z < 5$ sources in the GOODS-South field.

We would also like to study small number statistics to improve reliability of the results. This is especially useful in the study of $z \geq 6$ galaxies and quasars where only tens of objects are available. Besides, we are interested in the clustering properties of the early sources. Kolmogorov-Smirnov tests and Landy-Szalay estimators have been conducted on the HUDF to reach some preliminary but inclusive results. There is less than a 5% probability that the bright i_{775}-dropouts ($z_{850} < 27.5$) or the faint i_{775}-dropouts ($z_{850} > 27.5$) be so arranged by chance. The work should be extended to different redshift windows, with the correlation function also being well constrained.

The James Webb Space Telescope (JWST), scheduled for launch in 2018, will provide unparalleled sensitivity in the infrared to pinpoint the first galaxies and quasars. With a 10 ks exposure time, the JWST will detect point sources as faint as mag 29 with a 10σ significance[3]. In comparison, the ground-based observatory Gemini can only find bright objects of mag $20 - 24$ in the near-infrared. Other instruments, such as the Giant Segmented Mirror Telescope (GSMT), planned for construction over the coming decade, will render within spectroscopic reach the most distant objects imaged by the JWST. We will take advantage of their images and spectra to finally solve the mysteries of the first sources.

[3]http://www.stsci.edu/jwst/science/sensitivity.

Appendix A

More About Photometric Scatter and Flux Boosting

We assume the photometric scatter is in a Gaussian distribution, thus the probability of a galaxy arriving on the detector as magnitude m but cataloged in m' equals

$$G(m, m', \sigma) = \frac{1}{\sqrt{2\pi\sigma^2}} \exp[-\frac{(m-m')^2}{2\sigma^2}] \tag{A.1}$$

and the measured LF will be

$$\phi'(m) \quad = \quad \int \phi(m') G(m, m', \sigma) dm' \tag{A.2}$$

where ϕ is the actual LF, i.e., Equation (7) in Chapter 2.3.3 .

When the photometric error σ is very small, G takes the limit of the Dirac function and it is always true $\phi' \equiv \phi$. When the surveys are pushed close to the detection limit, σ is not negligible and also far from uniform in the magnitude window. To satisfy $S/N = 10$ at $m = m_*$ and $S/N = 5$ at $m = m_* + 2.5$, a guess would be

$$\sigma(m) = \frac{2.5}{\ln 10} \frac{1}{2(m_* - m) + 10} \tag{A.3}$$

Simulations show that the effect of flux boosting from fainter magnitudes outside our selection window is negligible. But as shown in Table A.1, if $\sigma(m)$ increases much

Table A.1. The Steepening of α by the flux boosting for $\sigma(m) \propto 10^{0.3(m-m_*)}$

	$\alpha = -1.5$	$\alpha = -1.7$	$\alpha = -1.9$
$S/N > 3$	0.14	0.18	0.26
$S/N > 5$	0.03	0.04	0.08
$S/N > 7$	0.01	0.02	0.03

faster with m, or if lower S/N candidates are included, there will be considerable steepening at the faint end due to the photometric scattering. We simulate 4000 objects according to the given LF parameters, i.e., m_* is fixed and α = -1.7 in [m_*-3.5,m_*+4.5]. Their magnitude errors are assumed to be in the form of $10^{0.3(m-m_*)}$ which comes from the real data of the HUDF. For each realization, the change of magnitudes brought by their errors will also change their detected S/N. We choose those with the S/N> 5 and lying within [m_*-2.5,m_*+2.5] to determine the slope. This process repeats for different combinations of S/N> 5, 7, 9 and α = -1.5, -1.7, -1.9. We can see from Table A.1 that if the S/N is kept $>$ 5, the steepening of the faint end slope by the flux boosting is less than 0.1.

Appendix B

Physical Concepts

B.1 Cosmology

Spectroscopy requires identification of spectral lines (typically emission lines) and record their wavelength λ. The relative shift of these lines (λ_o) compared to their known positions measured in the laboratory (λ_e) allows us to measure the redshift. A photon will be observed to have a wavelength $\lambda_o = (1+z)\lambda_e$ if it is emitted in a wavelength λ_e at redshift z.

The Hubble constant $H_0 = v/d$ can be measured by averaging the ratio of the distance d of an astronomical objects to its escape speed v away from us. Luminosity distance

$$D_L \equiv \sqrt{\frac{L}{4\pi F}} = (1+z)D_C \tag{B.1}$$

is useful when we want to know how bright an object looks like at the line-of-sight comoving distance $D_C = D_H \int_0^z \frac{dz'}{E(z')}$. Here the Hubble distance $D_H \equiv c/H_0$ and $E(z) = \sqrt{\Omega_M(1+z)^3 + (1-\Omega_M)}$. Ω_M is the ratio relative the critical density for matter today. When the universe is expanding, we always use the concept of comoving volume

$$V_C = 4\pi/3\ D_C^3 \tag{B.2}$$

$$\frac{dV_C}{dz} = \frac{D_C^2}{E(z)} D_H d\Omega \tag{B.3}$$

The K-corrected absolute magnitude in the rest frame of an object is given by,

$$M = m - 5\log(D_L) - K, \tag{B.4}$$

where K is the corresponding K-correction as to, e.g., Hogg et al. (2002).

B.2 Ionization

The number of ionizing photons required to maintain ionizing the universe at redshift z is (Madau et al. 1999):

$$\dot{N}(z) = \frac{n_H(0)}{t_{rec}(z)} \sim 2.5 \times 10^{47} C(1+z)^3 [\text{Mpc s}^{-1}], \tag{B.5}$$

where $n_H(0)$ is the hydrogen number density, $t_{rec}(z)$ is the time scale of hydrogen+electron recombination, and $C \equiv < \rho_{HI}^2 > / < \rho_{HI} >^2$ is the clumpiness factor of neutral hydrogen due to the inhomogeneities on large scale. On the other hand, the production rate of ionizing photons is

$$\dot{n}_c \sim f_{esc} \ \times 10^{13} L_\nu \tag{B.6}$$

where f_{esc} is the escape factor of ionizing photons from the sources to the IGM. Therefore, if $\dot{n}_c$ of one kind of source is larger than $\dot{N}(z)$, then this source can keep the universe ionized at the given redshift.

B.3 Black Hole

For spherical accretion of ionized gas, the bolometric luminosity emitted by a black hole has a maximum value beyond which radiation pressure prevents gas accretion,

$$L_E = 1.45 \times 10^{46} (\frac{M_{BH}}{10^8 M_\odot}) (\text{erg s}^{-1}) \tag{B.7}$$

The total luminosity of a black hole is related to its mass accretion rate by the radiative efficiency ϵ,

$$L = \epsilon \dot{M}_{BH} c^2 \tag{B.8}$$

The accretion time can be defined as

$$\tau = \frac{M_{BH}}{\dot{M}_{BH}} = 4 \times 10^7 (\frac{\epsilon}{0.1})(\frac{L}{L_E})^{-1} \; yr \tag{B.9}$$

The fact that τ is much shorter than the age of the universe even at high redshift implies that BH growth is mainly limited by its total fuel reservoir.

Nuclear fusion releases $\sim 7 \times 10^6$ eV per hydrogen atom, and thin-disk accretion onto black hole release 10 times more energy. It is therefore sufficient to convert a small fraction, i.e., $\sim 10^{-5}$, of the total baryonic mass into stars or BHs to ionize the rest of the universe at z$\leq$3, because the ionization of hydrogen requires only 13.6 eV.

B.4 Star Formation Rate

Observations of the star formation rates (SFR) in galaxies provide vital clues to the physical nature of the Hubble sequence and are key probes of the evolutionary history of galaxies (Kennicutt 1998). When the integrated spectrum is dominated by young stars, the SFR scales linearly with luminosity. Converting the calibration of Madau et al. (1998) to Salpeter's (1955) initial mass function (IMF) with mass limits 0.1 and 100 $M_\odot$ yields

$$\text{SFR } [M_\odot \text{ yr}^{-1}] = 1.4 \times 10^{-28} L_\nu [\text{ergs s}^{-1} \text{ Hz}^{-1}], \tag{B.10}$$

thanks to the fact that for a Salpeter IMF, the composite UV spectrum happens to be nearly flat in L_ν over the wavelength 1500-2800 Å. This equation applies to galaxies with continuous star formation over time scales of 10^8 years or longer.

Bibliography

Abazajian, K. N., et al. 2009, ApJS, 182, 543

Akylas, A., & Georgantopoulos, I. 2009, A&A, 500, 999

Alexander, D. M., et al. 2003, AJ, 126, 539

—. 2008a, ApJ, 687, 835

—. 2008b, AJ, 135, 1968

Amsler, C. 1998, Rev. Mod. Phys., 70, 1293

Arkani-Hamed, N., Dimopoulos, S., & Dvali, G. R. 1998, Phys. Lett., B429, 263

Avni, Y. 1976, ApJ, 210, 642

Balbus, S. A., & Hawley, J. F. 1991, ApJ, 376, 214

Balestra, I., et al. 2010, A&A, 512, A12+

Ballantyne, D. R., & Papovich, C. 2007, ApJ, 660, 988

Barger, A. J., Cowie, L. L., Brandt, W. N., Capak, P., Garmire, G. P., Hornschemeier, A. E., Steffen, A. T., & Wehner, E. H. 2002, AJ, 124, 1839

Barger, A. J., Cowie, L. L., Capak, P., Alexander, D. M., Bauer, F. E., Brandt, W. N., Garmire, G. P., & Hornschemeier, A. E. 2003, ApJ, 584, L61

Barger, A. J., Cowie, L. L., Mushotzky, R. F., Yang, Y., Wang, W.-H., Steffen, A. T., & Capak, P. 2005, AJ, 129, 578

Barkana, R., & Loeb, A. 2001, Phys. Rep., 349, 125

Bauer, F. E., Yan, L., Sajina, A., & Alexander, D. M. 2010, ApJ, 710, 212

Beckwith, S. V. W., et al. 2006, AJ, 132, 1729

Bennett, C. L. 2005, Science, 307, 879

Bertin, E., & Arnouts, S. 1996, A&AS, 117, 393

Boquien, M., et al. 2010, ApJ, 713, 626

Bouwens, R. J., Illingworth, G. D., Blakeslee, J. P., & Franx, M. 2006, ApJ, 653, 53

Bouwens, R. J., Illingworth, G. D., Franx, M., & Ford, H. 2007, ApJ, 670, 928

—. 2008, ApJ, 686, 230

Bouwens, R. J., et al. 2004, ApJ, 606, L25

—. 2009, ApJ, 705, 936

—. 2010a, ApJ, 709, L133

—. 2010b, ArXiv e-prints

—. 2010c, ApJ, 708, L69

—. 2011a, Nature, 469, 504

—. 2011b, ArXiv e-prints

Brandt, W. N., Guainazzi, M., Kaspi, S., Fan, X., Schneider, D. P., Strauss, M. A., Clavel, J., & Gunn, J. E. 2001, AJ, 121, 591

Brandt, W. N., & Hasinger, G. 2005, ARA&A, 43, 827

Bromm, V., Yoshida, N., Hernquist, L., & McKee, C. F. 2009, Nature, 459, 49

Broos, P. S., Townsley, L. K., Feigelson, E. D., Getman, K. V., Bauer, F. E., & Garmire, G. P. 2010, ApJ, 714, 1582

Brusa, M., et al. 2009, ApJ, 693, 8

Bruzual, G., & Charlot, S. 2003, MNRAS, 344, 1000

Bunker, A. J., Stanway, E. R., Ellis, R. S., & McMahon, R. G. 2004, MNRAS, 355, 374

Bunker, A. J., et al. 2010, MNRAS, 409, 855

Caputi, K. I., Dunlop, J. S., McLure, R. J., & Roche, N. D. 2004, MNRAS, 353, 30

Cardamone, C. N., et al. 2010, ApJS, 189, 270

Carroll, S. M. 2004, in American Institute of Physics Conference Series, Vol. 743, The New Cosmology: Conference on Strings and Cosmology, ed. R. E. Allen, D. V. Nanopoulos, & C. N. Pope, 16–32

Cash, W. 1979, ApJ, 228, 939

Castellano, M., et al. 2010, A&A, 524, A28+

Cho, J. 2000, PhD thesis, The University of Texas at Austin

Cho, J., Lazarian, A., & Vishniac, E. T. 2003, in Lecture Notes in Physics, Berlin Springer Verlag, Vol. 614, Turbulence and Magnetic Fields in Astrophysics, ed. E. Falgarone & T. Passot, 56–98

Ciardi, B., & Ferrara, A. 2005, Space Sci. Rev., 116, 625

Cimatti, A., et al. 2004, Nature, 430, 184

Civano, F., et al. 2011, ArXiv e-prints

Coe, D., Benítez, N., Sánchez, S. F., Jee, M., Bouwens, R., & Ford, H. 2006, AJ, 132, 926

Comastri, A. 2004, in Astrophysics and Space Science Library, Vol. 308, Supermassive Black Holes in the Distant Universe, ed. A. J. Barger, 245–+

Comastri, A., et al. 2011, A&A, 526, L9+

Cool, R. J., et al. 2006, AJ, 132, 823

Coppin, K. E. K., et al. 2009, MNRAS, 395, 1905

—. 2010, MNRAS, 407, L103

Cristiani, S., et al. 2004, ApJ, 600, L119

Croom, S. M., Smith, R. J., Boyle, B. J., Shanks, T., Miller, L., Outram, P. J., & Loaring, N. S. 2004, MNRAS, 349, 1397

Daddi, E., et al. 2007, ApJ, 670, 173

Dahlen, T., et al. 2010, ApJ, 724, 425

Damen, M., et al. 2011, ApJ, 727, 1

Diamond-Stanic, A. M., et al. 2009, ApJ, 699, 782

Dickinson, M., et al. 2004, ApJ, 600, L99

Dow-Hygelund, C. C., et al. 2007, ApJ, 660, 47

Efstathiou, G., Ellis, R. S., & Peterson, B. A. 1988, MNRAS, 232, 431

Elvis, M., et al. 1994, ApJS, 95, 1

Fabian, A. C. 1999, MNRAS, 308, L39

Fan, X., Carilli, C. L., & Keating, B. 2006a, ARA&A, 44, 415

Fan, X., et al. 2001, AJ, 122, 2833

—. 2003, AJ, 125, 1649

—. 2004, AJ, 128, 515

—. 2006b, AJ, 131, 1203

—. 2006c, AJ, 132, 117

Ferguson, H. C., et al. 2004, ApJ, 600, L107

Feruglio, C., Daddi, E., Fiore, F., Alexander, D. M., Piconcelli, E., & Malacaria, C. 2011, ApJ, 729, L4+

Finkelstein, S. L., Papovich, C., Giavalisco, M., Reddy, N. A., Ferguson, H. C., Koekemoer, A. M., & Dickinson, M. 2010, ApJ, 719, 1250

Fiore, F., et al. 2009, ApJ, 693, 447

—. 2011, ArXiv e-prints

Fisher, R. A. 1922, Philos. Trans. Roy. Soc. London Ser. A, 222, 309

Fontanot, F., Cristiani, S., Monaco, P., Nonino, M., Vanzella, E., Brandt, W. N., Grazian, A., & Mao, J. 2007, A&A, 461, 39

Ford, H. C., et al. 2003, in Presented at the Society of Photo-Optical Instrumentation Engineers (SPIE) Conference, Vol. 4854, Society of Photo-Optical Instrumentation Engineers (SPIE) Conference Series, ed. J. C. Blades & O. H. W. Siegmund, 81–94

Fritz, J., Franceschini, A., & Hatziminaoglou, E. 2006, MNRAS, 366, 767

Gaskell, C. M., & Benker, A. J. 2007, ArXiv e-prints

Giacconi, R., et al. 2002, ApJS, 139, 369

Giavalisco, M. 2002, ARA&A, 40, 579

Giavalisco, M., & the GOODS Team. 2008, in preparation

Giavalisco, M., et al. 2004, ApJ, 600, L93

Gilli, R., Comastri, A., & Hasinger, G. 2007, A&A, 463, 79

Gilli, R., et al. 2011, ApJ, 730, L28+

Glazebrook, K., et al. 2004, Nature, 430, 181

Glikman, E., Djorgovski, S. G., Stern, D., Dey, A., Jannuzi, B. T., & Lee, K.-S. 2011, ApJ, 728, L26+

Godfrey, S., & Napolitano, J. 1999, Rev. Mod. Phys., 71, 1411

Goto, T. 2006, MNRAS, 371, 769

Grazian, A., et al. 2006, A&A, 449, 951

—. 2010, ArXiv e-prints

Grogin, N. A., et al. 2011, ArXiv e-prints

Gunn, J. E., & Peterson, B. A. 1965, ApJ, 142, 1633

Haiman, Z. 2009, Observing the First Stars and Black Holes, ed. Thronson, H. A., Stiavelli, M., & Tielens, A., 385–+

Haiman, Z., Madau, P., & Loeb, A. 1999, ApJ, 514, 535

Harwit, M. 2006, Astrophysical Concepts, ed. Harwit, M.

Hathi, N. P., Malhotra, S., & Rhoads, J. E. 2008, ApJ, 673, 686

Heckman, T. M., Kauffmann, G., Brinchmann, J., Charlot, S., Tremonti, C., & White, S. D. M. 2004, ApJ, 613, 109

Heckman, T. M., et al. 2011, ApJ, 730, 5

Hogg, D. W., Baldry, I. K., Blanton, M. R., & Eisenstein, D. J. 2002, ArXiv Astrophysics e-prints

Hopkins, A. M. 2004, ApJ, 615, 209

Hopkins, A. M., & Beacom, J. F. 2006, ApJ, 651, 142

Hopkins, P. F., Hernquist, L., Cox, T. J., Di Matteo, T., Robertson, B., & Springel, V. 2005, ApJ, 632, 81

Hopkins, P. F., Richards, G. T., & Hernquist, L. 2007, ApJ, 654, 731

Jiang, L., et al. 2008, AJ, 135, 1057

—. 2009, AJ, 138, 305

Johnston, R. 2011, ArXiv e-prints

Jose, C., Samui, S., Subramanian, K., & Srianand, R. 2011, ArXiv e-prints

Kennicutt, Jr., R. C. 1998, ARA&A, 36, 189

Kim, J. E., Langacker, P., Levine, M., & Williams, H. H. 1981, Rev. Mod. Phys., 53, 211

Kim, S., et al. 2009, ApJ, 695, 809

Kochanek, C. S., et al. 2001, ApJ, 560, 566

Koekemoer, A. M., Fruchter, A. S., Hook, R. N., Hack, W., & Hanley, C. 2006, in The 2005 HST Calibration Workshop: Hubble After the Transition to Two-Gyro Mode, ed. A. M. Koekemoer, P. Goudfrooij, & L. L. Dressel, 423–+

Komatsu, E., et al. 2011, ApJS, 192, 18

Kron, R. G. 1980, ApJS, 43, 305

Labbé, I., Bouwens, R., Illingworth, G. D., & Franx, M. 2006, ApJ, 649, L67

Lamastra, A., Menci, N., Maiolino, R., Fiore, F., & Merloni, A. 2010, MNRAS, 405, 29

Landy, S. D., & Szalay, A. S. 1993, ApJ, 412, 64

Langer, N., Norman, C. A., de Koter, A., Vink, J. S., Cantiello, M., & Yoon, S.-C. 2007, A&A, 475, L19

Laurino, O., D'Abrusco, R., Longo, G., & Riccio, G. 2011, ArXiv e-prints

Lee, K.-S., Giavalisco, M., Gnedin, O. Y., Somerville, R. S., Ferguson, H. C., Dickinson, M., & Ouchi, M. 2006, ApJ, 642, 63

Lehmer, B. D., Alexander, D. M., Bauer, F. E., Brandt, W. N., Goulding, A. D., Jenkins, L. P., Ptak, A., & Roberts, T. P. 2010, ApJ, 724, 559

Lehnert, M. D., et al. 2010, Nature, 467, 940

Liddle, A. 2003, An Introduction to Modern Cosmology, Second Edition, ed. Liddle, A.

Lin, H., Kirshner, R. P., Shectman, S. A., Landy, S. D., Oemler, A., Tucker, D. L., & Schechter, P. L. 1996, ApJ, 464, 60

Ling, E. N., Barrow, J. D., & Frenk, C. S. 1986, MNRAS, 223, 21P

Loeb, A., & Barkana, R. 2001, ARA&A, 39, 19

Loeb, A., Ferrara, A., & Ellis, R. S. 2008, First Light in the Universe, ed. Loeb, A., Ferrara, A., & Ellis, R. S.

Lorenzoni, S., Bunker, A. J., Wilkins, S. M., Stanway, E. R., Jarvis, M. J., & Caruana, J. 2011, MNRAS, 623

Lubow, S. H., Papaloizou, J. C. B., & Pringle, J. E. 1994, MNRAS, 267, 235

Luo, B., et al. 2008, ApJS, 179, 19

Madau, P. 1995, ApJ, 441, 18

Madau, P., Haardt, F., & Rees, M. J. 1999, ApJ, 514, 648

Mahabal, A., Stern, D., Bogosavljević, M., Djorgovski, S. G., & Thompson, D. 2005, ApJ, 634, L9

Maiolino, R., Marconi, A., & Oliva, E. 2001a, A&A, 365, 37

Maiolino, R., Marconi, A., Salvati, M., Risaliti, G., Severgnini, P., Oliva, E., La Franca, F., & Vanzi, L. 2001b, A&A, 365, 28

Malhotra, S., et al. 2005, ApJ, 626, 666

Mannucci, F., Buttery, H., Maiolino, R., Marconi, A., & Pozzetti, L. 2007, A&A, 461, 423

Marconi, A., Risaliti, G., Gilli, R., Hunt, L. K., Maiolino, R., & Salvati, M. 2004, MNRAS, 351, 169

Marshall, H. L. 1985, ApJ, 299, 109

McGreer, I. D., Becker, R. H., Helfand, D. J., & White, R. L. 2006, ApJ, 652, 157

McKee, C. F., & Ostriker, E. C. 2007, ARA&A, 45, 565

McLure, R. J., Cirasuolo, M., Dunlop, J. S., Foucaud, S., & Almaini, O. 2009, MNRAS, 395, 2196

McLure, R. J., Dunlop, J. S., Cirasuolo, M., Koekemoer, A. M., Sabbi, E., Stark, D. P., Targett, T. A., & Ellis, R. S. 2010, MNRAS, 403, 960

McLure, R. J., et al. 2011, ArXiv e-prints

Melia, F. 2003, The Edge of Infinity, ed. Melia, F.

Ménard, B., Scranton, R., Fukugita, M., & Richards, G. 2010, MNRAS, 405, 1025

Menci, N., Fiore, F., Puccetti, S., & Cavaliere, A. 2008, ApJ, 686, 219

Miller, J. M. 2007, ARA&A, 45, 441

Mirabel, I. F., & Rodríguez, L. F. 1999, ARA&A, 37, 409

Miyaji, T., & Griffiths, R. E. 2002, ApJ, 564, L5

Mobasher, B., et al. 2005, ApJ, 635, 832

Momjian, E., Carilli, C. L., & McGreer, I. D. 2008, AJ, 136, 344

Mortlock, D. J., Patel, M., Warren, S. J., Hewett, P. C., Venemans, B. P., McMahon, R. G., & Simpson, C. J. 2011a, ArXiv e-prints

Mortlock, D. J., et al. 2009, A&A, 505, 97

—. 2011b, Nature, 474, 616

Muñoz, J. A. 2011, ArXiv e-prints

Murphy, K. D., & Yaqoob, T. 2009, MNRAS, 397, 1549

Murray, S. S., et al. 2010, in Society of Photo-Optical Instrumentation Engineers (SPIE) Conference Series, Vol. 7732, Society of Photo-Optical Instrumentation Engineers (SPIE) Conference Series

Norman, C., et al. 2002, ApJ, 571, 218

—. 2004, ApJ, 607, 721

Oesch, P. A., et al. 2007, ApJ, 671, 1212

—. 2010, ApJ, 709, L16

—. 2011, ArXiv e-prints

Oke, J. B., & Gunn, J. E. 1983, ApJ, 266, 713

Oke, J. B., & Sandage, A. 1968, ApJ, 154, 21

Osmer, P. S. 2004, Coevolution of Black Holes and Galaxies, 324

Papovich, C., et al. 2004, ApJ, 600, L111

Peebles, P. J. E. 1993, Principles of Physical Cosmology, ed. Peebles, P. J. E.

Pentericci, L., et al. 2011, ArXiv e-prints

Pickles, A. J. 1998, PASP, 110, 863

Polletta, M., et al. 2008, A&A, 492, 81

Pozzi, F., et al. 2010, A&A, 517, A11+

Press, W. H. 1997, in Unsolved Problems in Astrophysics, ed. J. N. Bahcall & J. P. Ostriker, 49–60

Rafferty, D. A., Brandt, W. N., Alexander, D. M., Xue, Y. Q., Bauer, F. E., Lehmer, B. D., Luo, B., & Papovich, C. 2011, ArXiv e-prints

Ranalli, P., Comastri, A., & Setti, G. 2003, A&A, 399, 39

Reddy, N. A., & Steidel, C. C. 2009, ApJ, 692, 778

Remillard, R. A., & McClintock, J. E. 2006, ARA&A, 44, 49

Ricciardelli, E., Trujillo, I., Buitrago, F., & Conselice, C. J. 2010, MNRAS, 406, 230

Richards, G. T., et al. 2006a, ApJS, 166, 470

—. 2006b, AJ, 131, 2766

Risaliti, G., Maiolino, R., & Salvati, M. 1999, ApJ, 522, 157

Robertson, B. E. 2010, ApJ, 713, 1266

Robertson, B. E., Ellis, R. S., Dunlop, J. S., McLure, R. J., & Stark, D. P. 2010, Nature, 468, 49

Sandage, A., Tammann, G. A., & Yahil, A. 1979, ApJ, 232, 352

Schlichting, H. E., & Sari, R. 2007, ApJ, 658, 593

Schmidt, M. 1968, ApJ, 151, 393

Schramm, M., Wisotzki, L., & Jahnke, K. 2008, A&A, 478, 311

Shankar, F., & Mathur, S. 2007, ApJ, 660, 1051

Shields, G. A. 1999, PASP, 111, 661

Shim, H., Chary, R.-R., Dickinson, M., Lin, L., Spinrad, H., Stern, D., & Yan, C.-H. 2011, ArXiv e-prints

Shimasaku, K., Ouchi, M., Furusawa, H., Yoshida, M., Kashikawa, N., & Okamura, S. 2005, PASJ, 57, 447

Shu, F. H. 1982, The physical universe. an introduction to astronomy, ed. Shu, F. H.

Siana, B., et al. 2008, ApJ, 675, 49

Spinrad, H. 2005, Galaxy Formation and Evolution, ed. Spinrad, H.

Springel, V., et al. 2005, Nature, 435, 629

Stanway, E. R., Bremer, M. N., Squitieri, V., Douglas, L. S., & Lehnert, M. D. 2008, MNRAS, 386, 370

Stanway, E. R., Bunker, A. J., & McMahon, R. G. 2003, MNRAS, 342, 439

Stanway, E. R., Bunker, A. J., McMahon, R. G., Ellis, R. S., Treu, T., & McCarthy, P. J. 2004, ApJ, 607, 704

Stanway, E. R., McMahon, R. G., & Bunker, A. J. 2005, MNRAS, 359, 1184

Stanway, E. R., et al. 2007, MNRAS, 376, 727

Stark, D. P., Ellis, R. S., Bunker, A., Bundy, K., Targett, T., Benson, A., & Lacy, M. 2009, ApJ, 697, 1493

Stark, D. P., Ellis, R. S., & Ouchi, M. 2011, ApJ, 728, L2+

Steidel, C. C., Adelberger, K. L., Giavalisco, M., Dickinson, M., & Pettini, M. 1999, ApJ, 519, 1

Stern, D., et al. 2005, ApJ, 631, 163

Stiavelli, M. 2009, From First Light to Reionization: The End of the Dark Ages

Stiavelli, M., Fall, S. M., & Panagia, N. 2004a, ApJ, 600, 508

—. 2004b, ApJ, 610, L1

Stiavelli, M., & Trenti, M. 2010, ApJ, 716, L190

Su, J., et al. 2011, ApJ, 738, 123

Szalay, A. S., Connolly, A. J., & Szokoly, G. P. 1999, AJ, 117, 68

Takeuchi, T. T., Yoshikawa, K., & Ishii, T. T. 2000, ApJS, 129, 1

Taylor, E. N., et al. 2009, ApJS, 183, 295

Tegmark, M., Silk, J., Rees, M. J., Blanchard, A., Abel, T., & Palla, F. 1997, ApJ, 474, 1

Teplitz, H. I., et al. 2011, AJ, 141, 1

Thompson, R. I., et al. 2005, AJ, 130, 1

Tozzi, P., et al. 2006, A&A, 451, 457

Treister, E., Urry, C. M., & Virani, S. 2009, ApJ, 696, 110

Trenti, M., & Stiavelli, M. 2008, ApJ, 676, 767

Trenti, M., Stiavelli, M., Bouwens, R. J., Oesch, P., Shull, J. M., Illingworth, G. D., Bradley, L. D., & Carollo, C. M. 2010, ApJ, 714, L202

Trenti, M., et al. 2011, ApJ, 727, L39+

Vanzella, E., et al. 2006, A&A, 454, 423

—. 2009, ApJ, 695, 1163

—. 2011, ApJ, 730, L35+

Venemans, B. P., McMahon, R. G., Warren, S. J., Gonzalez-Solares, E. A., Hewett, P. C., Mortlock, D. J., Dye, S., & Sharp, R. G. 2007, MNRAS, 376, L76

Verlinde, E. P. 2011, JHEP, 04, 029

Vignali, C., et al. 2009, MNRAS, 395, 2189

Vishniac, E. T. 1983, ApJ, 274, 152

Weinberg, S. 2008, Cosmology, ed. Weinberg, S. (Oxford University Press)

Weinmann, S. M., & Lilly, S. J. 2005, ApJ, 624, 526

White, N. E., Parmar, A., Kunieda, H., Nandra, K., Ohashi, T., & Bookbinder, J. 2010, in American Institute of Physics Conference Series, Vol. 1248, American Institute of Physics Conference Series, ed. A. Comastri, L. Angelini, & M. Cappi, 561–566

Wilkins, S. M., Bunker, A. J., Ellis, R. S., Stark, D., Stanway, E. R., Chiu, K., Lorenzoni, S., & Jarvis, M. J. 2010, MNRAS, 403, 938

Wilkins, S. M., Bunker, A. J., Lorenzoni, S., & Caruana, J. 2011a, MNRAS, 411, 23

Wilkins, S. M., Bunker, A. J., Stanway, E., Lorenzoni, S., & Caruana, J. 2011b, ArXiv e-prints

Willott, C. J., et al. 2007, AJ, 134, 2435

—. 2009, AJ, 137, 3541

—. 2010, AJ, 139, 906

Wirth, G. D. 2004, Nature, 430, 149

Wyithe, J. S. B., & Loeb, A. 2004, Nature, 432, 194

Wyse, R. F. G. 2006, Mem. Soc. Astron. Italiana, 77, 1036

Xue, Y. Q., et al. 2011, ArXiv e-prints

Yan, H., & Windhorst, R. A. 2004, ApJ, 612, L93

Yan, H.-J., Windhorst, R. A., Hathi, N. P., Cohen, S. H., Ryan, R. E., O'Connell, R. W., & McCarthy, P. J. 2010, Research in Astronomy and Astrophysics, 10, 867

Yaqoob, T. 1997, ApJ, 479, 184

Zakamska, N., et al. 2009, in Astronomy, Vol. 2010, astro2010: The Astronomy and Astrophysics Decadal Survey, 69P–+

Zeimann, G. R., White, R. L., Becker, R. H., Hodge, J. A., Stanford, S. A., & Richards, G. T. 2011, ArXiv e-prints

Zheng, W., et al. 2004, ApJS, 155, 73

Vita

Jian has been most familiar with three cities of China: Gaoyou of Jiangsu, a small town where he spent his childhood, Shanghai where he went to Kong Jiang High School & Shanghai Jiao Tong University, and Beijing where he studied theoretical physics at Peking University and decided to pursue higher education abroad.

Jian came to the Henry A. Rowland Department of Physics and Astronomy at the Johns Hopkins University to understand astronomy. During his stay at Baltimore, the best city in the US, Jian also worked for the Space Telescope Science Institute as a research assistant, and for the College of Notre Dame of Maryland as an astronomy instructor.

After graduation, Jian will continue his research, astronomy & medical physics, at Mayo Clinic of Minnesota, working toward a full-time physics faculty in the near future.